UNIVERSITY OF OKLAHOMA

GRADUATE COLLEGE

EFFECT OF WATER ON CATALYTIC REACTIONS OVER BRØNSTED ZEOLITES

A DISSERTATION

SUBMITTED TO THE GRADUATE FACULTY

in partial fulfillment of the requirements for the

Degree of

DOCTOR OF PHILOSOPHY

By

HAN KHIEU CHAU

Norman, Oklahoma

2022

Downloaded from SHAREOK. Persistent Handle URL: https://hdl.handle.net/11244/336612

EFFECT OF WATER ON CATALYTIC REACTIONS

OVER BRØNSTED ZEOLITES

A DISSERTATION APPROVED FOR THE

SCHOOL OF CHEMICAL, BIOLOGICAL AND MATERIALS ENGINEERING

BY THE COMMITTEE CONSISTING OF

Dr. Steven P. Crossley, Chair

Dr. Daniel T. Glatzhofer

Dr. Lance L. Lobban

Dr. Daniel E. Resasco

Dr. Bin Wang

© Copyright by HAN KHIEU CHAU 2022

All Rights Reserved.

The author dedicates this work to his beloved family.

Acknowledgements

I would like to express my sincere thanks and appreciation to the following people for their encouragement and support in completing this dissertation.

First and foremost, I would like to extend my deepest gratitude to my advisor, Dr. Steven Crossley, for his invaluable advice, continuous support, and patience during my PhD study. I am particularly grateful for his flexibility, which has allowed me to work on various exciting research projects. His immense knowledge and strong passion for research have inspired me all the time in my academic work and daily life and helped me to become a better researcher. It has been an honor and a privilege being part of the Crossley Catalysis and Nanomaterials Group.

I am also grateful to Dr. Daniel Resasco for sharing his extensive knowledge and tremendous enthusiasm for heterogeneous catalysis and for teaching me to be a critical thinker, reader, and writer. I would like to thank Dr. Lance Lobban for his encouragement and stimulating discussions in the group meetings. I am thankful to Dr. Bin Wang for his support and fruitful collaboration on DFT theoretical studies. I would like to express gratitude to Dr. Daniel Glatzhofer for being on my committee and providing insightful comments and suggestions on reaction mechanisms. Special thanks to Dr. Phuong Do for being a great collaborator and mentor.

I would like to thank Dr. Nhung Duong, Dr. Zheng Zhao, and Dr. Lawrence Barrett for helping me start in the lab at the beginning of my graduate years. I also had the great pleasure of working with many current and past members of OU Catalysis Group. I am very grateful to my friends and colleagues at OU: anh Ngoc, chi Huyen, anh Tuong, anh Tuan, chi Tram, anh Tien, chi Nhung, anh Quoc, anh Duong, chi Vi, anh Vinh, anh Thang, chi Linh, chi Oanh, Thanh, Vy, Thao, Phat, Quy, chi Vinh, Brandon, Gabriela, Daniela, Nilson, Gengnan, Malli, Feifei, Ximo, Tong, Reda, Alejandra, Ana, Elton, Ismaeel, Caleb, Donnie, Ethan, Yu, Nut, Nabihan, Erich, Luis,

Thomas. It is their kind support in the research and outside of work that has made my study and life at OU a wonderful time.

My appreciation also goes to Terri, Donna, Ginger, Rett, Nicole, and Madena for their support with paperwork, purchasing chemicals and equipment, and making my research proceed smoothly.

Many thanks should also go to Anton and Andrew for helping with fixing reactors and instrument troubleshooting.

I would like to acknowledge the funding sources for my work and the University of Oklahoma for the opportunity to study and perform this research.

Finally, words cannot express my gratitude to my family and friends for their unwavering support, sacrifices, and understanding. I am extremely grateful to my wife, Tien, and our little baby, Gift (Quan), for their unconditional love and pure joy. This endeavor would not have been possible without you.

Table of Contents

Acknowledgements iv

List of Tables xi

List of Figures xii

Abstract xx

Chapter 1: Introduction 1

Chapter 2: Acylation of m-cresol with acetic acid supported by in-situ ester formation on H-ZSM-5 zeolites 4

- Abstract 4
- Introduction 5
- Experimental 8
  - Catalyst preparation 8
  - Catalyst characterization 9
  - Catalytic testing 10
- Results and discussion 12
  - Reaction order and activation energy measurements 12
  - Kinetically relevant intermediate ester formed inside H-ZSM-5 zeolite pores 18
  - Catalyst deactivation 24
- Conclusions 26
- Acknowledgements 27

Chapter 3: Effect of water and acid site proximity on cumene dealkylation over H-ZSM-5 zeolites 28

- Abstract 28
- Introduction 29

Experimental 32
Catalyst preparation 32
Catalyst characterization 33
Catalytic testing 33
Results and discussion 35
Cumene dealkylation over H-ZSM-5 zeolites in the absence of water 35
Kinetic effect of co-feeding water in cumene dealkylation 42
Kinetic role of paired Brønsted acid sites and water 44
Catalyst deactivation in cumene dealkylation: effect of extra-framework aluminum species, reaction temperature, and the presence of water 52
Conclusion 57
Acknowledgement 58
Chapter 4: The role of water on zeolite-catalyzed transformation of polar polymers 59
Abstract 59
Introduction 60
Results 61
Effect of polar aprotic solvent and co-feeding water on dehydration of model compound .. 61
DFT analysis in the effect of GVL and co-fed water on the dehydration of DMTHF 77
Effect of water on dehydration of real EVOH polymer 83
Conclusion 85
Methods 85
Reagents 85
Catalyst preparation 86

Characterization 87
Catalytic testing 87
DFT calculations 89
Acknowledgements 90
Chapter 5: Concluding remarks 91
Chapter 6: Future works 93
References 95
Appendix A1: Supporting information for Chapter 2 108
S1. Catalyst characterization 108
S2. Diffusion test by titration method 109
S3. Derivation of initial rates of the acylation of m-cresol with acetic acid over MFI-140 zeolite 111
S3.1. Acylium ion formation from m-Tolyl acetate is the rate-limiting step. C-C coupling step follows Eley-Rideal reaction model. 112
S3.2. C-C coupling is the rate-limiting step. C-C coupling step follows Eley-Rideal reaction model. 113
References 114
Appendix A2: Acylation of m-cresol with acetic acid: effect of zeolite framework and water . 115
1. Materials and methods 115
2. Effect of zeolite frameworks 115
3. Effect of water 116
Appendix A3: Supporting information for Chapter 3 119
S1. Derivation of cumene dealkylation rate by transition state theory 119

S2. Catalyst deactivation during cumene dealkylation 120
References 121
Appendix A4: Supporting information for Chapter 4 122
S1. Statistical Thermodynamics Calculation 122
References 124
Appendix A5: Dehydration of 2,4-pentanediol and ethylene-vinyl alcohol co-polymer (EVOH) over sulfonic acid-functionalized silica catalyst 125
1. Materials and methods 125
2. Thermal Gravimetric Analysis (TGA) results 127
3. Vapor phase dehydration of 2,4-pentanediol 128
4. Liquid phase dehydration of EVOH in DMSO 129
References 132
Appendix A6: Effect of water solvent on hydrogenation of a phenolic compound over supported metal catalysts in aqueous phase 133
1. Materials and methods 133
2. Effect of water solvent on the hydrogenation of o-cresol 134
Acknowledgements 139
References 139

List of Tables

Table 1. Brønsted acid site densities of zeolites used in acylation reactions 13

Table 2. Brønsted acid site densities of H-ZSM-5 zeolites used in cumene dealkylation 35

Table 3. Initial turnover frequency (1/s) and rate enhancement percentage of cumene dealkylation over different zeolites in the absence and presence water at 300°C 44

Table 4. Apparent activation energy, apparent activation enthalpy, and apparent activation entropy of cumene dealkylation on different zeolites with and without water co-feeding 46

Table 5. Brønsted acid site densities of zeolites used in dehydration reactions 65

Table 6. Adsorption energetics of species on the Brønsted acid sites 78

Table 7. BET surface area of zeolite catalysts 108

Table 8. Coke content on the spent MFI-140 catalysts after 130 minutes reaction time on stream with varying $P_{acetic\ acid}$ and keeping $P_{m\text{-}cresol}$ at 0.3 kPa, $T_{reaction}$ = 250°C 109

Table 9. Fractions of bonds associated with hydrogen atoms in EVOH 131

Table 10. BET surface areas and pore volumes of catalyst supports 135

List of Figures

Fig. 1. Yield of m-Tolyl acetate formation in molar percentage using 50 mg MFI-40 (■), 25 mg MFI-40 (●), 25 mg MFI-140 (▲) at 250°C, $P_{acetic\ acid}$ = 1.4 kPa, $P_{m\text{-}cresol}$ = 0.3 kPa 13

Fig. 2. Initial turnover frequency of 2-hydroxyl-4-methylacetophenone formation over different H-ZSM-5 zeolites at 250°C, $P_{acetic\ acid}$ = 1.4 kPa, $P_{m\text{-}cresol}$ = 0.3 kPa..... 14

Fig. 3. Varying the partial pressure of acetic acid in acylation reaction with m-cresol over MFI-140 at 250°C, $P_{acetic\ acid}$ = 0.3 – 4.1 kPa, $P_{m\text{-}cresol}$ = 0.3 kPa. Rates of 2-hydroxyl-4-methylacetophenone formation are extrapolated to 0 min TOS. 16

Fig. 4. Varying the partial pressure of m-cresol over MFI-140 at 250°C, $P_{acetic\ acid}$ = 1.4 kPa, $P_{m\text{-}cresol}$ = 0.3 – 0.9 kPa. Rates of 2-hydroxyl-4-methylacetophenone formation are extrapolated to 0 min TOS. 17

Fig. 5. The true activation energy of 2-hydroxyl-4-methylacetophenone formation on MFI-140 over temperature range of 200-250°C, $P_{acetic\ acid}$ = 1.4 kPa, $P_{m\text{-}cresol}$ = 0.3 kPa. Rates of 2-hydroxyl-4-methylacetophenone formation are extrapolated to 0 min TOS. 18

Fig. 6. The rate of 2-hydroxyl-4-methylacetophenone formation in reactions of m-cresol with acetic acid (■), m-tolyl acetate + water (▲), m-tolyl acetate (●) over MFI-140 at 250°C, $P_{m\text{-}cresol}$ = 0.3 kPa, $P_{acylating\ agent}$ = 1.4 kPa, P_{water} = 0.9 kPa. The dashed lines are a guide to the eye. 20

Fig. 7. The rate of 2-hydroxyl-4-methylacetophenone formation in reactions of m-cresol with acetic acid (■), m-tolyl acetate (●) over BEA-133 at 250°C, $P_{m\text{-}cresol}$ = 0.3 kPa, $P_{acylating\ agent}$ = 1.4 kPa, P_{water} = 0.9 kPa. The dashed lines are a guide to the eye. 22

Fig. 8. Turnover frequency of 2-hydroxyl-4-methylacetophenone formation over MFI-140 as a function of cumulative catalyst turnover number at 250°C, $P_{m\text{-}cresol}$ = 0.3 kPa, $P_{acetic\ acid}$ = 1.4 kPa (●), $P_{acetic\ acid}$ = 2.8 kPa (■), $P_{acetic\ acid}$ = 4.1 kPa (▲). The dash lines are a guide to the eye. 25

Fig. 9. FT-IR spectra of MFI-11.5 and AHFS-MFI-11.5 measured at 300°C. Absorbance intensity of catalyst samples were normalized based on the peak of Brønsted acid site (Si-O(H)-Al) and Brønsted acid site density obtained from IPA-TPRx..... 36

Fig. 10. Rate of cumene dealkylation over different zeolites at reaction temperature of 300°C as a function of time on stream (TOS), P_{cumene} = 0.5 kPa..... 37

Fig. 11. Correlation of Brønsted acid site density with the amount of aluminum in pairs in different H-ZSM-5 zeolites. Fraction of aluminum in pairs was obtained from literature [91]..... 38

Fig. 12. Cumene dealkylation rate as a function of fraction of aluminum in pairs in H-ZSM-5 zeolites at 300°C, P_{cumene} = 0.5 kPa. The dash line is a guide to the eye. 39

Fig. 13. Linear regression fitting of cumene dealkylation rate versus function of fraction of aluminum in pairs in H-ZSM-5 zeolites (Si/Al ≥ 15) at 300°C, P_{cumene} = 0.5 kPa. 40

Fig. 14. Cumene dealkylation turnover frequency on paired sites as a function of fraction of aluminum in pairs in H-ZSM-5 zeolites at 300°C, P_{cumene} = 0.5 kPa. The dash line represents a linear regression fitting of data points 41

Fig. 15. Cumene dealkylation with intermittent water co-feeding over MFI-11.5, AHFS-MFI-11.5, MFI-40, and MFI-140 at T = 300°C, P_{cumene} = 0.5 kPa, P_{water} = 0 – 3.5 kPa..... 43

Fig. 16. Cumene dealkylation with intermittent water co-feeding over MFI-140 at T = 350°C, P_{cumene} = 0.5 kPa, P_{water} = 0 – 3.5 kPa 43

Fig. 17. Reaction order of cumene dealkylation over different zeolites in the absence of water (P_{water} = 0 kPa) and presence of water (P_{water} = 3.5 kPa) at 300°C 45

Fig. 18. Arrhenius plots for cumene dealkylation over different zeolites with and without water co-feeding, P_{cumene} = 0.5 kPa, P_{water} = 0 – 3.5 kPa 45

Fig. 19. Initial turnover frequency of cumene dealkylation with varying partial pressure of water co-feeding over H-ZSM-5 zeolites at reaction temperature of 300°C, P_{cumene} = 0.5 kPa. Dashed lines are to guide the eye..... 50

Fig. 20. a) Conversion of cumene before and after pulsing water over 5 mg MFI-11.5 (T = 300°C); **b)** Compare conversion of cumene dealkylation (T = 300°C, P_{cumene} = 1.17 kPa) and n-hexane cracking (T = 480°C, $P_{n\text{-}hexane}$ = 4.5 kPa) [82] before and after pulsing water 51

Fig. 21. Product selectivity of cumene dealkylation over different zeolites with and without water co-feeding at 300°C, TOS = 30 min, P_{cumene} = 0.5 kPa, P_{water} = 0 – 3.5 kPa 53

Fig. 22. Deactivation plots of different zeolites in cumene dealkylation at reaction temperature of 300°C, P_{cumene} = 0.5 kPa 53

Fig. 23. Effect of water co-feeding on deactivation of AHFS-MFI-11.5 at reaction temperature of 300°C, P_{cumene} = 0.5 kPa, P_{water} = 0 kPa (□); P_{cumene} = 0.5 kPa, P_{water} = 3.5 kPa (■)..... 55

Fig. 24. Effect of reaction temperature on deactivation of H-ZSM-5 (Si/Al = 40) in the absence and presence of water, P_{cumene} = 0.5 kPa, P_{water} = 0 – 3.5 kPa 55

Fig. 25. Effect of reaction temperature on deactivation of AHFS-MFI-11.5 in the absence and presence of water, P_{cumene} = 0.5 kPa, P_{water} = 0 – 3.5 kPa 55

Fig. 26. Effect of reaction temperature on deactivation of MFI-11.5 in the absence and presence of water, P_{cumene} = 0.5 kPa, P_{water} = 0 – 3.5 kPa 56

Fig. 27. Dehydration of 2,5-hexanediol model compound. **a,** Schematic reaction pathway of 2,5-hexanediol dehydration over Brønsted zeolites. **b,** Product yields of 2,5-hexanediol dehydration over MFI-140 with varying reaction space time. Reaction conditions: T = 250°C, $P_{2,5\text{-}hexanediol}$ = 0.09 kPa, P_{GVL} = 0.6 kPa. **c,** Initial turnover frequency of hexadienes formation in 2,5-hexanediol

dehydration over different H-ZSM-5 zeolites in the absence and presence of water. Reaction conditions: T = 250°C, $P_{2,5\text{-hexanediol}}$ = 0.09 kPa, P_{GVL} = 0.6 kPa, P_{water} = 0 kPa or 3.5 kPa..... 63

Fig. 28. Product yields of 2,5-hexanediol dehydration over MFI-140 during reaction time on stream. Reaction conditions: T = 250°C, $P_{2,5\text{-hexanediol}}$ = 0.09 kPa, P_{GVL} = 0.6 kPa..... 64

Fig. 29. Turnover frequency of hexadienes formation over different MFI zeolites. Reaction conditions: T = 250°C, $P_{2,5\text{-hexanediol}}$ = 0.09 kPa, P_{GVL} = 0.6 kPa 65

Fig. 30. Initial turnover frequency of hexadienes formation over BEA-133 zeolite in the absence and presence of water. T = 250°C, $P_{hexanediol}$ = 0.09 kPa, P_{GVL} = 0.6 kPa, P_{water} = 0 kPa (■), P_{water} = 3.5 kPa (■) 66

Fig. 31. Hexadienes formation rate per gram catalyst over different MFI zeolites in the absence and presence of water. T = 250°C, $P_{hexanediol}$ = 0.09 kPa, P_{GVL} = 0.6 kPa, P_{water} = 0 kPa or 3.5 kPa 67

Fig. 32. Catalyst characterization. **a,** Brønsted acid site density of different zeolites measured by temperature program reaction of isopropyl amine. **b,** Mass loss of MFI-140 sample after being exposed to water (P_{water} = 3.5 kPa, T = 250°C, 1 hour) from thermogravimetric analysis (TGA)68

Fig. 33. Turnover frequency of hexadienes formation over. **a,** MFI-140 and **b,** MFI-40. Reaction conditions: T = 250°C, $P_{hexanediol}$ = 0.09 kPa, P_{GVL} = 0.6 kPa, P_{water} = 0 kPa (●), P_{water} = 3.5 kPa (●), P_{water} = 7.0 kPa (▲) 69

Fig. 34. Yield of pentenoic acids formation from GVL over MFI-140 during 2,5-hexanediol dehydration in the presence of GVL. Reaction conditions: T = 250°C, $P_{hexanediol}$ = 0.09 kPa, P_{GVL} = 0.6 kPa, P_{water} = 0 kPa (●), P_{water} = 3.5 kPa (●) 70

Fig. 35. Turnover frequency of hexadienes formation over MFI-140. **a,** in two separated experiments. **b,** in one experiment with intermittent co-feeding. Reaction conditions: T = 250°C,

P_{DMTHF} = 0.08 kPa; $P_{4\text{-pentenoic acid}}$ = 0 kPa, P_{water} = 0 kPa (●); $P_{4\text{-pentenoic acid}}$ = 0.16 kPa, P_{water} = 0 kPa (●); $P_{4\text{-pentenoic acid}}$ = 0.16 kPa, P_{water} = 3.5 kPa (●)..... 70

Fig. 36. Dehydration of intermediate ether 2,5-dimethyltetrahydrofuran. **a,** Turnover frequency of hexadienes formation over MFI-140 in the absence and presence of water. Reaction conditions: T = 250°C, P_{DMTHF} = 0.08 kPa; P_{GVL} = 0 kPa, P_{water} = 0 kPa (●); P_{GVL} = 0 kPa, P_{water} = 3.5 kPa (♦); P_{GVL} = 0.6 kPa, P_{water} = 3.5 kPa (▲); P_{GVL} = 0.6 kPa, P_{water} = 0 kPa (■). **b,** Turnover frequency of hexadienes formation over MFI-140 with intermittent co-feeding of water. T = 250°C, PDMTHF = 0.08 kPa, P_{water} = 0 kPa (●) or 3.5 kPa (●). **c,** Correlation between reaction rate and reaction order with respect to 2,5-dimethyltetrahydrofuran in different co-feeding experiments over MFI-140. Reaction conditions: T = 250°C, P_{DMTHF} = 0.08 kPa; P_{GVL} = 0 kPa, P_{water} = 0 kPa (■); P_{GVL} = 0 kPa, P_{water} = 3.5 kPa (■); P_{GVL} = 0.6 kPa, P_{water} = 0 kPa (■); P_{GVL} = 0.6 kPa, P_{water} = 3.5 kPa (■). **d,** Inhibition effect of GVL on dehydration of 2,5-dimethyltetrahydrofuran over MFI-140. Reaction conditions: T = 250°C, P_{DMTHF} = 0.08 kPa; P_{GVL} = 0.30 – 1.16 kPa..... 72

Fig. 37. Reaction order of 2,5-dimethyltetrahydrofuran dehydration with respect to 2,5-dimethyltetrahydrofuran over MFI-140. T = 250°C, P_{DMTHF} = 0.08 – 0.4 kPa 74

Fig. 38. Reaction order of 2,5-dimethyltetrahydrofuran dehydration with respect to 2,5-dimethyltetrahydrofuran over MFI-140. T = 250°C, P_{DMTHF} = 0.08 – 0.4 kPa, P_{water} = 3.5 kPa.. 74

Fig. 39. Reaction order of 2,5-dimethyltetrahydrofuran dehydration with respect to 2,5-dimethyltetrahydrofuran over MFI-140. T = 250°C, P_{DMTHF} = 0.08 – 0.4 kPa, P_{GVL} = 0.6 kPa .. 75

Fig. 40. Reaction order of 2,5-dimethyltetrahydrofuran dehydration with respect to 2,5-dimethyltetrahydrofuran over MFI-140. T = 250°C, P_{DMTHF} = 0.08 – 0.4 kPa, P_{water} = 3.5 kPa, P_{GVL} = 0.6 kPa 75

Fig. 41. Apparent activation energy of hexadienes formation in 2,5-hexanediol dehydration over MFI-140. Reaction conditions: $P_{2,5\text{-hexanediol}}$ = 0.09 kPa, P_{GVL} = 0.6 kPa, P_{water} = 0 kPa (without water) or 3.5 kPa (with water) 76

Fig. 42. Gibbs free energy of adsorption of GVL, DMTHF, and pentenoic acid. Z: zeolite framework; H: the proton; ZH: the framework Brønsted acid site ("conventional" BAS); GVL: γ-valerolactone; DMTHF: 2,5-dimethyl tetrahydrofuran; PA: pentenoic acid isomers; W: water; W4: cluster of four water molecules; W4H: the hydronium cluster ("mobile" BAS)..... 77

Fig. 43. The DFT optimized structures over the framework Brønsted acid site. The aluminum, silicone, oxygen, carbon, and hydrogen atoms are, respectively, colored by pink, yellow, red, yellow, and white. **a,** γ-valerolactone (GVL). **b,** 2,5-dimethyl tetrahydrofuran (DMTHF). **c,** pentenoic acid isomers (PA). **d,** hydronium cluster..... 80

Fig. 44. The DFT optimized structures on the hydronium cluster. The aluminum, silicone, oxygen, carbon, and hydrogen atoms are, respectively, colored by pink, yellow, red, yellow, and white. **a,** γ-valerolactone (GVL). **b,** 2,5-dimethyl tetrahydrofuran (DMTHF). **c,** pentenoic acid isomers (PA)..... 82

Fig. 45. Dehydration of EVOH polymer. **a,** FT-IR spectra of original EVOH powder and dried solid products after reactions in liquid phase. Reaction conditions: 300 mg EVOH powder, 20 ml solvent, 100 mg MFI-140, T = 120°C, reaction time = 2 h, stirring = 600 rpm. **b,** FT-IR peak intensity ratios of C=O stretching to O-H bending or O-H stretching of original EVOH powder and dried solid products after reactions in liquid phase. **c,** Illustrated scheme for the formation of C=O double bonds in EVOH dehydration over solid acid catalyst in GVL solvent. 84

Fig. 46. Rate of 2-hydroxyl-4-methylacetophenone formation over different zeolites at 250°C, $P_{m\text{-cresol}}$ = 0.3 kPa, $P_{acetic\ acid}$ = 1.4 kPa 116

Fig. 47. Rate of 2-hydroxyl-4-methylacetophenone formation in reactions of m-cresol with acetic acid (■), m-tolyl acetate (▲), m-tolyl acetate + water (●) over BEA-133 at 250°C, $P_{m\text{-}cresol}$ = 0.3 kPa, $P_{acylating\ agent}$ = 1.4 kPa, P_{water} = 0 – 0.9 kPa 117

Fig. 48. Effect of water co-feeding on m-cresol acylation with acetic acid over BEA-133 at 250°C, $P_{m\text{-}cresol}$ = 0.3 kPa, $P_{acetic\ acid}$ = 1.4 kPa, P_{water} = 0 – 0.9 kPa 117

Fig. 49. TGA-TPO plot of SiO_2-SO_3H catalyst 127

Fig. 50. Initial conversion, product yields, and product selectivity of 2,4-pentanediol dehydration over SiO_2-SO_3H at 0-min TOS. Reaction conditions: T = 200°C, $P_{2,4\text{-}pentanediol}$ = 0.3 kPa 129

Fig. 51. a) FT-IR spectra of fresh EVOH powder and dried solid products after reactions in liquid phase. **b)** FT-IR peak intensity ratios of different bonds of fresh EVOH powder and dried solid products after reactions in liquid phase. Reaction conditions: Nitrogen atmosphere, 1 g EVOH, 10 ml DMSO, T = 120°C, 100 mg catalyst, reaction time = 2 h, stirring = 600 rpm 130

Fig. 52. ^{1}H NMR spectrum of fresh EVOH polymer in DMSO-d6 131

Fig. 53. ^{13}C NMR spectrum of fresh EVOH polymer in DMSO-d6 132

Fig. 54. The change of in-situ ATR-IR signal versus reaction time on stream 135

Fig. 55. Concentration vs. time profiles from in-situ IR spectra during the hydrogenation of o-cresol in n-dodecane at 150°C on Pd/SiO_2. Reaction conditions: 120 ml n-dodecane, 60 mg Pd/SiO_2. Concentration values are calibrated by the in-situ ATR-IR peak heights..... 136

Fig. 56. TEM image of palladium particles on carbon nanotubes 137

Fig. 57. Concentration vs. time profiles from in-situ IR spectra during the hydrogenation of o-cresol in water at 150°C on Pd/CNT. Reaction conditions: 120 ml water, 63 mg Pd/CNT. 137

Fig. 58. Concentration vs. time profiles from in-situ IR spectra during the hydrogenation of o-cresol in water at 150°C on Pd/CNT. Reaction conditions: 120 ml n-dodecane, 61 mg Pd/CNT. 138

Abstract

Water is present in both conventional chemical transformations and conversion of renewable emerging feedstocks such as biomass and plastic waste. Solid acids and zeolites, in particular, have been one of the most common industrial heterogeneous catalysts for decades. Interestingly, the interactions of water with reaction intermediates and framework protons in Brønsted zeolites give rise to various catalytic effects. In the first part, the role of water in the acylation of a phenolic compound with a carboxylic acid representing the upgrading reaction of lignocellulosic biomass has been revealed. The bulky intermediate ester is an active acylating agent but diffuses slowly in MFI pores, which can be manipulated by co-feeding water. In the second part, the effect of water on the conversion of a non-polar hydrocarbon was studied. The presence of a sufficient concentration of water inside the zeolite pores enables the formation of hydrated hydronium ions, which enhances the cumene dealkylation due to entropic gain of the reaction transition state. Finally, the influence of water on the dehydration of a diol representing polar polymers in multilayer polymer films in the presence of a competitive polar aprotic solvent was investigated. The change in the adsorption states of the reaction intermediate and solvent molecules on framework Brønsted acid sites versus hydrated hydronium ions alleviates the inhibition effect of solvent and improves the dehydration of polyols.

Keywords: zeolites, Brønsted acid sites, water, hydronium ions, diffusion, adsorption state, transition state, acylation, dealkylation, dehydration.

Chapter 1: Introduction

Zeolites are crystalline microporous aluminosilicates, which consist of corner-sharing TO_4 tetrahedra (T site can be Si or Al). In terms of catalysis, zeolites are one of the most important solid acid catalysts in chemicals and transportation fuels production industry for many decades [1]. As of today, over 200 zeolite structures have been defined, among which are commercially important catalysts such as H-ZSM-22, H-ZSM-5, H-Beta, and HY with pore sizes ranging approximately from 0.45 to 0.74 nm [1]. The important properties of zeolite materials include, but not limited to, high surface area, high shape selectivity for reactants and products due to well-defined pore dimensions, and confinement effect [2]. As the framework Si^{4+} atoms are replaced by Al^{3+} atoms, it creates a negative charge which can be neutralized by extra-cations such as proton or metals [3]. In case the counterbalanced cations are protons, they become strong Brønsted acid sites which play important roles on many acid-catalyzed reactions.

Water is ubiquitous in both conventional hydrocarbon transformation in crude oil refinery and conversion of emerging feedstocks such as biomass and plastic waste. Therefore, it is of critical importance to understand the divergent roles of water in catalytic reactions on a molecular level. In fact, the effects of water on zeolites structure, catalytic activity, and catalyst stability against coking have been widely investigated in both liquid and vapor phase reactions [4-13]. In terms of zeolite structure stability, the hydrolysis of Si-O-Si bridges or amorphization at silanol defects in aqueous phase can happen at the temperature range of 373-573 K and the hydrolysis of Si-O(H)-Al can occur at temperature above 723 K in steaming conditions, leading to loss of crystallinity and changes in catalyst performance [5, 6, 8]. In terms of catalytic activity, the presence of water molecules inside zeolite pores can influence mass transfer of reactants and products, solvation or enthalpic stabilization of reactants or transition states, and facilitating proton

transfer and remote bond polarization [4]. On the other hand, it has been reported that the presence of water molecules inside zeolite pores around Brønsted acid sites could facilitate the proton delocalization and form hydronium ion clusters [14-16]. These hydronium ion clusters can act as mobile acid sites and show distinctively intriguing catalytic properties compared to the conventional framework Brønsted acid sites, such as extending the Brønsted acid site proximity via water-bridge networks in high Brønsted acid site density catalysts or generating highly ionic environment inside zeolite pores [17, 18].

There are many critical features that influence the catalytic performance of zeolite catalysts, including framework type, pore size and structure, and intrinsic properties of acid sites in zeolites. Within the same zeolite framework such as ZSM-5, the location and distribution acid sites vary with changing Si/Al ratio, which show a diverse stabilization of reactive intermediates and reaction transition states by van der Waals force, leading to distinct catalytic reactivity of these acid sites [3, 19, 20]. Based on zero-order and first-order rate constants of methanol dehydration, Iglesia and co-workers found that Brønsted acid sites are favorably located at channel intersections in high-silica ZSM-5 (Si/Al > 23) and more Brønsted acid sites would occupy more confined pore channels with lowering Si/Al ratio [21]. Haag and co-workers proposed that the relative pore sizes and shape selectivity of medium-pore zeolites such as H-ZSM-5 could be probed by the constraint index (CI), which is defined as the ratio of cracking rate of n-hexane to 3-methylpentane [22]. As a result, this method could give us some insights about the location of acid sites in zeolites [23]. The higher the CI, the more acid sites located in the more confined pore channels.

The distribution of aluminum in terms of crystallographic unique T-site sitting and how proximity of these aluminum species has attracted much attention from several research groups. Wichterlová and co-workers carried out UV-Vis analysis of dehydrated Co-zeolites exchanged to

the maximum degree and reported that the distribution of aluminum atoms in ZSM-5 zeolites is influenced by Si/Al ratio and not random [24, 25]. In fact, the proximity of Brønsted acid sites influences many reactions such alkane cracking, olefin oligomerization, and alcohol dehydration [26-30].

In this work, the divergent effects of water on diffusion of reactive intermediate, transition state, and adsorbed reactant in different reactions such as Friedel-Crafts acylation of lignin-derived compounds, dealkylation of hydrocarbon, and dehydration of polyalcohols over various Brønsted zeolites was investigated by reaction kinetics under the conditions where zeolite framework hydrolysis or dealumination in the presence of water is minimized. While water is abundantly present as by-product of lignocellulosic biomass upgrading processes, many hydrocarbon conversion units in crude oil refinery such as catalytic reforming and fluid catalytic cracking are exposed to moisture or steam. In addition, the conversion of plastic waste streams can also encounter the presence of water. Fundamental understanding of interaction of water molecules with zeolite catalysts in these transformations would help elucidate the important factors which manipulate the effect of water such as polarity of reactants, aluminum location and distribution in zeolite catalysts, partial pressure of water, and reaction temperature. As a result, it will enable us to control and tune the selectivity of complex reaction systems by developing robust catalytic systems with co-feeding optimal amount of moisture.

Chapter 2: Acylation of m-cresol with acetic acid supported by in-situ ester formation on H-ZSM-5 zeolites

This chapter is based on a publication in Journal of Catalysis. Complete article and supplementary material can be found using the citation: Han K. Chau, Daniel E. Resasco, Phuong Do, Steven P. Crossley, "Acylation of m-cresol with acetic acid supported by in-situ ester formation on H-ZSM-5 zeolites", Journal of Catalysis 406 (2022) 48–55.

Abstract

Friedel-Crafts acylation of phenolic compounds with carboxylic acids catalyzed by Brønsted-acid zeolites is an interesting reaction that could find application in the production of fuels and chemicals from renewable feedstocks. The mechanism of direct acylation of m-cresol with acetic acid over protonic zeolites and the role that the confining environment may have on reaction rate and product selectivity are topics of current interest. Here, we evaluate this reaction at varying conditions over H-ZSM-5 catalysts with different acid site densities. By decoupling the effect of parasitic phenomena – diffusion and catalyst deactivation – we have been able to evaluate the true kinetics of this reaction. We have found that, in the absence of a solvent, the reaction over H-ZSM-5 zeolites under commonly studied conditions (Si/Al = 40) at 250°C is often influenced by the diffusion of reactants to active sites. By further decreasing active site density and operating under diffusion-free conditions, the true activation barrier for acetophenone (2-hydroxyl-4-methylacetophenone) formation obtained on H-ZSM-5 under surface-saturation conditions is relatively low (41 kJ/mol). This value is significantly lower than the barrier associated with the dehydration of the carboxylic acid to form surface acyl species when not assisted by the formation of intermediate ester species. Based on reaction kinetic analysis, it is proposed that the formation of acylium ion from adsorbed m-tolyl acetate is the rate-limiting step. However, feeding the

intermediate ester – i.e., m-tolyl acetate – to act as acylating agent, results in reduced rates compared to those in which the acylating agent is acetic acid. This result reveals that the diffusion of m-tolyl acetate is slow and the kinetically relevant ester is formed within the confines of the zeolite pores. By co-feeding water with m-tolyl acetate, we reveal that the bulky ester is hydrolyzed to form smaller molecules that diffuse faster inside zeolite pores and subsequently enhance the reaction rate. Vapor phase acylation of m-cresol with acetic acid over low acid site density H-Beta zeolite confirms the role of the active intermediate ester in accelerating the rate of acylated product formation. Catalyst deactivation during reaction increases with the partial pressure of acetic acid, even under the zero-order kinetic regime, during which the partial pressure of produced gaseous ketene remains constant. This result would indicate that this usual coke precursor is not the main cause of deactivation, but rather bulkier compounds formed by subsequent esterification of acetic acid with the acylated product (e.g., 2-hydroxyl-4-methylacetophenone).

Introduction

The conversion of lignocellulosic biomass into transportation fuels and chemicals has attracted great attention in recent years [31, 32]. The most prevalent compounds derived from these renewable sources include phenolic species and carboxylic acids. Direct Friedel-Crafts acylation in which the carboxylic acid is the acylating agent is an attractive approach for functionalization due to its high potential selectivity and carbon efficiency [32], with benefits in overall life-cycle CO_2 emissions compared with other transportation fuel production pathways originating from biomass pyrolysis [33-35]. The acylation of aromatic compounds in the presence of acid catalysts is generally accepted to proceed through the coupling of acylium cations interacting with the nucleophilic aromatic rings [36]. The original Friedel-Crafts acylation (also known as acetylation) used homogeneous strong Lewis acid catalysts such as $AlCl_3$ [37], which generate large amounts

of waste. Recently, heterogeneous solid acid catalysts such as zeolites (ZSM-5, Beta, USY, La-Y, Mordenite) and mesoporous materials such as MCM-41 and SBA-15 have gained much attention due to their ease of separation from the reaction mixture, a more facile catalyst recovery, and less undesired side products [38, 39]. Acylium ions can be generated from strong acylating agents such as acyl chloride, acetic anhydride or mild acylating agents such as carboxylic acids and esters [36, 40, 41]. In particular, acetic acid is present in high concentrations in pyrolysis products of lignocellulosic biomass and acetic anhydride can be produced by dehydration of acetic acid at high temperature [35]. Oxygenated aromatic compounds such as anisole and cresol, furanic compounds, or even less reactive aromatics such as toluene are effective acyl acceptors that couple with acyl groups [36, 42-45]. Replacing anhydrides or acyl halides has the obvious potential to minimize steps and energy input, but it also requires more severe operating conditions to generate the active surface acyl species. However, at high temperatures, acid sites may also catalyze self-coupling reactions to form ketones, which generate carbon dioxide and water as byproducts [46, 47]. Advancing the understanding of direct acylation with carboxylic acids without the use of intermediate anhydrides or acyl halides could significantly improve the energy requirements for forming fuels and chemicals from renewable sources, but the more severe conditions required for acylium ion formation directly from acids requires care to minimize undesirable side reactions.

Acylation reactions have been primarily studied in the condensed phase with liquid solvents, commonly over Brønsted acid zeolites such as HY, H-ZSM-5, and H-Beta [32, 44, 48]. Since in these studies different solvents have been employed and often the roles of diffusion and deactivation on observed reaction rates have not been properly accounted for, conflicting conclusions have been drawn regarding the most effective catalyst needed to carry out this reaction. This uncertainty also complicates our ability to determine the actual reaction mechanism

since various intermediates, such as esters, may be formed and they may influence the overall acylation rate. Similarly, different intermediates and/or side products may influence catalyst deactivation, which further complicates the analysis. Acylation chemistry has been evaluated in the vapor phase as well, where continuous flow reactors are employed providing easier decoupling of diffusion vs. reaction and separating catalyst activity vs. deactivation rates. In these instances, it has been revealed that not only is deactivation important when assessing reaction rates [43], but rates of deactivation can be highly dependent on the acid coverage on the catalyst surface. Flow studies have revealed, for example, that high coverages of carboxylic acids on the surface of the catalyst can limit direct adsorption of reactive acyl acceptors and products, which limit subsequent coke forming reactions [43, 45, 49].

In this study, the acylation of m-cresol with acetic acid, two common molecules derived from biomass, has been studied in a vapor phase flow reactor over high Si/Al ratio H-ZSM-5 and H-Beta zeolites. The roles of diffusion of m-cresol, acetic acid, as well as the active intermediate have been considered. This is an important aspect that may affect the analysis but has not been fully contemplated in previous literature. Unlike other acyl acceptors such as anisole or toluene, m-cresol reacts rapidly with acetic acid in the presence of zeolite catalysts to form m-tolyl acetate [50, 51]. The acetate has been shown in larger pored zeolites in liquid phase studies to facilitate decomposition to form surface acyl species which accelerates subsequent C-C coupling rates with acyl acceptors [51]. The role of an intermediate formed during reaction and how it enhances the rate of acylation while properly accounting for its diffusion within zeolite micropores is discussed in detail.

In addition to the net reaction rate, catalyst stability under acylation reaction conditions is an important aspect that must be considered. Without properly decoupling deactivation from the

intrinsic reaction rates, erroneous conclusions regarding reaction rates and mechanism may be drawn. The deactivation mechanism of zeolites during acylation reactions is usually ascribed to either gaseous ketene species from acylium ion desorption, the acylated products, or subsequent reactions of the acylated products [52-54]. Here, we investigate these potential causes as well as the role of gas-phase acetic acid on catalyst deactivation.

Experimental

Catalyst preparation

ZSM-5 zeolites with two different Si/Al ratios were purchased in the ammonium form NH_4-ZSM-5 from Zeolyst International (CBV-8014 with Si/Al = 40, CBV-28014 with Si/Al = 140). Beta zeolite (Si/Al = 133) was obtained in proton-form H-Beta from Alfa Aesar. Sodium exchange of NH_4-ZSM-5 (CBV-28014) was carried out to titrate a fraction of the Brønsted acid site for diffusion test. NH_4-ZSM-5 (CBV-28014) and NH_4-ZSM-5 (CBV-8014) samples were mixed with 10 mM $NaNO_3$ solution and 0.5 M $NaNO_3$ solution respectively, with the ratio of 20 ml solution per gram catalyst. Deionized water and commercial $NaNO_3$ (Sigma Aldrich, ACS Reagent, ≥ 99.0%) were used to prepare $NaNO_3$ solution. The mixture of NH_4-ZSM-5 powder and $NaNO_3$ solution was stirred for 12 h at room temperature. Then, the solution was centrifuged, and the solid part was washed five times with deionized water followed by a drying step at 80°C in a vacuum oven for 24 h.

Catalyst samples in ammonium form were calcined in flowing dry air at 600°C for 5 h with a heating rate of 2°C/min to obtain the proton-form zeolites. Protonated zeolites were then pelletized, crushed, and sieved to particles with sizes ranging from 90 to 250 μm. H-ZSM-5 zeolites with Si/Al = 40, Si/Al = 140, and sodium-titrated samples are denoted as MFI-40, MFI-

140, Na-MFI-40, and Na-MFI-140, respectively. H-Beta zeolite (Si/Al = 133) is denoted as BEA-133.

Catalyst characterization

IPA-TPD experiments

Temperature-programmed desorption (TPD) of isopropylamine (IPA) was carried out to determine the Brønsted acid site densities of the catalysts. The catalyst sample was packed in a quartz reactor (1/4″ OD) that was installed inside a temperature-controlled oven. The temperature of the catalyst bed was measured via a thermocouple attached to the outer wall of the reactor in the center of the catalyst bed. The exit of the reactor was connected with an MKS Cirrus 200 quadrupole mass spectrometer (MS) to analyze products. Catalyst samples were pretreated at 300°C for 1 h with a heating rate of 10°C/min using He as a carrier gas (20 ml/min) to remove physisorbed water in the catalyst. After pretreatment, the oven temperature was lowered to 100°C and 2 μL pulses of isopropylamine (Sigma–Aldrich, ≥ 99.5%) were manually injected into the reactor through a septum. The mass-to-charge ratios m/z = 44 at the outlet were monitored on an MKS Cirrus 200 quadrupole mass spectrometer (MS) to ensure that the catalyst surface was fully saturated with IPA. IPA pulses were continuously injected until the intensity of the peak m/z = 44 remained constant, indicating that the catalyst surface was saturated with IPA. Subsequently, physically adsorbed IPA was removed by flowing He through the catalyst bed at a rate of 20 ml/min at 100°C for 1 h. The temperature was then ramped from 100°C to 600°C at a rate of 10°C/min. Propylene (m/z = 41), ammonia (m/z = 17), and IPA (m/z = 44) desorbing from catalyst bed during temperature ramp were monitored via MS. Propylene desorbed during the temperature program was quantified through monitoring during the run with propylene response factors quantified by injecting a standard through a gas sample loop. The total moles of propylene

desorbed from the catalyst bed were assumed to be 1:1 stoichiometric with the number of Brønsted acid sites in the catalyst sample.

Nitrogen adsorption

Nitrogen adsorption analysis was conducted on a Micromeritics ASAP 2020 at liquid nitrogen temperature (-196°C). The catalyst sample was degassed at 350°C with a heating rate of 5°C/min in vacuum pressure for 10 h to remove moisture and volatile impurities. The weight of the dried sample was determined after degassing. Then, the sample was cooled down to -196°C for nitrogen adsorption analysis. The specific surface area of the catalyst sample was evaluated by Brunauer, Emmet and Teller (BET) method.

Thermogravimetric analysis

Thermogravimetric analysis (TGA) was performed on a Netzsch STA 449F1 equipped with a pin thermocouple and a Netzsch nano-balance to quantify the amount of coke formed on H-ZSM-5 catalysts during acylation reactions. Spent catalysts after acylation reactions were heated from room temperature to 300°C at the ramp rate of 10°C/min and held at 300°C for 1 h in flowing argon (40 ml/min) to remove physisorbed water in the spent catalysts. Then, temperature program oxidation (TPO) was carried out under flowing air (50 ml/min). The spent catalyst sample was heated from 40°C up to 800°C at the ramp rate of 10°C/min, held at 800°C for 230 min and cooled down to the original temperature of 40°C. The coke on the sample was determined by the weight loss of the sample after the TPO experiment.

Catalytic testing

Vapor phase flow reactions between m-cresol and acetic acid over H-ZSM-5 and H-BEA catalysts were conducted in a quartz tube reactor (1/4″ OD) at atmospheric pressure. The catalyst

sample was mixed with acid-washed glass beads and packed between quartz wool layers in the quartz reactor. The reactor was filled with acid-washed glass beads from the inlet of the reactor to the catalyst bed. The quartz reactor was installed inside a temperature-controlled oven. The temperature of the catalyst bed was controlled by a thermocouple inside the quartz reactor and beneath the catalyst bed. Helium with a flowrate of 125 ml/min was used as a carrier gas during catalyst pretreatment and flow reactions. Catalyst samples were heated to 300°C at the ramp rate of 10°C/min and held at 300°C for 1 h to remove physisorbed water in the catalyst. After pretreatment, the temperature of the oven was set to reach the desired reaction temperature. Reactants including m-cresol (Sigma Aldrich, 99%) and acetic acid (Sigma Aldrich, ACS reagent, ≥ 99.7%) were fed by KD Scientific syringe pumps through inlet septum. The inlet of the reactor was heated to create a vaporization zone for the liquid reactants. The outlet of the reactor was heated to 250°C to prevent condensation of products on the downstream tubing. Samples were collected at different reaction time-on-stream (TOS) by a gas sample loop connected with a six-port valve and products were analyzed by a Hewlett Packard 6890 gas chromatograph equipped with a flame ionization detector and an INNOWAX column (30 m × 0.25 mm).

Turnover frequency (TOF) and turnover number (TON) of the reaction are defined as follows:

$$\text{Turnover frequency} = \frac{\text{Mole of product formed per second per gram catalyst}}{\text{Brønsted acid site density (mol H}^{+}\text{per gram catalyst)}}\ (1/\text{s}) \qquad (1)$$

$$\text{Turnover number} = \int_0^t TOF(t)dt \qquad (2)$$

where TOF(t) is the turnover frequency at reaction time on stream t.

Yield of product formation in molar percentage is calculated as follows:

$$\text{Yield} = \frac{\text{Mole of product formed per second}}{\text{Mole of limiting reactant fed per second}} \text{ (mol\%)} \quad (3)$$

Initial turnover frequency and initial yield are used to decouple the intrinsic kinetic results from catalyst deactivation during continuous vapor phase flow reactions.

Results and discussion

Reaction order and activation energy measurements

The acylation of m-cresol with acetic acid over Brønsted acid sites forms two major products, including m-tolyl acetate and 2-hydroxy-4-methylacetophenone. It has been reported that the acylation between aromatics and acylating agents proceeds by acylium ion mechanism [36, 52]. Interestingly, aromatic ester such as m-tolyl acetate can be protonated by Brønsted acid sites in H-ZSM-5 zeolites and form acylium ions [55].

The formation of m-tolyl acetate over MFI-40 and MFI-140 with different catalyst amounts is shown in Fig. 1. It clearly shows that yields of ester formation during reaction time on stream over different amounts of MFI-140 and MFI-40 catalysts are stable and identical. This observation suggests that ester formation under the reaction conditions has reached thermodynamic equilibrium, which does not depend on the concentration of active sites on the catalyst. This result is consistent with prior results obtained in the liquid phase that suggested that the formation of ester from m-cresol and acetic acid over zeolites rapidly reaches equilibrium [51].

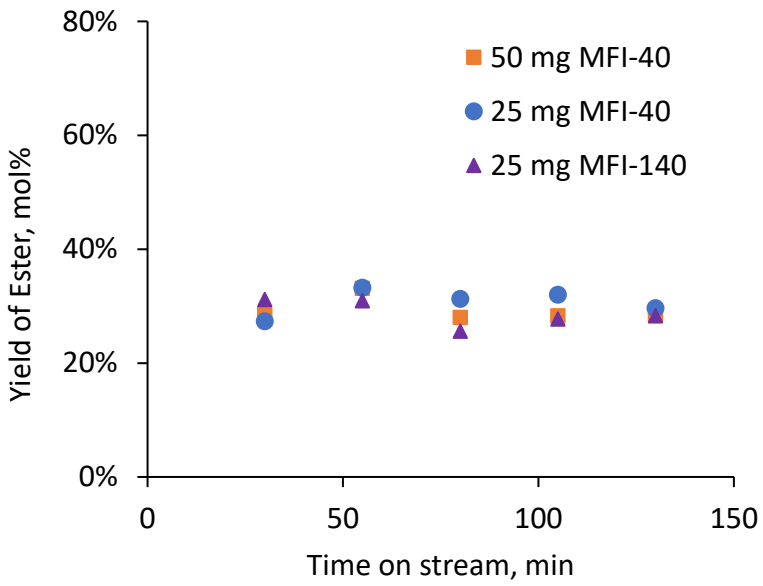

Fig. 1. Yield of m-Tolyl acetate formation in molar percentage using 50 mg MFI-40 (■), 25 mg MFI-40 (●), 25 mg MFI-140 (▲) at 250°C, $P_{acetic\ acid}$ = 1.4 kPa, $P_{m\text{-}cresol}$ = 0.3 kPa

It is important to study the reaction kinetics and the role of the intermediate ester under diffusion-free conditions, while also confirming that all sites have comparable intrinsic activity. It is also acknowledged that the presence of Lewis acid sites such as extra-framework aluminum species in low Si/Al zeolites could influence the confinement inside zeolite pores, the adsorption of reactants and products, and the interaction with reaction transition states, altering the catalytic activity of zeolites [56-58]. Table 1 shows that the Brønsted acid site densities of the low Si/Al MFI zeolites studied here are close to the theoretical numbers, indicating a low amount of extra-lattice aluminum species, and in good agreement with the previous report [59].

Table 1. Brønsted acid site densities of zeolites used in acylation reactions

Catalysts	Si/Al ratio	Brønsted acid site densitiy, mmol/g	
		Calculated [a]	IPA-TPD method
MFI-40	40	0.408	0.391

Na-MFI-40	40	-	0.153
MFI-140	140	0.118	0.106
Na-MFI-140	140	-	0.082
BEA-133	133 [b]	0.124	0.119

[a] Theoretical values based on framework Si/Al ratio

[b] Determined by ICP-OES method (Galbraith Laboratories)

The initial turnover frequency of 2-hydroxyl-4-methylacetophenone formation over H-ZSM-5 zeolites with varying Brønsted acid site densities is shown in Fig. 2. As expected, Brønsted acid site density increases with lowering Si/Al ratio in zeolites. In addition, it is well known that reaction Thiele modulus increases with catalyst particle size and reaction rate constant [60]. The latter is proportional to the acid site density of the catalyst. The higher the Thiele modulus, the lower the effectiveness factor, which may shift the reaction from surface-reaction-controlled regime to internal diffusion limitation regime. Therefore, acylation reactions over zeolites with high acid site densities are subject to internal mass transfer limitation.

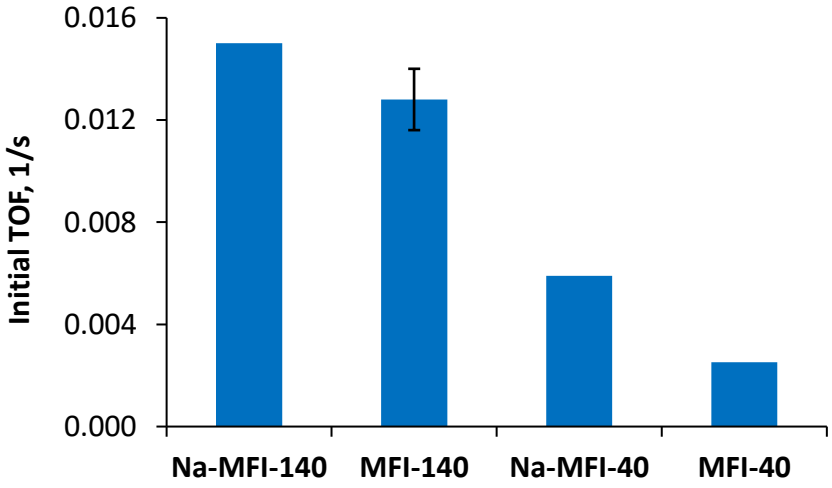

Fig. 2. Initial turnover frequency of 2-hydroxyl-4-methylacetophenone formation over different H-ZSM-5 zeolites at 250°C, $P_{acetic\ acid}$ = 1.4 kPa, $P_{m\text{-}cresol}$ = 0.3 kPa

As shown in Fig. 2, the lower turnover frequency of reactions on MFI-40 and Na-MFI-40 compared to MFI-140 and Na-MFI-140 suggests that the reaction over MFI-40 is limited by diffusion of reactants to the active sites. On the other hand, the similar initial turnover frequencies of acylated product formation over MFI-140 and Na-MFI-140 implies that the reaction over MFI-140 is not limited by internal diffusion.

The partial pressure of acetic acid and m-cresol were varied to further examine whether the reaction over MFI-140 is limited by internal diffusion. It is known that the catalyst surface cannot be saturated if it is diffusion-limited by the reactants, so the observed zero-order reaction regime would suggest the absence of internal diffusion corruptions to the reported rates, assuming the reaction order with respect to acetic acid or m-cresol is not negative first order.

The reaction order of 2-hydroxyl-4-methylacetophenone formation with respect to acetic acid at the reaction temperature of 250°C was determined by varying partial pressure of acetic acid while keeping partial pressure of m-cresol constant at 0.3 kPa. As shown in Fig. 3, the initial turnover frequency of 2-hydroxyl-4-methylacetophenone formation changes from first-order to zero-order with respect to acetic acid when the partial pressure of acetic acid increases. It indicates that the catalyst surface is saturated at the partial pressure of acetic acid equal to and higher than 1.4 kPa. In addition, these results indicate that the rates reported here with respect to acetic acid are not corrupted by the internal diffusion of acetic acid to the active sites under these conditions.

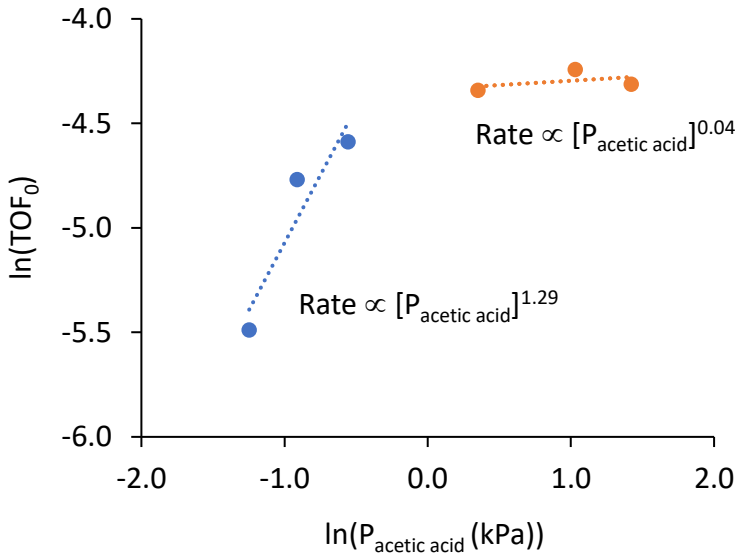

Fig. 3. Varying the partial pressure of acetic acid in acylation reaction with m-cresol over MFI-140 at 250°C, $P_{acetic\ acid}$ = 0.3 – 4.1 kPa, $P_{m\text{-}cresol}$ = 0.3 kPa. Rates of 2-hydroxyl-4-methylacetophenone formation are extrapolated to 0 min TOS.

The partial pressure of m-cresol was also varied to test the diffusion of m-cresol and unravel the acylation mechanism. Fig. 4 shows the initial turnover frequency of 2-hydroxy-4-methylacetophenone formation changes with varying partial pressure of m-cresol while keeping partial pressure of acetic acid constant at 1.4 kPa. As mentioned above, the rate of 2-hydroxyl-4-methylacetophenone formation is zero-order with respect to acetic acid and the catalyst surface is saturated at this partial pressure of acetic acid. Interestingly, the rate of 2-hydroxyl-4-methylacetophenone formation is also zero-order with respect to m-cresol when varying partial pressure of m-cresol from 0.3 kPa to 0.9 kPa. This evidence further suggests that the reaction rates obtained in this study are not influenced by the internal diffusion of m-cresol to the active sites. In addition, as the formation of m-tolyl acetate from m-cresol and acetic acid reaches thermodynamic equilibrium as shown in Fig. 1, this observation also implies that the catalyst surface is saturated by intermediate m-tolyl acetate under the reaction conditions.

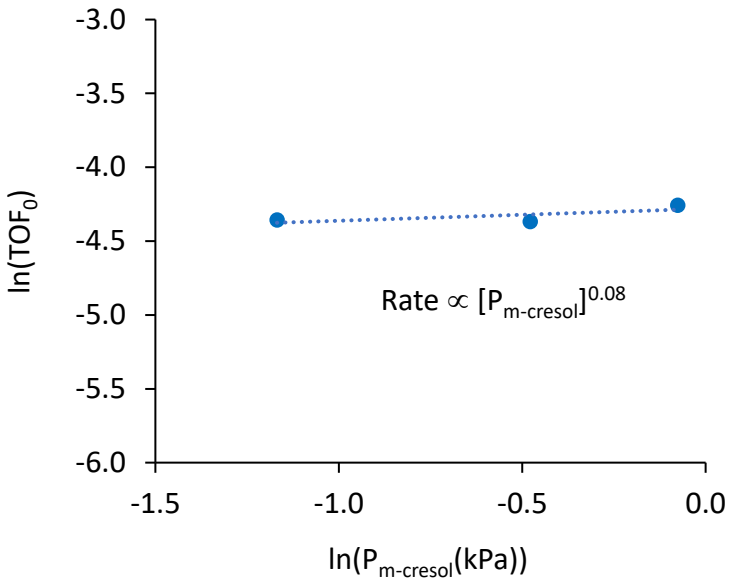

Fig. 4. Varying the partial pressure of m-cresol over MFI-140 at 250°C, $P_{acetic\ acid}$ = 1.4 kPa, $P_{m\text{-}cresol}$ = 0.3 – 0.9 kPa. Rates of 2-hydroxyl-4-methylacetophenone formation are extrapolated to 0 min TOS.

The activation energy of 2-hydroxyl-4-methylacetophenone formation was estimated by an Arrhenius plot over the temperature range of 200°C to 250°C. The reaction conditions were selected at the zero-order regime with respect to acetic acid and m-cresol to obtain the intrinsic activation energy of 2-hydroxyl-4-methylacetophenone formation, or the difference in energy between the adsorbed intermediate m-tolyl acetate on the surface and the acylium ion of the transition state. As shown in Fig. 5, the estimated true energy barrier is 41 kJ/mol. Interestingly, hybrid DFT calculations in our prior reports have shown that the true activation energy of acylium ion formation from acetic acid is 133 kJ/mol [43]. This energy barrier is much higher than the estimated activation energy of 2-hydroxyl-4-methylacetophenone formation of 41 kJ/mol. As mentioned above, m-cresol acylation with acetic acid proceeds through the intermediate ester m-tolyl acetate. Therefore, this result suggests that m-cresol interacts with acetic acid to form m-tolyl acetate, which leads to a lower intrinsic activation energy of acylium ion formation. This

observation implies the important role of ester intermediates in reducing the barrier for acylium ion formation. The flux of reactants upon comparison with the generated ester is further discussed in the following section.

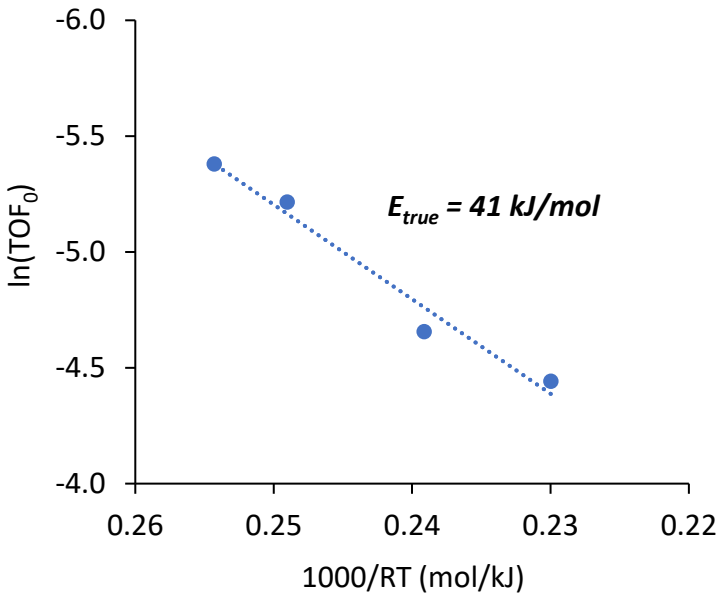

Fig. 5. The true activation energy of 2-hydroxyl-4-methylacetophenone formation on MFI-140 over temperature range of 200-250°C, $P_{acetic\ acid}$ = 1.4 kPa, $P_{m\text{-}cresol}$ = 0.3 kPa. Rates of 2-hydroxyl-4-methylacetophenone formation are extrapolated to 0 min TOS.

Kinetically relevant intermediate ester formed inside H-ZSM-5 zeolite pores

The reaction rate equation was derived based on the proposed acylation pathway via active intermediate ester (Appendix A1 - Section S3). There are two possible rate-limiting steps: acylium ion formation or C-C coupling to form the acylated product. If the acylium ion formation is the rate-determining step as derived in Appendix A1 - Section S3.1, the initial turnover frequency of 2-hydroxy-4-methylacetophenone increases with the partial pressure of acetic acid and then becomes independent of partial pressure of reactants. This proposed mechanism matches with the experimental data of varying partial pressure of acetic acid and m-cresol as shown in Fig. 3 and

Fig. 4. On the other hand, if the C-C coupling following Eley-Rideal the rate-determining step as shown in Appendix A1 - Section S3.2, the initial turnover frequency of 2-hydroxy-4-methylacetophenone would keep increasing linearly with the partial pressure of m-cresol, which is not consistent with the observation in Fig. 4. Therefore, it is concluded that adsorbed m-tolyl acetate is the most abundant surface intermediate under the reaction conditions, and acylium ion formation from ester decomposition on Brønsted acid sites is the rate-determining step of the acylation of m-cresol with acetic acid. The acylation initial rate equation for this proposed mechanism is as follows:

$$\frac{r_{initial}}{[H^+]_0} = \frac{k_6 K_1 K_2 P_{mC} P_{AC} / P_{H_2O}}{1 + \frac{K_1 K_2 P_{mC} P_{AC}}{P_{H_2O}}} \quad (4)$$

where k_6 is the rate constant of the acylium ion formation step; K_1 is the equilibrium constant of m-tolyl acetate formation; K_2 is the adsorption equilibrium constant of m-tolyl acetate on Brønsted acid sites in MFI-140 catalyst.

Based on the barrier observed under saturation conditions, it is proposed that the intermediate ester formation accelerates acylation reaction rates. In the liquid phase over H-Beta zeolites, directly feeding the intermediate ester m-tolyl acetate was shown to enhance acylation reaction rates when compared with feeding acetic acid alone [51]. To investigate this effect further in the vapor phase flow reactor employed here, m-tolyl acetate was used as an acylating agent in order to contrast reaction rates with acetic acid in acylation reaction with m-cresol under identical reaction conditions.

Fig. 6 shows the turnover frequency of 2-hydroxyl-4-methylacetophenone formation as a function of time on stream with varying acyl sources. The kinetic diameter of m-tolyl acetate (MW = 150 g/mol) is estimated to be 0.66 nm based on the work of Huber et al., while pore channels of

MFI zeolites are either 0.54 × 0.56 nm (straight circular channels) or 0.51 × 0.55 nm (sinusoidal elliptical channels) [61, 62]. While more accurate diffusion calculations would be required to truly assess diffusivity within the pores, this estimate combined with experimental observations indicates that the kinetically relevant m-tolyl acetate molecules are not those present external to the zeolite crystallite but are instead formed near the active site within the pores of the zeolite. Because the majority of sites in the zeolites studied here are in the larger channel intersections [21, 63], stabilization of these bulky transition states are likely favorable. Therefore, the proposed mechanism of acylation involves diffusion of smaller reactants, m-cresol and acetic acid, to the active sites, where the ester m-tolyl acetate forms directly at MFI channel intersections. These bulky ester molecules subsequently decompose on Brønsted acid sites to generate surface acylium ions, which acylate the ring of m-cresol to form the final acylated product.

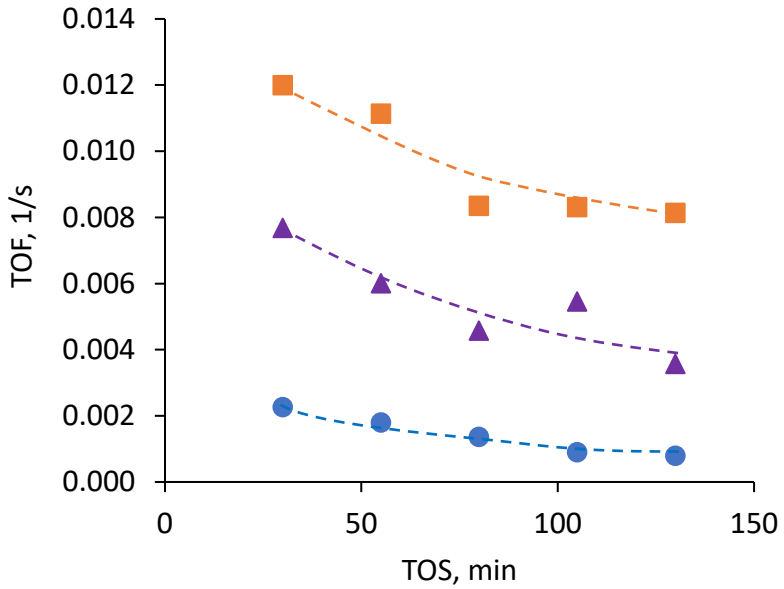

Fig. 6. The rate of 2-hydroxyl-4-methylacetophenone formation in reactions of m-cresol with acetic acid (■), m-tolyl acetate + water (▲), m-tolyl acetate (●) over MFI-140 at 250°C, $P_{m\text{-cresol}}$ = 0.3 kPa, $P_{acylating\ agent}$ = 1.4 kPa, P_{water} = 0.9 kPa. The dashed lines are a guide to the eye.

The diffusion of active intermediate m-tolyl acetate was further investigated by water co-feeding experiment. It is acknowledged that one potential disadvantage of direct acylation with carboxylic acids rather than utilizing anhydrides or acyl halides is the side product of water which is produced upon carboxylic acid dehydration. Water can promote the reverse reaction with surface acyl groups and limit the overall rate of products observed [46]. As discussed in previous studies, the negative influence of water on acylation and ketonization reactions can be due to the decreased concentration of surface acyl species, overall reaction equilibrium, or competitive adsorption [45, 46, 51]. In this case, however, the role of water is more intriguing. Results obtained upon co-feeding water along with m-tolyl acetate in acylation with m-cresol over MFI-140 at 250°C suggest the potential for water to accelerate rates when bulky ester molecules are involved, as shown in Fig. 6. Acetic acid is also observed when water is co-fed with m-tolyl acetate under reaction conditions. This result indicates that water facilitates the reverse esterification reaction to form acetic acid and m-cresol. These small reactant molecules diffuse through zeolite pores much faster than the bulky ester. The kinetically relevant ester is then formed from these acetic acid molecules and m-cresol at MFI channel intersections where Brønsted acid sites are located. Therefore, a positive influence of water on this reaction involves the ability to reversibly break the bulky ester, so faster diffusion of reactants to acid sites can occur where these ester molecules may form and decompose near the active sites.

The acylation of m-cresol with different acylating agents was carried out over a low acid site density H-Beta zeolite to further examine the diffusion of the active intermediate ester. Pore channels of BEA (~ 0.7 nm) are larger than channel intersections of MFI (~ 0.63 nm) pore channels of MFI (~ 0.51 – 0.56 nm) [19, 61, 62, 64]. Since the reaction over MFI-140 is not limited by internal diffusion, it is expected that the reaction over BEA-133 with similar Brønsted acid site

density is also free of diffusional effects. Fig. 7 illustrates that, counter to the case over MFI zeolites, the acylation of m-cresol with m-tolyl acetate has a higher turnover frequency when compared to the acylation of m-cresol with acetic acid. It is acknowledged that the net ester concentration in this case should be higher than that generated in equilibrium when co-feeding the acid and cresol independently due to the absence of co-fed water in the former case, which could help explain the increased rate observed upon co-feeding the ester. Nevertheless, it clearly shows the inverse trend when contrasted to MFI, that the ester indeed accelerates acylation rates whereas in smaller pored MFI feeding the ester alone without allowing equilibration leads to reduced rates. These results further imply that kinetically relevant m-tolyl acetate is formed at MFI channel intersections, followed by acylium formation from this active intermediate ester.

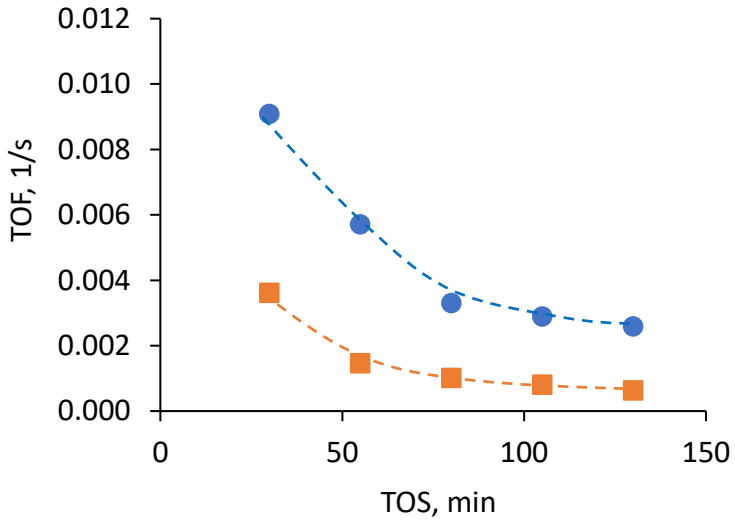

Fig. 7. The rate of 2-hydroxyl-4-methylacetophenone formation in reactions of m-cresol with acetic acid (■), m-tolyl acetate (●) over BEA-133 at 250°C, $P_{m\text{-}cresol}$ = 0.3 kPa, $P_{acylating\ agent}$ = 1.4 kPa, P_{water} = 0.9 kPa. The dashed lines are a guide to the eye.

It is also worth mentioning that the turnover frequency of the acylation of m-cresol with acetic acid over MFI-140 is higher than that on BEA-133 by comparing Fig. 6 and Fig. 7. The

diversity of confining void size of different zeolite frameworks such as MFI, BEA, FAU, TON was found to influence various reactions such as methanol dehydration, alkane cracking, and olefin oligomerization via the confinement effect [19, 20, 65]. Reactive intermediates and transition states are enthalpically stabilized by van der Waals interactions with the confining zeolite frameworks. Consequently, smaller void size in zeolites leads to a higher reaction rate, given that the reaction is not limited by the internal diffusion. Therefore, the higher acylation rate over MFI-140 compared to BEA-133 in this study could be attributed to confinement effects.

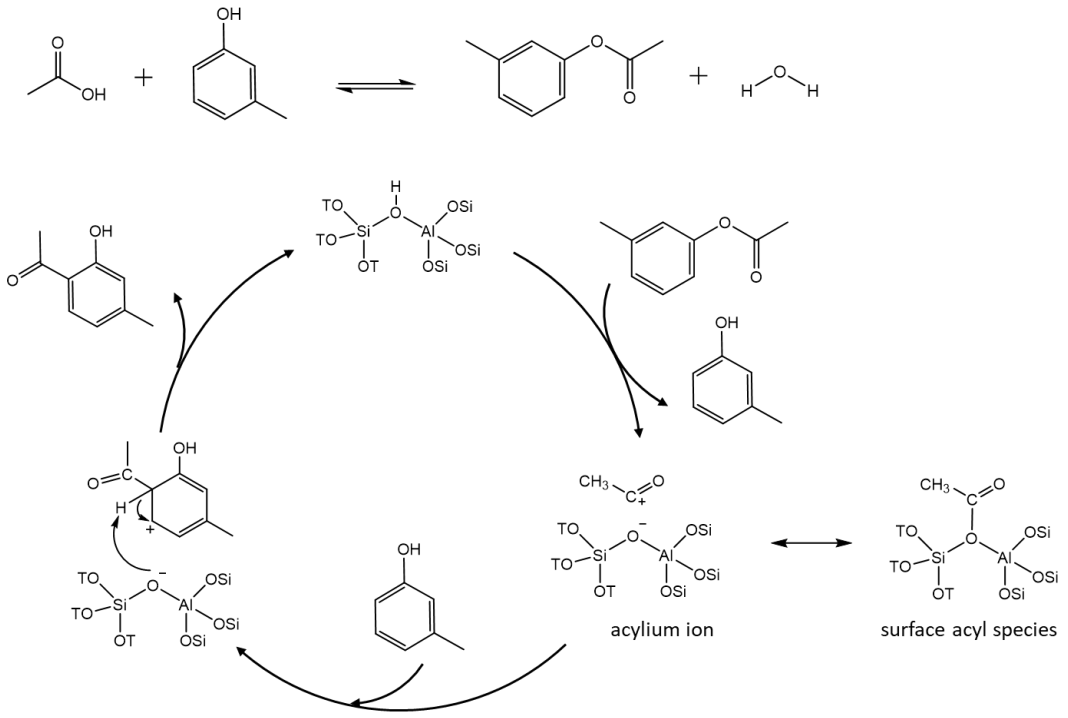

Scheme 1. Proposed mechanism of the acylation of m-cresol with acetic acid over Brønsted zeolites

Consequently, it has been proposed that the acylation of phenolic compounds such as m-cresol with acetic acid over zeolites proceeds through an intermediate ester (m-tolyl acetate) which decomposes on Brønsted acid site to form acylium ion, followed by the formation of the final

acylated product (2-hydroxyl-4-methylacetophenone). The proposed reaction mechanism is illustrated in Scheme 1.

Catalyst deactivation

Given the potential to form large coke forming species from both phenolic and carboxylic species, improving catalyst lifetime is of critical practical importance for acylation reactions. Bhan et al. suggested that catalyst turnover number (TON) is a more accurate way to describe the reaction progress than reaction time-on-stream (TOS), especially when catalyst deactivation is evaluated at different conversion levels [66-68]. Therefore, the turnover frequency of 2-hydroxyl-4-methylacetophenone formation was plotted as a function of the turnover number to evaluate catalyst deactivation at various partial pressures of acetic acid.

Condensation of ketene species often has been claimed to be the main cause of deactivation of zeolites during the acylation of aromatic compounds [52, 69]. Stockenhuber et al. has proposed that acylium ions during the acylation of anisole with acetic anhydride over H-Beta zeolite can desorb to gas phase, as ketene species, which can oligomerize to form coke-like products that block and poison catalyst active sites [52]. Iglesia et al. also attributed the deactivation of metal oxide catalyst during ketonization of carboxylic acids to gaseous ketene species [70]. On the other hand, Apesteguía et al. studied catalyst deactivation during the acylation of phenol with acetic acid over zeolites and suggested that catalyst deactivation is not due to ketene species but attributed to subsequent reactions of acylated products to form coke precursors [53]. Similarly, Guisnet et al., studying the acylation of anisole with acetic anhydride over H-Beta zeolite in liquid phase batch

reactor, found that the acylated product (p-methoxyacetophenone) is responsible for catalyst deactivation by blocking mesopores in H-Beta zeolite [54].

Fig. 8 shows the turnover frequency of 2-hydroxyl-4-methylacetophenone formation as a function of turnover number with varying partial pressure of acetic acid from 1.4 kPa to 4.1 kPa while maintaining the partial pressure of m-cresol of 0.3 kPa. It is noted that this is the zero-order regime with respect to both m-cresol and acetic acid and the initial partial pressure of 2-hydroxyl-4-methylacetophenone are the same under these reaction conditions. As a result, the influence of acylated product formation on catalyst deactivation has been ruled out when evaluating the reaction at comparable product yields. Interestingly, it shows that the higher the partial pressure of acetic acid in vapor phase reaction, the faster the catalyst deactivated. This result clearly suggests that the deactivation behavior of zeolite catalyst during acylation reaction is highly related to species formed from acetic acid.

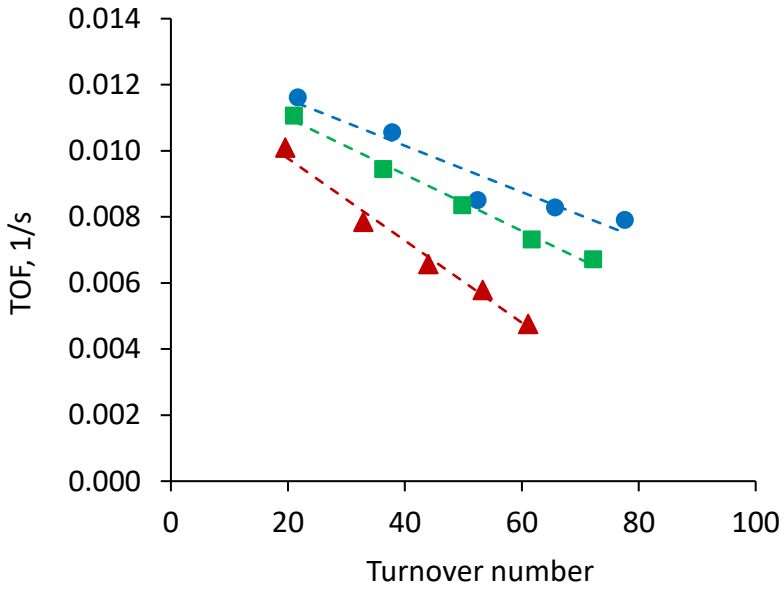

Fig. 8. Turnover frequency of 2-hydroxyl-4-methylacetophenone formation over MFI-140 as a function of cumulative catalyst turnover number at 250°C, $P_{m\text{-}cresol}$ = 0.3 kPa, $P_{acetic\ acid}$ = 1.4 kPa (●), $P_{acetic\ acid}$ = 2.8 kPa (■), $P_{acetic\ acid}$ = 4.1 kPa (▲). The dash lines are a guide to the eye.

It is known that small amounts of gaseous ketene species can form in equilibrium with surface acylium ions [32, 52]. As a result, the initial partial pressure of gaseous ketene species should be constant in the zero-order reaction regime in Fig. 8. Therefore, the faster catalyst deactivation at a higher partial pressure of acetic acid within the zero-order reaction regime implies that gaseous ketene species are unlikely to be the primary source of coke precursors, in this case. Hence, it is suggested that subsequent esterification of the acylated product (2-hydroxyl-4-methylacetophenone) with acetic acid is the major precursor to catalyst deactivation in the acylation of m-cresol with acetic acid over Brønsted zeolites. In fact, this observation is in agreement with proposals involving the acylation of phenol with acetic acid, where subsequent ester formation can occur with the final acylated product [53]. This increases the probability for subsequent CAC bond forming reactions such as aldol condensation or sequential acylation that will yield species that are too large to exit the zeolite micropores. Understanding how this product-acid interaction leads to subsequent C-C bond forming reactions that ultimately cause catalyst deactivation requires further investigation.

Conclusions

The acylation of m-cresol with acetic acid over MFI catalysts is a very interesting reaction that generates a highly reactive ester intermediate with a low diffusion rate within the pores. When MFI catalysts operate under conditions where rates are not affected by diffusion of reactants to active sites, ester intermediates are readily formed but their diffusion through the pores is slow. Interestingly, while the flux of the ester intermediate species is slow their role on reaction kinetics cannot be ignored, as the esters produced within the micropores of the zeolite enable a pathway for acylium ion formation that is energetically favored. Energy barriers measured under conditions at which active sites are saturated with the active intermediate m-tolyl acetate reveal the significant

role of the ester to modify rates of acylium ion formation. However, feeding the ester directly results in lower observed rates due to the significant diffusion limitations that they exhibit within MFI pores. This reversible process is observed by co-feeding water where m-tolyl acetate is hydrolyzed and rates are subsequently enhanced. Therefore, the kinetically relevant ester is formed inside zeolite pores where it readily decomposes on Brønsted acid sites to form an acylium ion at the transition state, leading to accelerated rates of 2-hydroxy-4-methylacetophenone formation.

Investigations into catalyst deactivation rates reveal that low Al content MFI catalysts (Si/Al = 140) exhibit intriguing behavior of increased deactivation rates even when acetic acid partial pressures are increased beyond saturation conditions. In these instances, the partial pressure of gaseous ketene species that are commonly attributed to deactivation is constant. Hence, the deactivation mechanism during the acylation of m-cresol with acetic acid is proposed to be related to subsequent esterification of the acylated product with acetic acid to form heavier compounds that become trapped within zeolite pores, ultimately leading to accelerated catalyst deactivation rates.

Acknowledgements

The authors would like to thank financial support from Honeywell-UOP Applied and Fundamental Project Award to carry out this research.

Chapter 3: Effect of water and acid site proximity on cumene dealkylation over H-ZSM-5 zeolites

All the data presented in this chapter is obtained at the University of Oklahoma. The pulse reaction experiment and discussion as a part of this work were performed by Dr. Tram Pham. This chapter will be submitted as a journal article using the citation: Han K. Chau, Abhishek Gumidyala, Tram N. Pham, Daniel T. Glatzhofer, Steven P. Crossley, "Effect of water and acid site proximity on cumene dealkylation over H-ZSM-5 zeolites".

Abstract

Cumene dealkylation over H-ZSM-5 zeolites is influenced by the presence of adjacent Brønsted acid sites and water molecules inside zeolite pores. The reaction turnover frequency over paired acid sites was found to be 6-times higher than that on isolated acid sites at the reaction temperature of 300°C. Co-feeding water enhances the reaction rate of cumene dealkylation over H-ZSM-5 zeolites, which is likely related to the delocalization of framework protons by water molecules to generate hydronium ion clusters, leading to a looser transition state and possibly extend the range of interaction between two Brønsted acid sites. Both effects of water and acid site proximity on improving reaction rate were attributed to higher transition state entropy. This direct participation of water is contrasted with water-induced modifications to the catalyst surface, such as the generation and mobility of extra-lattice species. These features have been shown to influence reaction rates for more demanding chemical transformations such as alkane cracking but do not significantly influence rates for the facile dealkylation chemistry studied here. We further reveal how the addition of moisture also induced positive consequences on catalyst stability by limiting subsequent oligomerization reactions with formed products.

Introduction

Collective understanding of the role of water in acid catalyzed chemistry is continuously evolving. Water has been traditionally considered a simple diluent for gas phase cracking chemistry, but it may not be a simple benign spectator [71]. Local perturbations to the zeolite structure induced by water can significantly alter the environment around protons through the creation of extra-lattice species, and consequentially significantly modify activity for demanding transformations such as alkane cracking. It has also been reported that water may directly influence rates of certain reactions, such as alcohol dehydration [28], by creating more stable hydrogen bound surface intermediate species. Interactions of water that modify reaction rates of more facile reactions with hydrocarbons, such as dealkylation of aromatics, have not been explored to the same extent. Practical considerations, however, necessitate a more detailed understanding of the impact that water has on this type of chemistry. Dealkylation of aromatics has a profound impact on benzene yield in fluidized catalytic cracking, as well as emerging applications such as the catalytic conversion of polystyrene to value-added products.

Dealkylation of alkylbenzenes over zeolites has been studied for many years as this is a critical reaction involved in the production of a variety of high value chemicals [72-75]. In fact, cumene dealkylation has been used as a test reaction to characterize catalyst acidity and study the mechanism of industrial catalytic cracking since the early 1950s [76]. While both reaction products, benzene and propylene, are high-value commodity chemicals, the formation of benzene is of great interest to crude oil refineries due to benzene concentration limits in gasoline. However, there have been only a few attempts to elucidate the mechanism of cumene dealkylation over zeolites [76, 77]. The influence of water on cumene dealkylation has not been investigated in the

literature, although steam is normally used to transport vaporized feed streams with a powdered catalyst up a riser and strip hydrocarbon products from catalyst particles.

Zeolites are among the most industrially important solid acid catalysts that have been used in various chemical transformations for several decades [2]. The presence of aluminum in a zeolite framework creates a negative charge that is neutralized by cations such as protons or metals. Recently, the distribution of aluminum in terms of crystallographic unique T-site location and proximity between aluminum species has attracted much attention [3]. In fact, the proximity of Brønsted acid sites influences many reactions such alkane cracking, olefin oligomerization, aldol condensation, and alcohol dehydration [26-30, 78]. Vicinal Brønsted acid site has been reported to modify the turnover frequency of some hydrocarbon transformations by increasing activation entropy [26, 29, 30], while modified stability of the active intermediate and a shift in the reaction pathways have been reported for the presence of paired sites in the case of alcohol dehydration [28]. In terms of acid strength, it was reported by Iglesia and co-workers that the strength of the Brønsted acid site in zeolites does not significantly depend on acid site density in MFI framework zeolites, framework structure, or proton location [21, 79]. Instead, rates were reported to correlate to the greatest extent with the local confining environment around the transition state. Unraveling these effects is quite challenging, as lowering the Si/Al ratio of a zeolite in its protonated form increases the Brønsted acid site density. This often leads to both an increase in the concentration of paired sites, as well as modifications to the location of acid sites. The confining local environment around a Brønsted acid site has been shown to influence the catalytic activity of zeolite catalysts in many reactions such as alkane cracking and alcohol dehydration [19, 20, 80]. The presence of extra-framework aluminum species is another important factor which could alter

the local environment around an acid site while also influencing reaction transition states, leading to the changes in catalytic activity by entropic or enthalpic stabilization [56, 57, 81-83].

The effect of water on zeolite structure and catalytic reactivity has been studied extensively for both liquid and vapor phase reactions [4-8]. In terms of zeolite structure stability, the hydrolysis of Si-O-Si and Si-O(H)-Al, as well as amorphization at silanol defects, can occur depending on the phase of water and reaction temperature, leading to a loss of crystallinity and catalyst destruction. The presence of water molecules inside zeolite pores can influence reactivity by changing mass transfer properties of reactants and products, enthalpic stabilization of reactants or transition states through solvation, facilitating proton transfer, and remote bond polarization [4, 78, 84]. On the other hand, it is known that water molecules facilitate proton delocalization at Brønsted acid sites and form hydronium ion clusters around the framework site [14-16]. The presence of a delocalized proton in a hydronium ion cluster created by the presence of water near a conventional Brønsted acid site in zeolites is capable of catalyzing aqueous phase reactions such as cyclohexanol dehydration and alkylation of phenolic compounds with alcohols [85-88]. Hydronium ions have been proposed to generate a highly local ionic environment that can modify transition states for some reactions, but this effect becomes less pronounced at high concentrations of hydronium ion clusters due to spatial constraints [18]. The role of water on zeolite catalyst stability is intriguing. While enhancing catalyst lifetime by co-feeding water has been generally attributed to competitive adsorption of water molecules [11, 12], it was reported for methanol-to-hydrocarbon reactions that water could reduce catalyst deactivation by shifting the equilibrium constants of surface intermediates, effectively decreasing the rate of initiation and termination reactions that ultimately lead to catalyst deactivation [13].

Here we report the enhancement of reaction rates and changes in catalyst stability during cumene dealkylation over H-ZSM-5 zeolites in the presence of paired acid sites and water, which contrasts with the inhibition effect of water on a more demanding alkane cracking reaction reported in our previous work [82]. This motivated us to systematically study the effect of water and acid site proximity on the intrinsic kinetic constants associated with cumene dealkylation over H-ZSM-5 zeolites. Different H-ZSM-5 zeolites with varying fractions of paired acid sites were used as catalysts for cumene dealkylation in the absence and presence of co-fed water. Extra-framework aluminum species were removed to decouple the roles water and acid site proximity from the presence of extra-lattice species on catalytic activity and catalyst deactivation during cumene dealkylation over H-ZSM-5 zeolites.

Experimental

Catalyst preparation

ZSM-5 zeolites with different Si/Al ratios (CBV-2314 with Si/Al = 11.5, CBV-3024E with Si/Al = 15, CBV-5524G with Si/Al = 25, CBV-8014 with Si/Al = 40, CBV-28014 with Si/Al = 140) were purchased in ammonium forms from Zeolyst International. In order to decouple the role of extra-framework aluminum species (EFAL) from site proximity, ZSM-5 catalyst with a Si/Al =11.5 was treated by $(NH_4)_2SiF_6$ (AHFS, Sigma-Aldrich, 99.999%, trace metals basis) solution [56]. A mixture of 2.06 g of NH_4-ZSM-5 and 1.92 g of AHFS was dissolved in 80 ml of water. The amount of AHFS was about four times the amount of aluminum in NH_4-ZSM-5 (Si/Al = 11.5). The solution was stirred vigorously at 80°C for 5 h. The solution was centrifuged, and the solid part was washed five times with hot deionized water, followed by drying step at 80°C in a vacuum oven for 15 h.

All catalyst samples were calcined in flowing dry air with a ramping rate of 2°C/min up to 600°C and kept at that temperature for 5 h to obtain proton-form H-ZSM-5. Protonated zeolites were then pelletized, crushed, and sieved to particles with sizes ranging from 90 to 250 μm. H-ZSM-5 zeolites with Si/Al = 11.5, Si/Al = 40, and Si/Al = 140 are denoted as MFI-11.5, MFI-40, and MFI-140, respectively. The catalyst sample after AHFS treatment is denoted as AHFS-MFI-11.5.

Catalyst characterization

Temperature-programmed reaction of isopropylamine (IPA-TPRx) in combination with an MKS Cirrus 200 quadrupole mass spectrometer (MS) was carried out on catalyst samples to determine Brønsted acid site (BAS) densities of these catalysts. The details of this method is described elsewhere [89].

Fourier-transform infrared (FT-IR) spectroscopy was carried out using a PerkinElmer Spectrum 100 Fourier Transform Infrared (FT-IR) spectrometer equipped with a high-temperature diffuse reflectance Infrared Fourier Transformation (DRIFT) CaF_2 cell (HVC, Harrick). A blank run using a KBr pellet was obtained for the background. Catalyst samples were ground and pressed into a sample holder equipped with a thermocouple. The sample was pretreated at 300°C for 1 h using He as a carrier gas to remove physically adsorbed water in the catalyst. FT-IR spectra of MFI-11.5 and AHFS-MFI-11.5 were obtained at 300°C.

Catalytic testing

Vapor phase flow reactions at atmospheric pressure over H-ZSM-5 catalysts were conducted in a quartz tube reactor (1/4" OD). The catalyst was mixed with acid-washed glass beads and packed between quartz wool layers in the quartz reactor. The quartz reactor was installed

inside a temperature-controlled oven. The temperature of the catalyst bed was controlled by a thermocouple located inside the quartz reactor beneath the catalyst bed. Catalyst samples were pretreated at 300°C for 1 h with helium as a carrier gas (125 ml/min) to remove physisorbed water in the catalyst. After pretreatment, the temperature of the oven was set to reach the reaction temperature. Cumene (Sigma Aldrich, 98%) and de-ionized water were fed through inlet septa into the reactor using KD Scientific syringe pumps. The inlet of the reactor was heated to create a vaporization zone for the liquid reactants. The outlet of the reactor was heated to 250°C to prevent condensation of products on the downstream tubing. Samples were collected at different reaction time on stream (TOS) using a gas sample loop connected with a six-port valve and products were analyzed using a Hewlett Packard 6890 gas chromatograph equipped with a flame ionization detector and an INNOWAX column (30 m × 0.25 mm).

A micro-pulse reactor was used to measure the catalytic activity for cumene dealkylation to minimize the influence of catalyst deactivation. Pelletized H-ZSM-5 (5 mg, Si/Al = 11.5) mixed with 95 mg glass beads was utilized for the reaction. After the catalyst was pretreated at 300°C for 1 h, several pulses of 0.15 μmol cumene, diluted in N_2, were sent over the catalyst bed at a 75 ml/min N_2 flowrate. The volume of the sample loop was 500 μmol and the partial pressure of cumene in the loop was 1.17 kPa. After conversion was measured for cumene dealkylation on the parent zeolite, pulsing water was utilized to treat the catalyst under conditions that lead to a significant enhancement for the rates of alkane cracking reactions [82]. The catalyst was exposed to 20 pulses of vapor water at 480°C and then dried overnight. Each pulse contains 2.85 μmol of water at a partial pressure of 18.6 kPa. The detailed conditions for this treatment are listed elsewhere [82]. The temperature of the pulse reactor was then reduced to a reaction temperature

of 300°C to measure the reactivity for cumene dealkylation. Products of the reaction were analyzed by GC-FID as previously described.

To decouple kinetic effects from catalyst deactivation over the reaction time on stream in flow reactions, all of the reaction rates were extrapolated to zero-time on stream to obtain initial rates. Turnover frequency (TOF) and turnover number (TON) for a reaction are defined as follows:

$$\text{Turnover frequency} = \frac{\text{Reaction rate (mol of cumene converted per second per gram catalyst)}}{\text{Brønsted acid site density (mol H}^{+}\text{ per gram catalyst)}} \text{ (1/s)} \quad (5)$$

$$\text{Turnover number} = \int_0^t TOF(t)dt \quad (6)$$

where TOF(t) is the turnover frequency at the reaction time on stream t.

Results and discussion

Cumene dealkylation over H-ZSM-5 zeolites in the absence of water

Cumene dealkylation has been proposed to occur on Brønsted acid sites through cleavage of the C-C bond of a protonated cumene molecule to form benzene and a propyl carbocation that can desorb to form propylene [76]. Therefore, the products of cumene dealkylation are benzene and propylene with expected stoichiometric 1:1 molar ratio. Catalytic activities of H-ZSM-5 zeolites with different features such as Brønsted acid site distribution, location, and the presence of extra-framework aluminum species were investigated in cumene dealkylation. Brønsted acid site densities of H-ZSM-5 zeolites used in this study are shown in Table 2.

Table 2. Brønsted acid site densities of H-ZSM-5 zeolites used in cumene dealkylation

ZSM-5 zeolites	Si/Al ratio	Brønsted acid site densitiy, mmol/g	
		Calculated [a]	IPA-TPRx method
MFI-140	140	0.118	0.106

MFI-40	40	0.408	0.391
MFI-25	25	0.644	0.502
MFI-15	15	1.050	0.733
MFI-11.5	11.5	1.348	1.094
AHFS-MFI-11.5	-	-	0.985

[a] Theoretical Brønsted acid site densities were calculated from framework Si/Al ratio

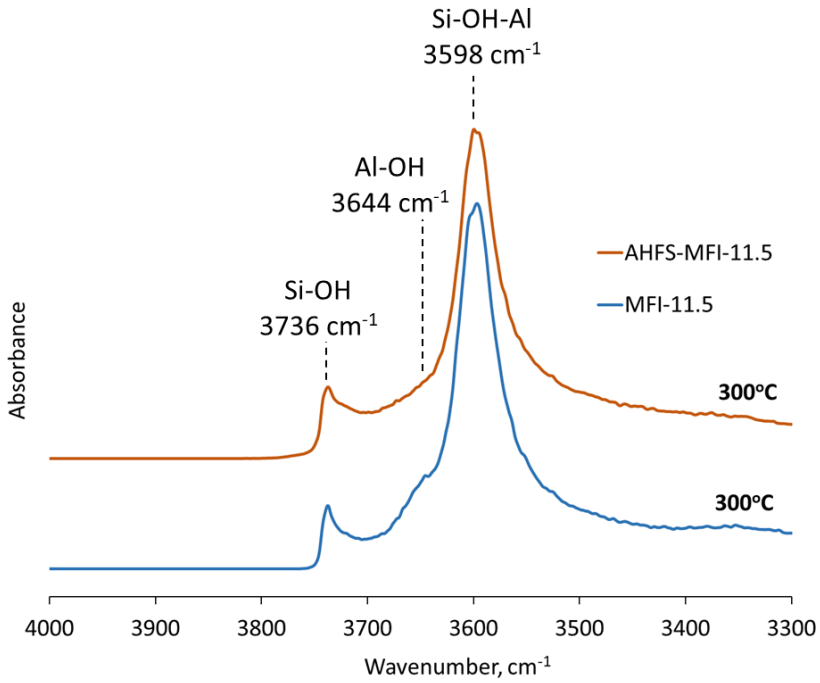

Fig. 9. FT-IR spectra of MFI-11.5 and AHFS-MFI-11.5 measured at 300°C. Absorbance intensity of catalyst samples were normalized based on the peak of Brønsted acid site (Si-O(H)-Al) and Brønsted acid site density obtained from IPA-TPRx

FT-IR spectra in Fig. 9 shows a peak corresponding to extra-framework aluminum species in MFI-11.5 at wavenumber of 3643 cm^{-1}, located between typical bands for surface silanol (≡Si–(O–H)) at 3737 cm^{-1} and surface Brønsted acid sites (≡Si–(O–H)–Al≡) at 3596-3599 cm^{-1}, while the peak of extra-framework aluminum species is not present in AHFS-MFI-11.5. These results

indicate that extra-framework aluminum species have been removed successfully by AHFS treatment, while the vast majority of the Brønsted acid sites were preserved.

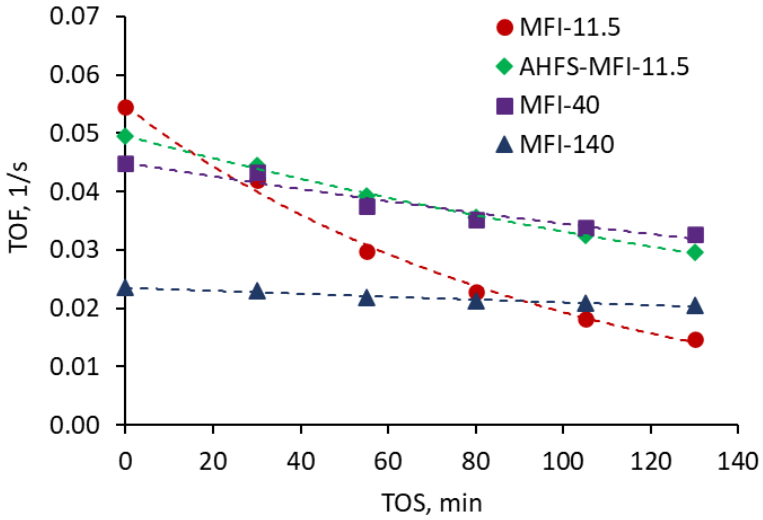

Fig. 10. Rate of cumene dealkylation over different zeolites at reaction temperature of 300°C as a function of time on stream (TOS), P_{cumene} = 0.5 kPa

As shown in Fig. 10, the initial rate normalized per proton, or turnover frequency (TOF), on different H-ZSM-5 zeolites for cumene dealkylation exhibits the following order: MFI-11.5 > AHFS-MFI-11.5 > MFI-40 > MFI-140. The intrinsic reactivity appears to strongly depend on the location and distribution of Brønsted acid sites. It has been previously reported that Brønsted acid sites are favorably located at large pore intersection voids in low Brønsted acid site density zeolites such as MFI-140 and MFI-40 [21]. Based on this, one could assume that Brønsted acid sites are located in more confined straight channels and sinusoidal channels in zeolites with lower Si/Al ratios such as MFI-11.5 and AHFS-MFI-11.5 catalysts. In addition, the amount of extra-framework aluminum species in MFI-40 and MFI-140 is negligible because the measured framework Brønsted acid site densities by IPA-TPRx are very close to the theoretical values.

Therefore, the significantly higher reaction rate over MFI-40 compared to MFI-140 suggests that the distribution of Brønsted acid sites plays the dominant role on the rate of cumene dealkylation.

Wichterlová and co-workers reported that the distribution of proximate framework Brønsted acid sites in ZSM-5 zeolites can be probed by Co^{2+} ion exchange [90]. This method was applied by other research groups illustrating the correlation between proximate framework Brønsted acid sites, or paired sites, and Si/Al ratios [26, 91, 92]. The fraction of paired sites decreases with an increase of Si/Al ratio, or a lowering of the Brønsted acid site density, of H-ZSM-5 zeolites as shown in Fig. 11. There is an insignificant number of paired sites in the MFI-140 catalyst. On the other hand, a significant number of Brønsted acid sites in MFI-40 and MFI-11.5 are paired, or in close proximity, based on Co^{2+} exchange coupled with UV-Vis measurements. In addition, there is only a small loss of the Brønsted acid site density in AHFS-MFI-11.5 (10%) after acid treatment when compared to the parent zeolite MFI-11.5. Therefore, it is expected that the number of paired sites in AHFS-MFI-11.5 is smaller than that in MFI-11.5, but still significant.

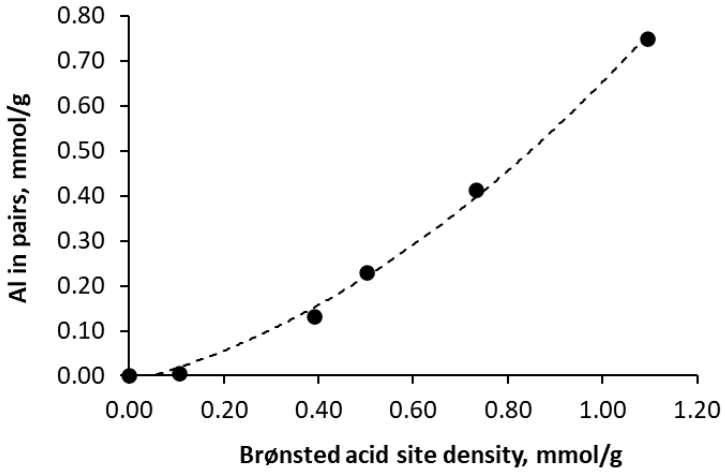

Fig. 11. Correlation of Brønsted acid site density with the amount of aluminum in pairs in different H-ZSM-5 zeolites. Fraction of aluminum in pairs was obtained from literature [91]

It is acknowledged that the fraction of extra-framework aluminum species in H-ZSM-5 zeolites with low Si/Al ratios like MFI-11.5 is considerable. However, the similar turnover frequency between MFI-11.5 and AHFS-MFI-11.5 implies that extra-lattice species do not play the most critical role on cumene dealkylation under these reaction conditions. Therefore, it is suggested that cumene dealkylation rate is strongly influenced by the presence of Brønsted acid sites in close proximity. In addition, the higher turnover frequency over the low Si/Al MFI-11.5 compared to the high Si/Al MFI-40 and MFI-140 implies that reactions over these catalysts are unlikely to be limited by internal diffusion.

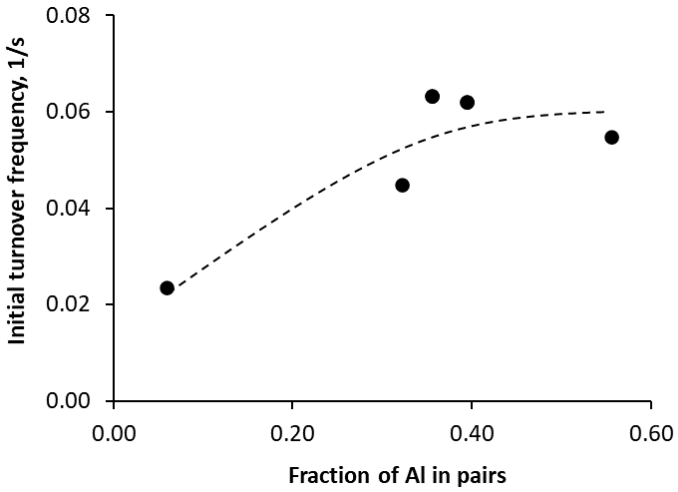

Fig. 12. Cumene dealkylation rate as a function of fraction of aluminum in pairs in H-ZSM-5 zeolites at 300°C, P_{cumene} = 0.5 kPa. The dash line is a guide to the eye.

It is evident from Fig. 12 that paired Brønsted acid sites play an important role in cumene dealkylation as reaction turnover frequency increases with the fraction of aluminum in pairs in H-ZSM-5 zeolites. However, the increase in turnover frequency of cumene dealkylation with respect to fraction of aluminum in pairs levels off as the fraction of paired sites is higher than 0.5 in MFI-11.5. By assuming the measured turnover frequency of cumene dealkylation is the weighted average of turnover frequency on two different types of active sites: isolated sites and paired sites,

and the reaction rates over isolated sites and paired sites in H-ZSM-5 zeolites are not markedly varied with site locations for Si/Al ≥ 15, the linear regression line in Fig. 13 can be described by following equations:

$$TOF = TOF_i X_i + TOF_P X_p \quad (7)$$

$$TOF = TOF_i(1 - X_p) + TOF_P X_p = (TOF_P - TOF_i)X_p + TOF_i \quad (8)$$

where TOF_i and TOF_p are average turnover frequency on isolated sites and paired sites respectively; X_i and X_p are the fractions of aluminum in isolated and paired sites, respectively.

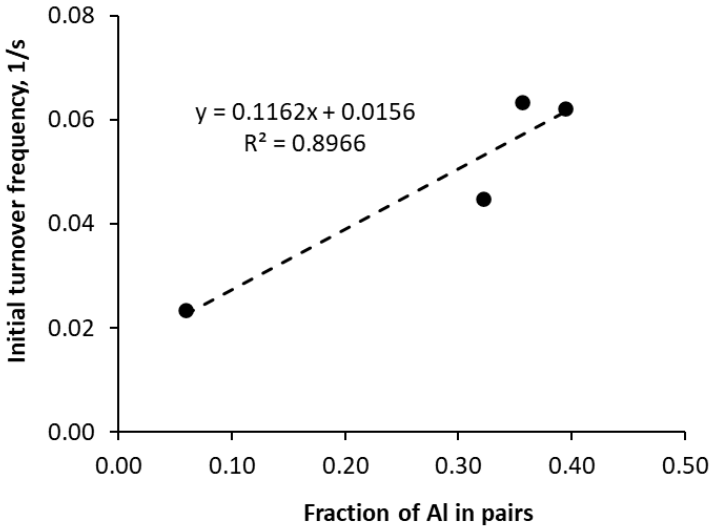

Fig. 13. Linear regression fitting of cumene dealkylation rate versus function of fraction of aluminum in pairs in H-ZSM-5 zeolites (Si/Al ≥ 15) at 300°C, P_{cumene} = 0.5 kPa.

Based on the equation and linear regression fitting of data points in Fig. 13, the average turnover frequency of cumene dealkylation on paired sites in H-ZSM-5 zeolites is approximately 6-times greater than that on isolated sites at the reaction temperature of 300°C. In addition, the enhancement effect of paired sites becomes less pronounced as the number of aluminum pairs or Brønsted acid sites density increases to higher values, such as in the case of MFI-11.5. It is well-

known that the location of Brønsted acid sites in H-ZSM-5, which can be either at channel intersections or in more confined straight and sinusoidal channels, strongly depends on the Si/Al ratio of zeolite samples. However, there is inconsistency in the literature regarding the shift in location of Brønsted acid sites with varying Si/Al ratios in H-ZSM-5 zeolites. Iglesia and co-workers reported that Brønsted acid sites become located in more confined pore channels in H-ZSM-5 zeolites with Si/Al > 23 [21]. The fact that turnover frequency of cumene dealkylation does not keep increasing with the fraction of paired acid sites suggests that the location of paired acid sites could influence the catalytic activity of these sites. This is further clarified in Fig. 14 where reaction rates are normalized by the fraction of aluminum in pairs.

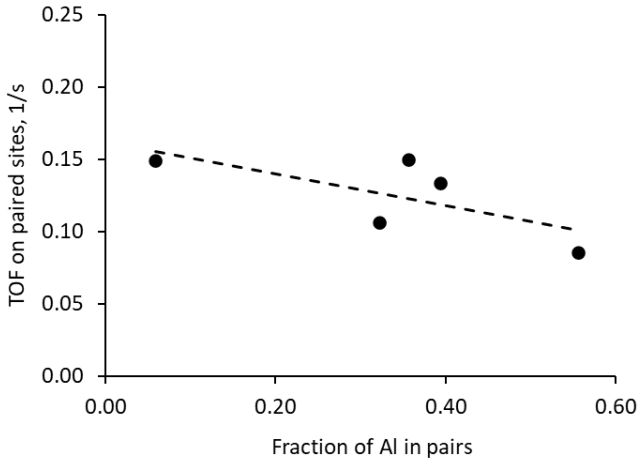

Fig. 14. Cumene dealkylation turnover frequency on paired sites as a function of fraction of aluminum in pairs in H-ZSM-5 zeolites at 300°C, P_{cumene} = 0.5 kPa. The dash line represents a linear regression fitting of data points

The turnover frequency on paired sites decreases with increasing the fraction of aluminum in pairs in H-ZSM-5 zeolites (Fig. 14). This observation suggests that the effect of site proximity on cumene dealkylation is not likely due to enthalpic effects as the higher fraction of aluminum in pairs leads to more acid sites located in more confined pore channels where it would have higher

enthalpic stabilization. Therefore, it is speculated that the reactivity of paired sites depends on the location of these active sites, whether they are at channel intersections or in more confined straight and sinusoidal channels. This catalytic activity enhancement is likely related to the entropic effects of having Brønsted acid sites in close proximity on cumene dealkylation rates as discussed later.

Kinetic effect of co-feeding water in cumene dealkylation

In this section, the effect of water is investigated based on water co-feeding experiments in cumene dealkylation over different H-ZSM-5 zeolites. It can be seen from Fig. 15 that water helps to enhance the turnover frequency of cumene dealkylation over all studied catalysts. However, the effect of water in reaction over isolated Brønsted acid sites in MFI-140 was less pronounced and required a higher reaction temperature than other H-ZSM-5 zeolites (Fig. 15 and Fig. 16). Interestingly, this enhancement effect of water is reversible, as shown by intermittent water co-feeding experiments. These results suggest that the influence of water on cumene dealkylation is due to the stabilization of reaction intermediates or transition states rather than inducing any irreversible change to the zeolite structure.

Irreversible changes to the zeolite by exposure to water vapor under more severe conditions are well-known. Zeolites undergo dealumination in the presence of water vapor at a high temperature (≥ 450°C) [93], which is much higher than the reaction temperature in our study. In addition, the increase of turnover frequency with water co-feeding provides further evidence to suggest that cumene dealkylation over the zeolite samples in this study is not limited by diffusion of reactants to active sites under these reaction conditions.

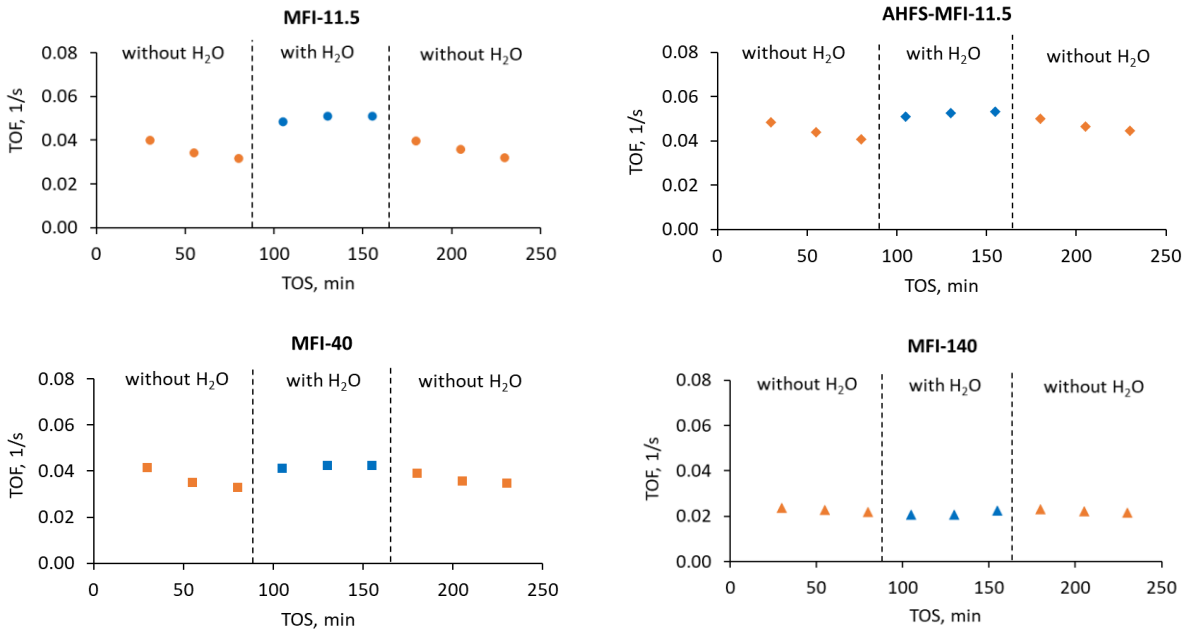

Fig. 15. Cumene dealkylation with intermittent water co-feeding over MFI-11.5, AHFS-MFI-11.5, MFI-40, and MFI-140 at T = 300°C, P_{cumene} = 0.5 kPa, P_{water} = 0 – 3.5 kPa

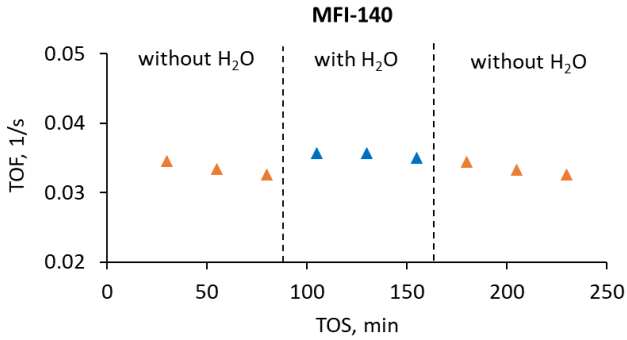

Fig. 16. Cumene dealkylation with intermittent water co-feeding over MFI-140 at T = 350°C, P_{cumene} = 0.5 kPa, P_{water} = 0 – 3.5 kPa

To decouple the effect of water on reaction kinetics from catalyst deactivation, initial rates in separate reaction runs with and without water co-feeding were determined by extrapolating to 0-minute TOS. Table 3 clearly shows that co-feeding water facilitates cumene dealkylation over different zeolites to different extents. Reaction over MFI-11.5 exhibits the most significant

enhancement in rate per proton from water co-feeding, followed by AHFS-MFI-11.5 and MFI-40, respectively. Kinetic analysis by measuring reaction order, activation energy, and activation entropy of cumene dealkylation reveals the reason for this enhancement effect of water present inside zeolite pores, as described in the following section.

Table 3. Initial turnover frequency (1/s) and rate enhancement percentage of cumene dealkylation over different zeolites in the absence and presence water at 300°C

Catalysts	**MFI-11.5**	**AHFS-MFI-11.5**	**MFI-40**
P_{water} = 0 kPa	0.055	0.050	0.045
P_{water} = 3.5 kPa	0.073	0.063	0.056
Rate enhancement, %	32.7	26.0	24.4

Kinetic role of paired Brønsted acid sites and water

The partial pressure of cumene was varied to determine reaction order with respect to cumene in the absence and presence of water. The reaction order of cumene dealkylation over different zeolites is first-order with respect to cumene (Fig. 17). The first-order reaction with respect to partial pressure is in agreement with previous proposals that C-C bond cleavage of adsorbed cumene is the rate-determining step [76, 77]. It is evident that cumene molecules undergo significant rates of dealkylation at temperatures below 300°C, which is much lower than those required to obtain comparable rates for alkane cracking, where protonation is far more demanding [26, 56, 57, 81].

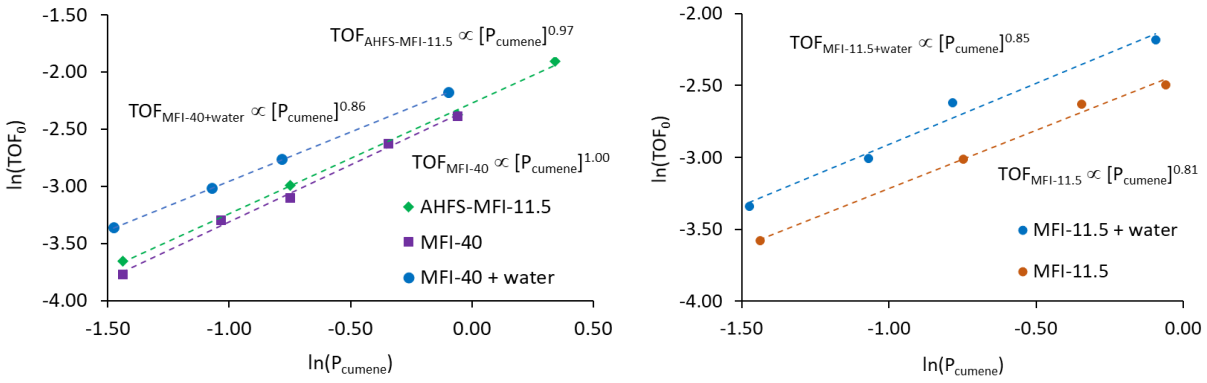

Fig. 17. Reaction order of cumene dealkylation over different zeolites in the absence of water (P_{water} = 0 kPa) and presence of water (P_{water} = 3.5 kPa) at 300°C

Apparent activation energy of cumene dealkylation over different zeolites with and without water co-feeding measured over the temperature range from 250°C to 300°C is shown in Fig. 18.

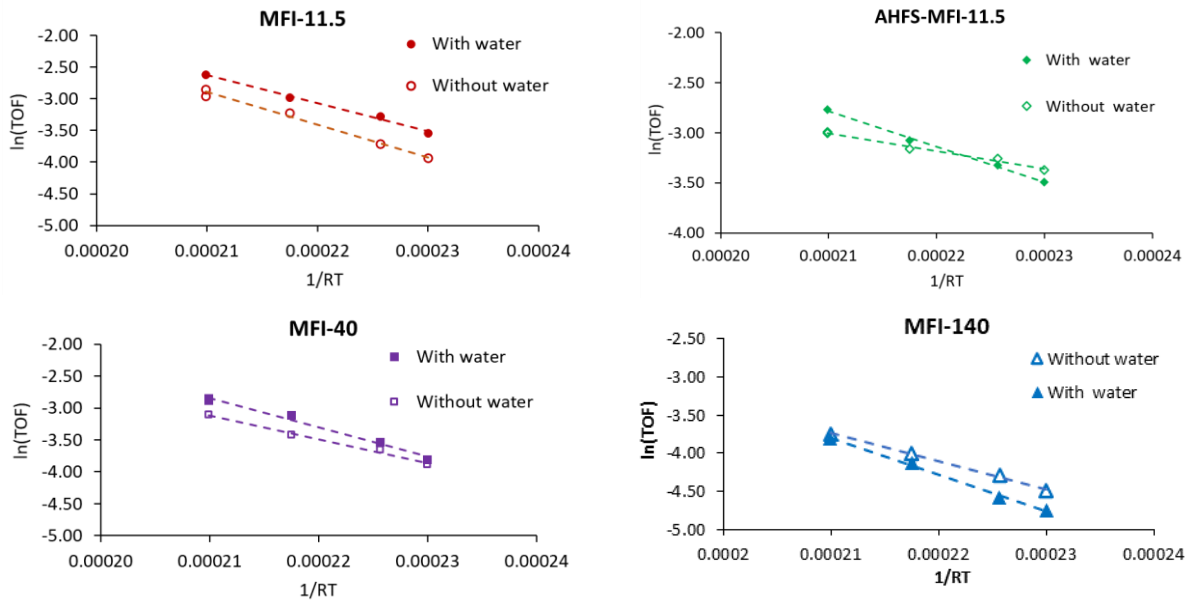

Fig. 18. Arrhenius plots for cumene dealkylation over different zeolites with and without water co-feeding, P_{cumene} = 0.5 kPa, P_{water} = 0 – 3.5 kPa

Based on the Arrhenius plots and transition state theory as derived in Appendix A3 - Section S1, the apparent activation energy, enthalpy, and entropy are summarized in Table 4. By comparing MFI-40 and MFI-140, where most Brønsted acid sites have been reported to reside in

the large pore intersections with the same confinement [21], the apparent activation enthalpy of reactions over these two catalysts are similar. In contrast, the apparent activation entropy of reaction over MFI-40 in the presence of paired sites is less negative than that over MFI-140 with isolated sites. It is acknowledged that the activation entropy calculated from the transition state theory is strongly influenced by the number of active sites. As cumene dealkylation rate over paired sites is significantly higher than the rate over isolated sites and there is a considerable fraction of aluminum in pairs in MFI-40, apparent activation entropy and enthalpy over two types of sites, paired sites versus isolated sites, in MFI-40 are decoupled by applying Equation 8 at different reaction temperatures for MFI-140 and MFI-40 with the known fraction of aluminum in pairs and combining with the transition state theory. As shown in Table 4, the apparent activation entropy on the paired sites in MFI-40 is less negative than that on the isolated sites. Therefore, the higher turnover frequency over MFI-40 when compared to MFI-140 is attributed to the entropic gain of the transition state due to proximate Brønsted acid sites interacting with the same transition state rather than an enthalpic stabilization for this reaction. It is speculated that the adjacent proton can exert a repulsive force on the positively charged transition state, leading to a higher activation entropy.

Table 4. Apparent activation energy, apparent activation enthalpy, and apparent activation entropy of cumene dealkylation on different zeolites with and without water co-feeding

Catalysts	Apparent activation enthalpy $\Delta H_{app}^{\ddagger}$, kJ/mol [a]	Apparent activation entropy $\Delta S_{app}^{\ddagger}$, J/mol.K [a]
MFI-11.5	47.1	-234
MFI-11.5 + H_2O	39.8	-247

AHFS-MFI-11.5	13.2	-304
AHFS-MFI-11.5 + H_2O	30.9	-271
MFI-40	32.8	-271
MFI-40 + H_2O	41.3	-246
MFI-140	31.9	-277
MFI-140 + H_2O	43.2	-258
Isolated sites in MFI-40	31.5	-280
Paired sites in MFI-40	33.3	-263

[a] calculated from transition state theory

In addition, the similar apparent activation enthalpy and increased apparent activation entropy for the paired sites when compared with the isolated sites could also suggest a looser and late transition state over the paired sites. This result is in line with the study of propylene oligomerization and alkanes cracking over ZSM-5 and CHA zeolites, where similar apparent activation enthalpy but less negative apparent activation entropy was reported on proximate sites compared to that on isolated sites [26, 29, 30]. On the other hand, the apparent activation enthalpy for AHFS-MFI-11.5 with the presence of paired sites and an insignificant amount of extra-framework aluminum species is lower than those for MFI-40 and MFI-140. This result can be explained by the fact that some Brønsted acid sites are located at more confined pore channels with a more enthalpic stabilization effect as the Si/Al decreases.

The mechanism of the alkylation of benzene with propylene, which is the reverse reaction of cumene dealkylation, over Brønsted acid sites was proposed to proceed through the C-C bond formation between benzene and surface propoxy species [94-96]. Weckhuysen and co-workers have applied spectrometry techniques to confirm the presence of surface ethoxy species and

carbocationic arenium ion/σ-complexes (i.e., Wheland-type reaction intermediates) in the ethylation of benzene over zeolites [97]. Based on these studies of aromatic alkylation and the moderate activation enthalpy (Table 4), a putative transition state for cumene dealkylation over H-ZSM-5 zeolites with a backside attack by an oxygen atom at the central isopropyl carbon was proposed in Scheme 2.

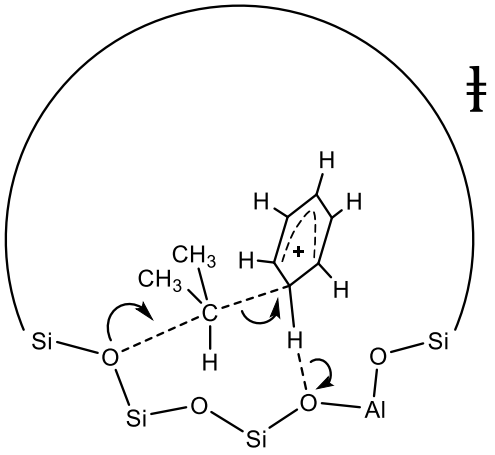

Scheme 2. Proposed transition state of cumene dealkylation over H-ZSM-5 zeolites

Interestingly, the effect of water co-feeding is consistent for reactions over MFI-140, MFI-40, and AHFS-MFI-11.5 with the negligible presence of extra-framework aluminum species. It is shown in Table 4 that the presence of water in reactions over these catalysts increases the apparent activation enthalpy, which is compensated for by less negative apparent activation entropy. It is well known that protons in Brønsted zeolites could become delocalized and form hydronium ion clusters $H_3O^+(H_2O)_n$ in the presence of water molecules inside zeolite pores [14, 15]. It is also worth mentioning that water molecules are unlikely to compete for adsorption sites with cumene since the heat of adsorption over H-ZSM-5 zeolites of water is about 51 kJ/mol, which is much lower than that of ethylbenzene (110 kJ/mol) [98, 99]. In fact, ab initio molecular dynamics (AIMD) simulations proved the formation of hydronium ion clusters in the presence of water and cyclohexanol, which is a highly competitive adsorbed reactant, in microporous BEA zeolite [100].

On the one hand, the enhancement in rate was observed upon water co-feeding for reaction over MFI-140, which has mainly isolated acid sites and is unlikely to benefit from the cooperative effect of site proximity in the presence of water. We speculate that the interaction of cumene with hydronium ion cluster instead of framework proton enables a looser reaction transition state with more degree of freedom, resulting in a less negative activation entropy. In fact, the entropic enhancement effect of water on cumene dealkylation becomes more pronounced at higher reaction temperatures (Fig. 18). Interestingly, this effect of water started to happen at a lower reaction temperature over MFI-40 compared to AHFS-MFI-11.5, followed by MFI-140. This result can be explained by the entropically beneficial effect of paired acid sites and acid site location at larger pore intersections in MFI-40. In contrast, it requires a higher temperature for the enhancement effect of water in reactions over other catalysts due to acid sites located at more confined pore channels in AHFS-MFI-11.5 and the lack of site proximity in MFI-140.

On the other hand, water molecules can also extend the interaction range of Brønsted acid sites in proximity by improving proton mobility through water-bridge networks, especially over zeolites with high Brønsted acid site density [17]. The delocalization of protons due to increased water should extend the distance by which neighboring framework acid sites may interact with the same transition state, resulting in more degrees of freedom and less negative entropy of this reaction transition state. This effect should be a function of the size of the delocalized hydronium cluster, which may be probed by altering the water partial pressure to examine the influence of local water concentration inside zeolite pores. Interestingly, after the incorporation of modest water amounts, the enhancement effect of water on cumene dealkylation becomes independent of the partial pressure of water, as shown in Fig. 19. It is known that the concentration of hydronium ions inside zeolite pores only depends on the Brønsted acid site density. The higher the partial

pressure of water, the more hydrated the hydronium ion clusters become. In addition, Li et al. found that the proton is only extended to about two water molecules from the original site in MCM-41-SO_3H catalysts, which implies that the positive charge in the hydronium cluster is close to the negative charge on catalyst surface [84]. Therefore, these results further suggest that the kinetic role of water in reactions over MFI-40 and AHFS-MFI-11.5 is related to the special distance between framework acid sites. In addition, it is noted that the maximum initial TOFs over AHFS-MFI-11.5 and MFI-40 are different, which we speculate is due to the varying fractions and location of paired sites in these catalysts.

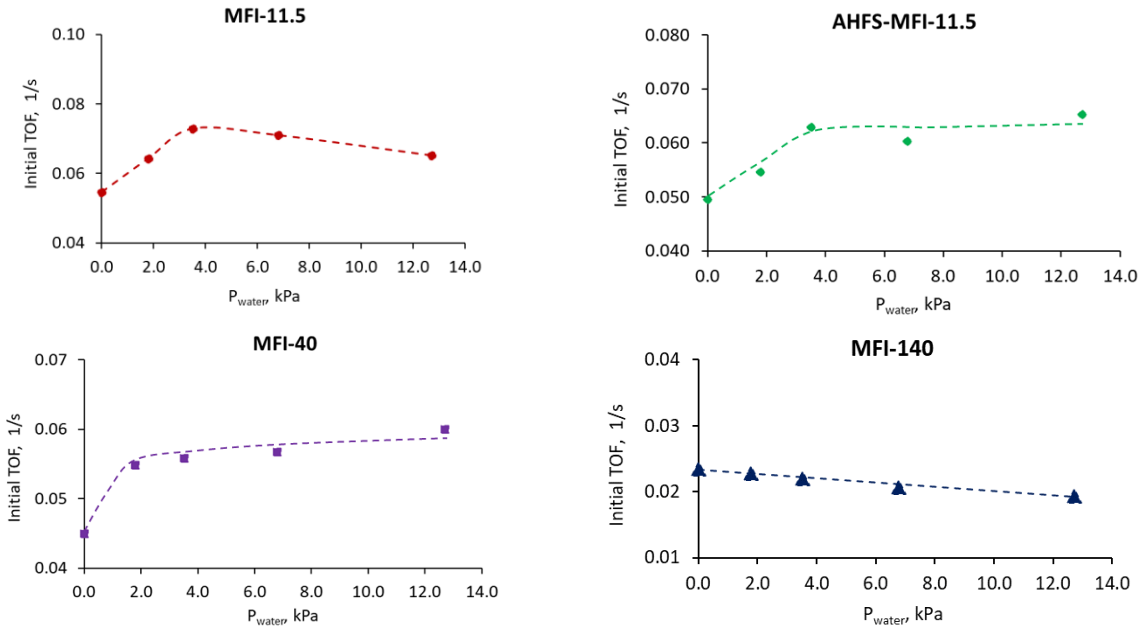

Fig. 19. Initial turnover frequency of cumene dealkylation with varying partial pressure of water co-feeding over H-ZSM-5 zeolites at reaction temperature of 300°C, P_{cumene} = 0.5 kPa. Dashed lines are to guide the eye.

Table 4 also shows a decrease in apparent activation enthalpy and more negative apparent activation entropy in the presence of water for reactions over MFI-11.5. This different behavior compared to AHFS-MFI-11.5 and MFI-40 is likely due to the significant amount of extra-

framework aluminum species present in MFI-11.5 and further revealed by the volcano curve where the initial TOF of cumene dealkylation was plotted with varying partial pressure of water (Fig. 19). Gounder et al. claimed that the presence of these extra-framework species leads to a tighter confinement inside zeolite pores [101]. In our case, the high partial pressure of water may lead to the formation of large clusters of hydrated extra-framework aluminum species, which act as spatial constraints inside MFI pores.

The role of extra-framework aluminum species in association with water in the low Si/Al zeolite MFI-11.5 was further clarified by the pulsing water experiment (Fig. 20). As reported previously, the pulsing water treatment does not create a persistent water partial pressure, nor does it lead to the loss of Brønsted acid sites or significant modifications in the crystallinity of H-ZSM-5 catalysts [82]. However, it is proposed that this treatment can facilitate the mobility of extra-framework aluminum species, leading to the formation of synergistic sites between Brønsted acid sites and neighboring extra-framework aluminum species. These synergistic sites are important for alkane cracking reactions, which happen at higher temperatures than cumene dealkylation and usually require high activation energy to protonate alkane molecules.

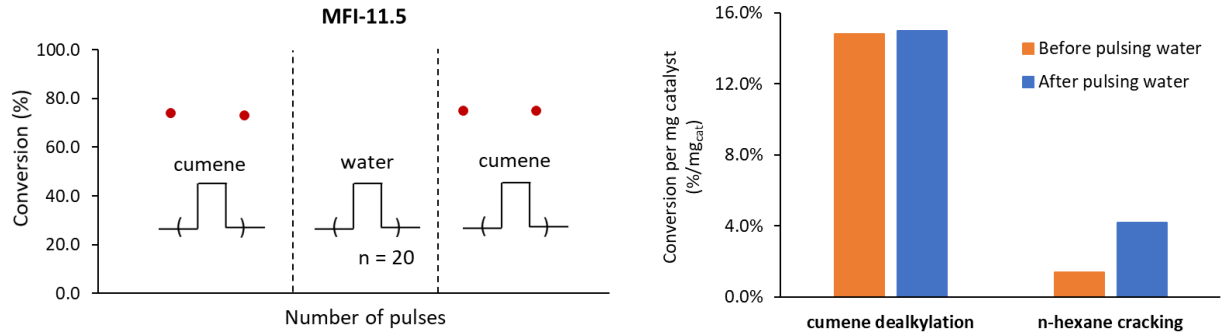

a) **b)**

Fig. 20. a) Conversion of cumene before and after pulsing water over 5 mg MFI-11.5 (T = 300°C); **b)** Compare conversion of cumene dealkylation (T = 300°C, P_{cumene} = 1.17 kPa) and n-hexane cracking (T = 480°C, $P_{n\text{-}hexane}$ = 4.5 kPa) [82] before and after pulsing water

The pulsing water treatment was conducted under the same conditions that significantly enhanced the reactivity of zeolites for the n-hexane cracking reaction. Interestingly, the results show that there is no difference in the rates of cumene conversion on the zeolite before and after pulsing water treatment, as shown in Fig. 20. Therefore, this observation implies that the synergistic EFAL-BAS sites are not responsible for the enhanced reaction rate of cumene dealkylation over H-ZSM-5 with high Brønsted acid site densities in the presence of water. While at high temperatures, water can modify the forms and the distribution of aluminum, this does not likely happen in the reaction conditions of cumene dealkylation. The different roles of water in the alkane cracking and cumene dealkylation are likely related to the difference in the mechanism of these reactions. This observation further suggests that the rate-limiting step of cumene dealkylation is less likely the protonation of adsorbed reactant, which usually requires the highest energy barrier in the case of alkane cracking. The co-presence of extra-framework aluminum species, paired sites, and water molecules inside MFI-11.5 pores create a more complicated system than AHFS-MFI-11.5 and MFI-40 catalysts where only framework site density and location are modified.

Catalyst deactivation in cumene dealkylation: effect of extra-framework aluminum species, reaction temperature, and the presence of water

The products of cumene dealkylation are propylene and benzene, with an expected molar ratio of 1:1. However, propylene is a reactive olefin that can readily undergo subsequent reactions such as oligomerization over H-ZSM-5 zeolites and form coke even at low temperatures [102]. The selectivity toward propylene is slightly lower than benzene for reactions over different zeolites (Fig. 21). This observation suggests that propylene may continue to oligomerize and form heavier compounds in zeolites which is the main cause of catalyst deactivation over time on stream.

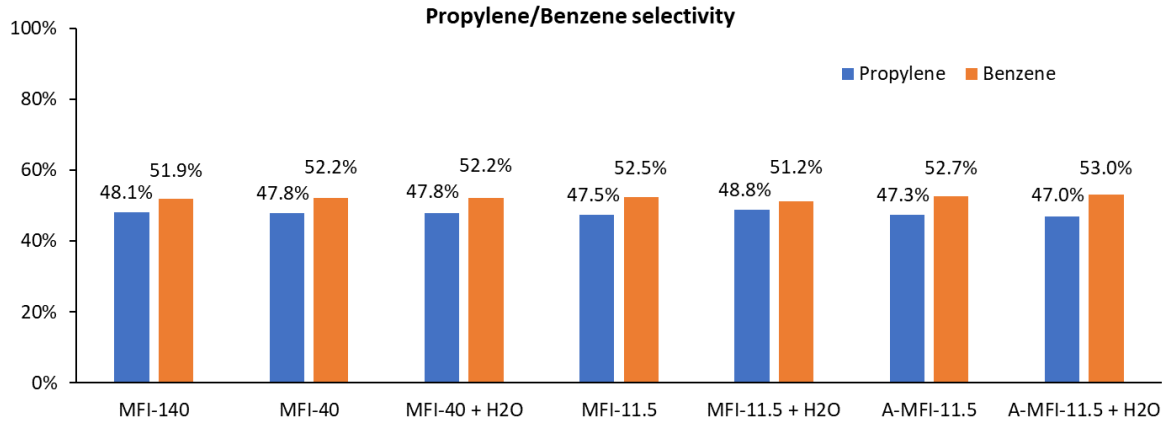

Fig. 21. Product selectivity of cumene dealkylation over different zeolites with and without water co-feeding at 300°C, TOS = 30 min, P_{cumene} = 0.5 kPa, P_{water} = 0 – 3.5 kPa

Catalyst deactivation during cumene dealkylation was evaluated by plotting the turnover number – turnover frequency correlation as previously described [89]. The influence of Brønsted acid site density and the role of extra-framework aluminum species on catalyst stability in cumene dealkylation were evaluated, as shown in Fig. 22.

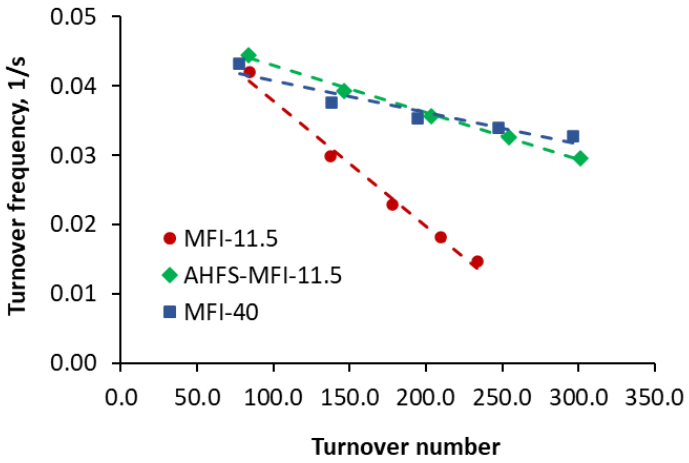

Fig. 22. Deactivation plots of different zeolites in cumene dealkylation at reaction temperature of 300°C, P_{cumene} = 0.5 kPa

Catalyst deactivation tends to increase with Brønsted acid site density by comparing TON-TOF plots of MFI-40 and AHFS-MFI-11.5. In fact, propylene oligomerization is a sequential reaction that should enhance with the increase of Brønsted acid site density or the presence of adjacent Brønsted acid sites. This result is in agreement with previous literature that found that the turnover frequency of propylene oligomerization over close Brønsted acid sites could be up to one order of magnitude higher than that over isolated Brønsted acid sites, which is attributed to the transition state entropy gain over proximate sites [29, 103].

In addition, it seems that the presence of extra-framework aluminum species in MFI-11.5 leads to a faster catalyst deactivation compared to AHFS-MFI-11.5, which has a similar Brønsted acid site density but with an insignificant amount of extra-framework aluminum species. It has been reported that these extra-framework aluminum species increase the adsorption enthalpy of adsorbed molecules [58]. Consequently, coke precursors generated from propylene oligomerization may adsorb more strongly to the acid sites and further undergo coke formation. Additional extra-lattice species may also impede the diffusion paths of exiting products. In fact, it was reported by many research groups that the presence of extra-framework aluminum species in zeolites correlates with increased catalyst deactivation rates in various reactions such as n-heptane cracking, toluene disproportionation, toluene alkylation with ethylene, n-butene isomerization, and cumene–toluene transalkylation [104-107].

The presence of water not only facilitates cumene dealkylation by increasing transition state entropy but also reduces catalyst deactivation over reaction time on stream, as shown in Fig. 23-26. This effect of water on catalyst stability is consistent for catalysts with different Brønsted acid site densities and with the presence or absence of extra-framework aluminum species.

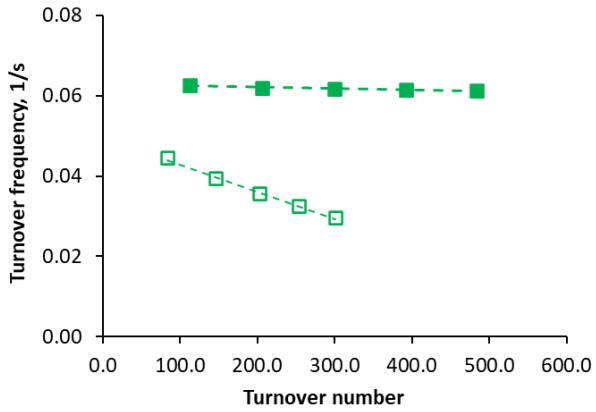

Fig. 23. Effect of water co-feeding on deactivation of AHFS-MFI-11.5 at reaction temperature of 300°C, P_{cumene} = 0.5 kPa, P_{water} = 0 kPa (□); P_{cumene} = 0.5 kPa, P_{water} = 3.5 kPa (■)

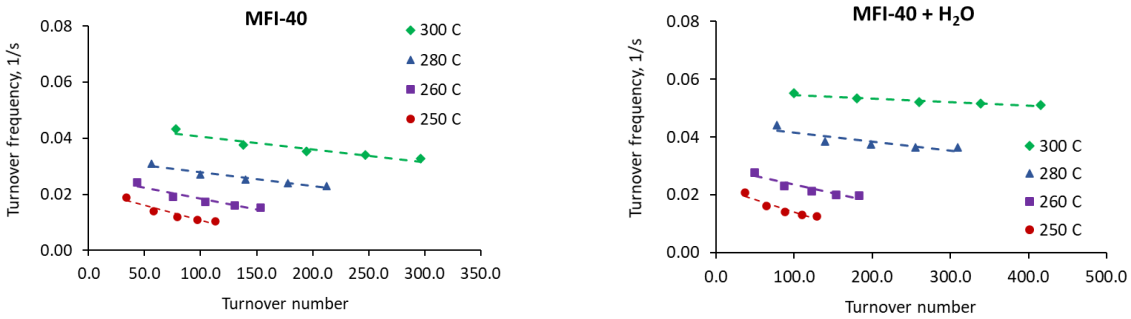

Fig. 24. Effect of reaction temperature on deactivation of H-ZSM-5 (Si/Al = 40) in the absence and presence of water, P_{cumene} = 0.5 kPa, P_{water} = 0 – 3.5 kPa

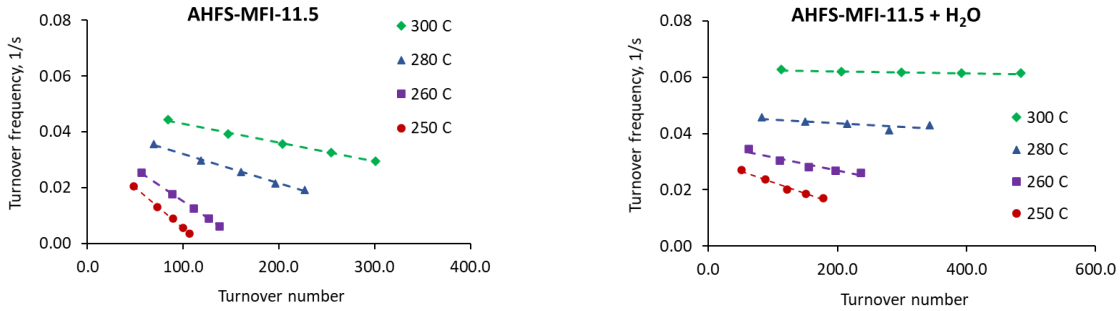

Fig. 25. Effect of reaction temperature on deactivation of AHFS-MFI-11.5 in the absence and presence of water, P_{cumene} = 0.5 kPa, P_{water} = 0 – 3.5 kPa

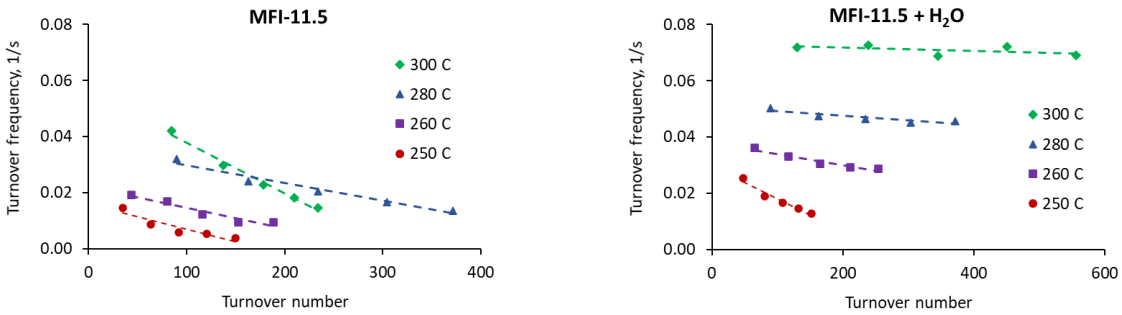

Fig. 26. Effect of reaction temperature on deactivation of MFI-11.5 in the absence and presence of water, P_{cumene} = 0.5 kPa, P_{water} = 0 – 3.5 kPa

It is acknowledged that Brønsted acid sites are delocalized to form hydronium ion clusters inside zeolite pores that can still catalyze reactions such as alcohol dehydration [85, 86]. Therefore, these hydronium ion clusters should be able to catalyze a facile reaction such as propylene oligomerization. On the other hand, the heat of water adsorption on H-ZSM-5 zeolites is about 51 kJ/mol measured experimentally [98], while propylene adsorption on H-ZSM-5 forms a stable carbenium ion [108]. Another light olefin, such as ethylene, has a heat of adsorption of 46 kJ/mol on H-ZSM-5 zeolite based on hybrid MP2:DFT calculation [99]. Therefore, water is less likely to enhance catalyst stability by competing for adsorption sites with propylene molecules and inhibiting propylene oligomerization. In fact, the selectivity towards propylene is almost unchanged in the absence and presence of water for AHFS-MFI-11.5 and MFI-40 zeolites (Fig. 21). This observation implies that water does not stop propylene from further reactions by competitive adsorption.

It has been discussed that water molecules inside zeolite pores tend to delocalize the proton and improve Brønsted acid site proximity. On the other hand, Bell and co-workers found that the presence of oligomers on the adjacent Brønsted acid site increases activation energy for propylene trimerization, whereas the acid site proximity does not affect propylene dimerization, resulting in

a higher selectivity to dimers [27]. As a result, the accumulation of heavy compounds and coke from propylene oligomerization is reduced, which leads to a more stable catalyst. Therefore, the enhancement of catalyst stability in the presence of water can be attributed to the effect of water molecules on facilitating Brønsted acid site proximity. However, we note in this case that propylene dimers are not observed in significant quantities as one might expect if this were the case. Alternatively, we hypothesize that water may promote a more stable intermediate where the framework-bound proton is shared between a water molecule and the olefin, lowering the energy of the intermediate but leading to a higher intrinsic activation energy for coupling. This stabilization effect of water has been shown in alcohol dehydration, where water enthalpically stabilizes adsorbed intermediate to a greater extent than the relevant transition state, leading to a higher energy barrier for propene formation [109, 110]. The root cause of enhancing catalyst stability during cumene dealkylation in the presence of water requires further study.

Conclusion

Cumene dealkylation rates are significantly enhanced by the presence of Brønsted acid sites in close proximity. Interestingly, the reaction rate also increases with the presence of water molecules with a reversible effect. Based on detailed reaction kinetics, it is evident that the presence of paired sites or water improves the turnover frequency in reactions over H-ZSM-5 zeolites by the entropic gain of the transition state within the first-order reaction regime. We propose that the formation of hydrated hydronium ions in the presence of water may create a looser transition state with more degree of freedom as well as extend the network of proximate protons that may interact with the same transition state by improving proton mobility through water-bridge networks. It is also worth mentioning that the EFAL-BAS synergistic sites generated by pulsing water over H-ZSM-5 with a low Si/Al ratio do not influence the conversion of cumene dealkylation

under the reaction conditions. However, the presence of extra-framework species in H-ZSM-5 zeolites may reduce catalyst stability against coking. The deactivation mechanism is attributed to the subsequent oligomerization of propylene. Catalyst stability during cumene dealkylation can be improved by adding moisture, removing extra-framework aluminum species, and optimizing reaction temperature. These findings are of great practical importance to modifying rates of parallel reactions in recycling mixed polymer blends and enabling the production of high-value chemicals with a more robust catalytic reaction system.

Acknowledgement

The authors are grateful for the support from the National Science Foundation under the Grant No. CHE-1764130 to carry out this research. We thank Dr. Daniel E. Resasco for helpful technical discussions.

Chapter 4: The role of water on zeolite-catalyzed transformation of polar polymers

All the data presented in this chapter is obtained at the University of Oklahoma. The DFT calculations and discussion as a part of this work were performed by Quy Nguyen and Dr. Bin Wang. This chapter will be submitted as a journal article using the citation: Han K. Chau, Quy P. Nguyen, Lance L. Lobban, Bin Wang, Steven P. Crossley, "The role of water on zeolite-catalyzed transformation of polar polymers".

Abstract

Selective dehydration of polyalcohols over zeolites containing Brønsted acids is a promising approach to purify and recycle multilayer polymer films consisting of non-polar polymers such as polyethylene and polar polymers like ethylene-vinyl alcohol copolymer. In addition, polar aprotic solvents can be utilized to improve the diffusion of polymer molecules to access the active sites in solid catalysts. Here, we reveal the positive role of water on dehydration of ethylene-vinyl alcohol polymer over a solid acid catalyst in the presence of γ-valerolactone as the solvent. Through vapor phase experiments with 2,5-hexanediol as a model compound and theoretical calculations, we reveal that water facilitates dehydration reactions by delocalizing surface bound protons and allowing dehydration rates to occur even in the presence of solvents that would otherwise inhibit reaction rates through competitive adsorption on the surface. The hydronium ion clusters act as delocalized acid sites, leading to improved surface coverage of the reactant, and consequently enhance dehydration activity in the presence of solvent molecules. This example of co-solvent induced modulation of competitive adsorption for active sites could open new doors for polymer recycling and upcycling.

Introduction

Plastics play a vital part in modern life due to their outstanding durability, versatility, lightweight nature, and cost-efficiency. Recently, multilayer packaging materials have been advancing rapidly and emerging as a desirable choice for protecting perishable foods and medicine due to their excellent moisture resistance and oxygen barrier properties with less material and energy required for production than single-resin plastic alternatives [111]. The sharp increase in the consumption of these plastic products creates significant challenges in plastic recycling, yet it provides opportunities for developing feasible catalytic systems for the recycling of plastic waste [112]. At present, most plastic waste ends up in landfills, thus losing the intrinsic value of the material while creating environmental concerns. In recent years, besides conventional mechanical methods, many chemical processes and catalytic systems such as pyrolysis, hydrogenolysis, and solvolysis have been proposed to recycle plastic waste and convert them into high-value products, which foster a circular economy for plastics [113-120]. Recycling of mixed polymers or multilayer films is even more challenging due to the presence of different non-polar polymers such as polyethylene (PE) and polypropylene (PP) and polar polymers like ethylene-vinyl alcohol copolymer (EVOH) [121, 122]. The ability to selectively target specific polymers in these multicomponent mixtures would enable vastly improved recycling. A staged conversion would allow for purification and re-use, or alternatively better optimized post-processing approaches to yield higher-value products such as olefin monomers, fuels, and lubricants. Huber and co-workers have proposed a non-catalytic dissolution and precipitation approach for the recycling of multilayer plastic films, which requires the considerable usage of multiple different polar and non-polar solvents [123, 124]. The approach proposed here illustrates a similar concept, but with a prior catalytic treatment rather than solvent treatment alone.

Here we carry out the dehydration of 2,5-hexanediol (the model compound) and real EVOH polymers over Brønsted-acid zeolites in the presence of a polar aprotic solvent. A unique feature of this approach is that the polar polymer can be converted to a non-polar polymer, which is more compatible with the other polyolefins and allows a more efficient recycling of the multilayer polymer films, without breaking the C-C bonds of the polymer backbone. Gamma-valerolactone (GVL), a sustainable green solvent derived from lignocellulosic biomass [125], was used to improve the accessibility of polymer molecules to the active sites on solid catalysts with a lower temperature requirement compared to molten phase reactions. We report the reduced dehydration rate due to the competitive adsorption of the polar aprotic solvent, which can be alleviated by co-feeding water. Kinetics and mechanistic investigations suggest that in the presence of water, hydronium ion clusters are more favorable to reactant adsorption than are the framework Brønsted acid sites.

Results

Effect of polar aprotic solvent and co-feeding water on dehydration of model compound

Alcohol dehydration over solid acid catalysts such as zeolites has been studied extensively for decades, especially in the biomass upgrading process [110, 126, 127]. Since zeolites contain both Brønsted and Lewis acid sites, it is still debatable which one is the active site in alcohol dehydration reactions. However, it is generally accepted that the alcohol dehydration rate correlates well with the Brønsted acid site density in zeolite catalysts [109]. Water is the by-product of alcohol dehydration reactions. The presence of water in the dehydration of alkanols (e.g., ethanol, propanol, and butanol) often shows the negative effect as it inhibits the formation of olefins by stabilizing adsorbed intermediates and forming stable dimer [109, 110, 128]. However,

it is unclear what influence water will have during the dehydration of EVOH polar polymers in the presence of polar aprotic solvent.

In commercial products, EVOH normally contains about 30 mol% ethylene and 70 mol% vinyl alcohol to maximize the oxygen barrier properties. Therefore, 2,5-hexanediol was selected as the model compound of EVOH to investigate the influence of solvent on dehydration mechanisms. This di-alcohol compound has a molar ratio of ethylene to vinyl alcohol similar to that of EVOH, and the hydroxyl groups are also located at the secondary carbons like EVOH copolymer.

While the dehydration of diol compounds such as hexanediol over zeolite catalysts has not been adequately addressed in the literature, it is known that hexanediol can undergo a ring-closing reaction to form a cyclic ether, which can then form di-olefins by a dehydra-decyclization mechanism. The ring-opening and subsequent dehydration of cyclic ethers such as dimethyl tetrahydrofuran has been extensively studied over solid acid catalysts [129-133].

The gas phase dehydration of 2,5-hexanediol with co-feeding GVL over MFI-140 was carried out at 250°C and atmospheric pressure (Fig. 27). The observable products were 2,5-dimethyltetrahydrofuran, hexadienes, and hydride transfer (HT) products (e.g. hexenes). In addition, pentenoic acid (PA) isomers were observed as the products of GVL ring-opening over Brønsted acid sites in MFI-140, which is consistent with the literature [134]. The reaction pathway of 2,5-hexanediol dehydration to form hexadienes over isolated Brønsted acid sites in MFI-140 via a cyclic ether intermediate is shown in Fig. 27a, which was identified by varying reaction space time W/F. It should be noted that the conversion of 2,5-hexanediol was 100% during reaction time on stream in these experiments. As shown in Fig. 27b, the product yield of DMTHF decreases from 74.0 mol% to 62.9% with increasing W/F from 0.32 h to 1.24 h, which suggests that the

cyclic ether is the primary product of 2,5-hexanediol dehydration. On the other hand, the yield of hexadienes increases from 25.2 mol% to 35.2 mol% and the yield of hydride transfer products from 0.8 mol% to 1.8 mol% when the reaction space time increases from 0.32 h to 1.24 h, which indicates that these compounds are secondary products.

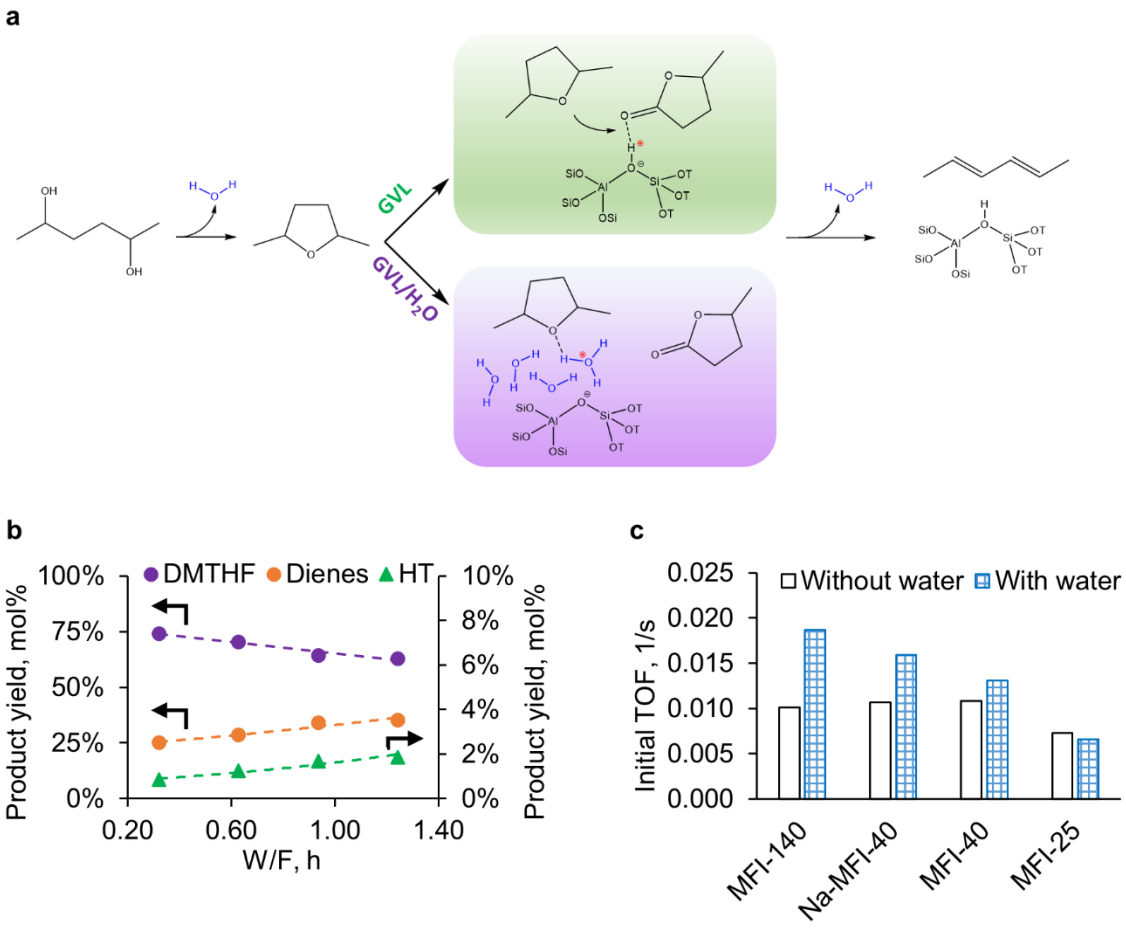

Fig. 27. Dehydration of 2,5-hexanediol model compound. **a,** Schematic reaction pathway of 2,5-hexanediol dehydration over Brønsted zeolites. **b,** Product yields of 2,5-hexanediol dehydration over MFI-140 with varying reaction space time. Reaction conditions: T = 250°C, $P_{2,5\text{-hexanediol}}$ = 0.09 kPa, P_{GVL} = 0.6 kPa. **c,** Initial turnover frequency of hexadienes formation in 2,5-hexanediol

dehydration over different H-ZSM-5 zeolites in the absence and presence of water. Reaction conditions: T = 250°C, $P_{2,5\text{-hexanediol}}$ = 0.09 kPa, P_{GVL} = 0.6 kPa, P_{water} = 0 kPa or 3.5 kPa.

The evidence for this reaction pathway is shown in Fig. 28 where product yields were plotted as a function of reaction time on stream over both MFI-140 and MFI-40. Over both catalysts, as the catalyst deactivated during reaction time on stream, the yield of DMTHF increases while the yield of hexadienes decreases. The significantly higher yield of DMTHF compared to hexadienes suggests that the formation of cyclic ether intermediate is facile while the formation of hexadienes is the slower step. Dumesic and co-workers also found that the ring-opening of DMTHF over SiO_2/Al_2O_3 catalyst proceeds via carbocation mechanism and resulted in a high yield of hexadiene isomers [133].

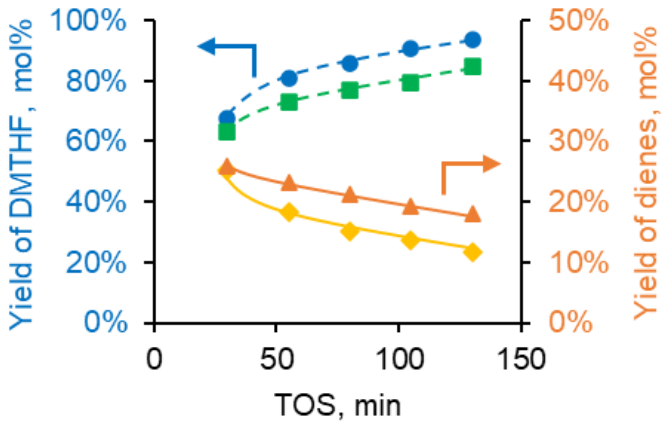

Fig. 28. Product yields of 2,5-hexanediol dehydration over MFI-140 during reaction time on stream. Reaction conditions: T = 250°C, $P_{2,5\text{-hexanediol}}$ = 0.09 kPa, P_{GVL} = 0.6 kPa

Because of the significant deactivation that takes place, initial turnover frequencies were used to decouple kinetic effects from catalyst deactivation. Fig. 29 shows the best fits for the formation of hexadienes over three different MFI zeolites assuming exponential activity loss, i.e., activity given by $TOF = TOF_0 \cdot e^{-\beta t}$. The effect of water on dehydration of 2,5-hexanediol was studied by co-feeding water at a constant partial pressure over different Brønsted zeolites as shown

in Fig. 27c, which compares initial TOF in the absence and in the presence of water. The equivalent initial turnover frequency of hexadienes formation over MFI-140, Na-MFI-40, and MFI-40 in the absence of water are nearly equal. Since these catalysts have identical pore structure (and therefore identical internal mass transfer characteristics) but different active site densities (given in Table 5), this result suggests that the reactions over these catalysts are not limited by internal diffusion.

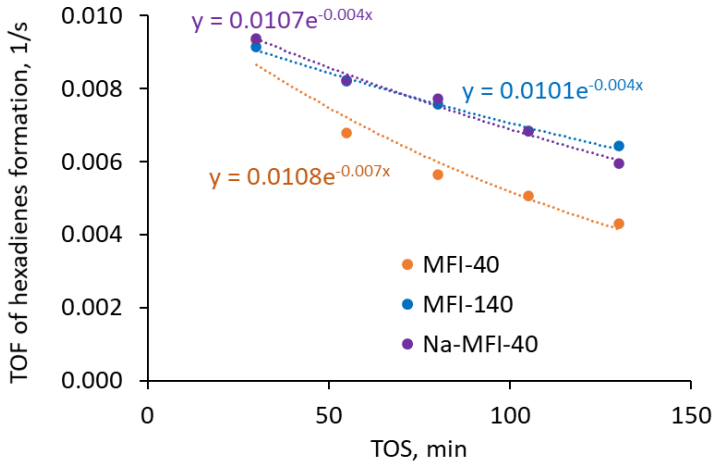

Fig. 29. Turnover frequency of hexadienes formation over different MFI zeolites. Reaction conditions: T = 250°C, $P_{2,5\text{-hexanediol}}$ = 0.09 kPa, P_{GVL} = 0.6 kPa

On the other hand, the initial turnover frequency over MFI-25, which has the highest acid site density, is lower than other MFI catalysts, which implies that the reaction over MFI-25 is likely to be diffusion-limited. Fig. 27c shows that in the presence of GVL, the addition of water actually facilitates the dehydration of 2,5-hexanediol to form hexadienes over MFI catalysts operating under a surface-reaction-controlled regime.

Table 5. Brønsted acid site densities of zeolites used in dehydration reactions

Catalysts	Si/Al ratio	Brønsted acid site densitiy, mmol/g		Extra-framework aluminum species, mmol/g [c]
		Calculated [a]	IPA-TPD method	
MFI-25	25	0.644	0.502	0.142

MFI-40	40	0.417	0.391	0.026
Na-MFI-40	40	-	0.153	-
MFI-140	140	0.119	0.106	0.013
BEA-133	133 [b]	0.124	0.119	0.005

[a] Theoretical values based on framework Si/Al ratio

[b] Determined by ICP-OES method (Galbraith Laboratories)

[c] Extra-framework aluminum species is calculated as the difference between the theoretical BAS density and the measured BAS density

A similar effect of water was observed for reaction over high silica Beta zeolite BEA-133 (Fig. 30). Interestingly, the effect of water is most pronounced on high-silica H-ZSM-5 zeolite with the lowest acid site density (MFI-140), with the initial turnover frequency of hexadienes formation increasing 85% with co-feeding water. The cause of this increase may be the formation of water molecule clusters and is discussed later in this paper.

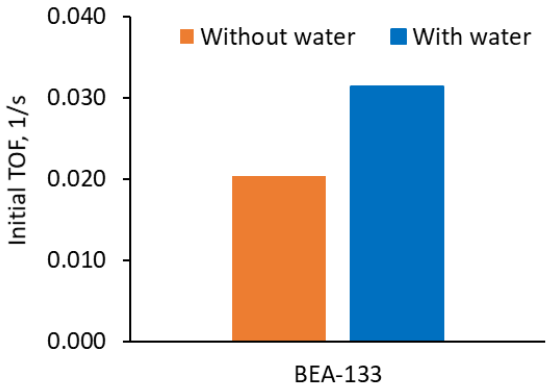

Fig. 30. Initial turnover frequency of hexadienes formation over BEA-133 zeolite in the absence and presence of water. T = 250°C, $P_{hexanediol}$ = 0.09 kPa, P_{GVL} = 0.6 kPa, P_{water} = 0 kPa (■), P_{water} = 3.5 kPa (■)

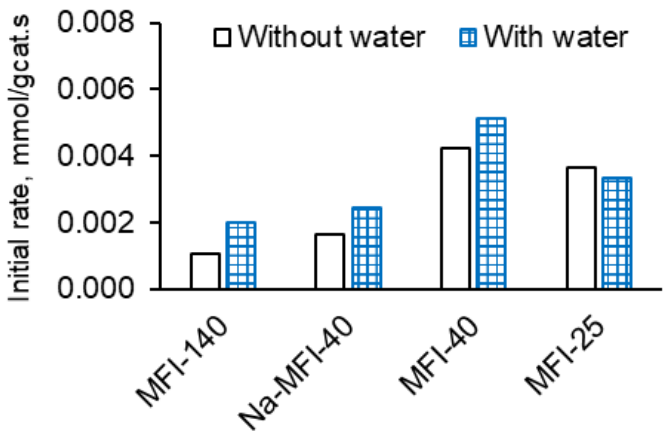

Fig. 31. Hexadienes formation rate per gram catalyst over different MFI zeolites in the absence and presence of water. T = 250°C, $P_{hexanediol}$ = 0.09 kPa, P_{GVL} = 0.6 kPa, P_{water} = 0 kPa or 3.5 kPa

The rate per gram of catalyst also increases with the addition of water on the three lowest acid site density catalysts (Fig. 31), but over the high site density MFI-25, the measured rate per gram of catalyst is lower in the presence of water. This decrease could be attributed to the increase of diffusional constraints caused by the presence of the water molecule clusters. It is noted that the Brønsted acid sites in these high Si/Al zeolites are mainly isolated sites, while the fraction of aluminum in pairs in MFI-40 is about 0.322 based on the Co^{2+} exchange method [91]. Two aluminum atoms separated by two silicon atoms ($AlSi_2Al$ sequence) in zeolites are often considered an aluminum pair [3]. These adjacent sites in zeolite catalysts significantly influence many acid-catalyzed reactions [26-28]. Gounder and co-workers investigated the role of acid site proximity in alkane cracking over chabazite zeolites and found that sodium exchange favorably titrates paired Brønsted acid sites over isolated Brønsted acid sites in CHA frameworks [30]. In our study, the enhancement of the initial rate in the presence of co-fed water over sodium-titrated catalyst Na-MFI-40 (49%) is more significant compared to parent zeolite MFI-40 (21%) as shown in Fig. 27c. In addition, the location of Brønsted acid sites in high-silica MFI zeolites (Si/Al > 23) is mainly at the channel intersections [21]. Therefore, the less notable effect of water on higher

acid site density MFI zeolites such as MFI-40 is less likely due to different acid site locations but could be attributed to the acid site distribution or role of site proximity in these catalysts.

It is worth mentioning that the catalysts in this study have low Brønsted acid site density with an insignificant amount of extra-framework aluminum species (Fig. 32a and Table 5). In addition, the reaction temperature in this study is 250°C which is lower than the reported value (450°C) for dealumination of ZSM-5 zeolites in the presence of water vapor [93]. Therefore, the effect of water here should not be related to the change of zeolite structure under the reaction conditions.

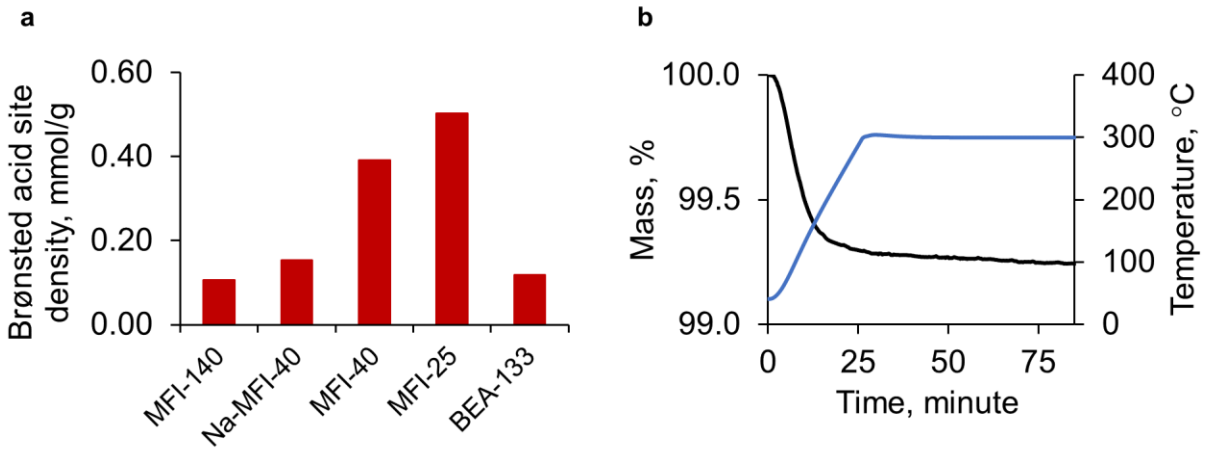

Fig. 32. Catalyst characterization. **a,** Brønsted acid site density of different zeolites measured by temperature program reaction of isopropyl amine. **b,** Mass loss of MFI-140 sample after being exposed to water (P_{water} = 3.5 kPa, T = 250°C, 1 hour) from thermogravimetric analysis (TGA)

On the other hand, the presence of two or more water molecules inside zeolite pores was found to facilitate the delocalization of proton from the zeolite framework and form hydronium ion clusters even at room temperature [14, 16]. As shown in Fig. 32b, the weight loss of hydrated MFI-140 sample in TGA after being exposed to water under reaction conditions is about 0.76 wt.%, leading to the calculated number of four water molecules per Brønsted acid site in MFI-140

catalyst. As a result, the accessibility of the reactant to the hydronium ion clusters or mobile acid sites in the presence of competitive molecules such as GVL can be improved, leading to higher surface coverage and reaction rate.

The influence of partial pressure of water on hexadienes formation over MFI-140 and MFI-40 is shown in Fig. 33. It shows that the effect of water on the turnover frequency of hexadienes formation slightly decreases with doubling the partial pressure of water. This observation suggests that adding a small amount of water (P_{water} = 3.5 kPa) improves the formation of hexadienes, but the higher partial pressure of co-fed water could lower the accessibility of the reactant molecules to the mobile active sites as hydronium ion clusters become larger.

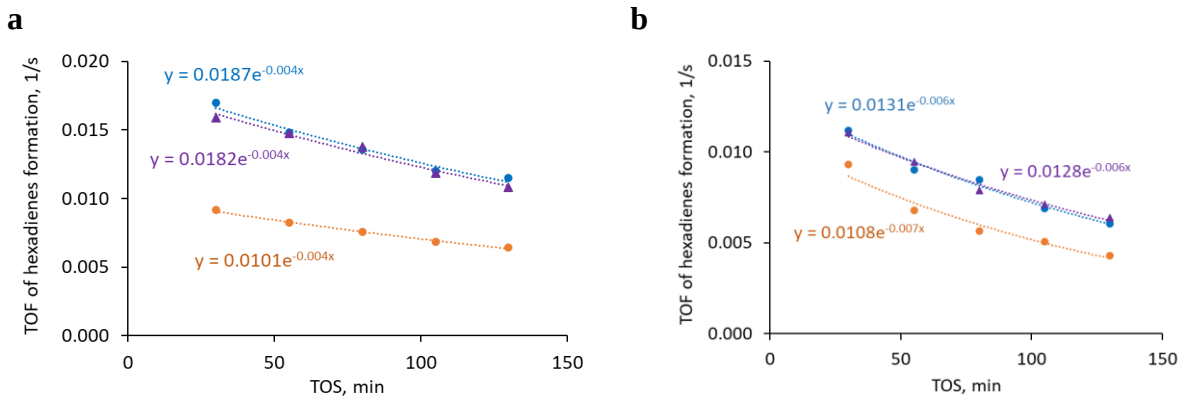

Fig. 33. Turnover frequency of hexadienes formation over. **a,** MFI-140 and **b,** MFI-40. Reaction conditions: T = 250°C, $P_{hexanediol}$ = 0.09 kPa, P_{GVL} = 0.6 kPa, P_{water} = 0 kPa (●), P_{water} = 3.5 kPa (●), P_{water} = 7.0 kPa (▲)

The presence of water is also known to intervene in the ring-opening of GVL over solid acid catalyst [135, 136]. Haider et al. found that oxocarbenium ion is stabilized by water, which enables the two-step reaction pathway of GVL ring-opening with lower activation energy [136]. In fact, the formation of pentenoic acid isomers from GVL ring-opening is enhanced by co-feeding water (Fig. 34). Pentenoic acid isomers were found to have a higher heat of adsorption than GVL

[135]. Therefore, it is expected that these GVL ring-opening products also inhibit the dehydration of intermediate cyclic ether, as is shown in Fig. 35.

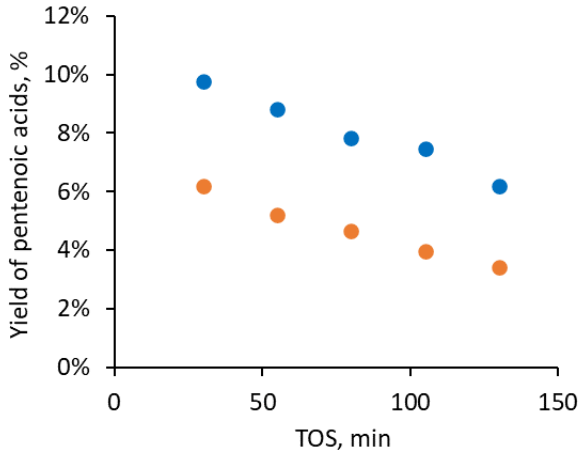

Fig. 34. Yield of pentenoic acids formation from GVL over MFI-140 during 2,5-hexanediol dehydration in the presence of GVL. Reaction conditions: T = 250°C, $P_{hexanediol}$ = 0.09 kPa, P_{GVL} = 0.6 kPa, P_{water} = 0 kPa (●), P_{water} = 3.5 kPa (●)

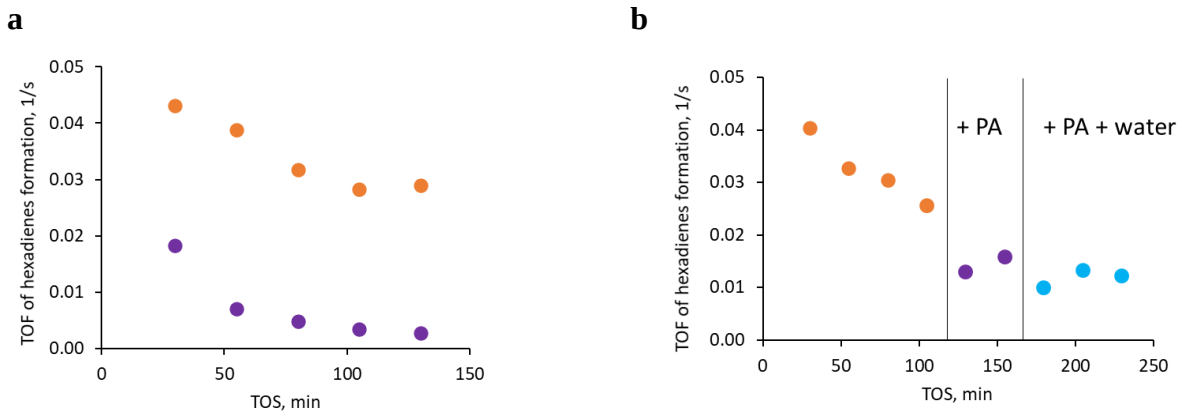

Fig. 35. Turnover frequency of hexadienes formation over MFI-140. **a,** in two separated experiments. **b,** in one experiment with intermittent co-feeding. Reaction conditions: T = 250°C, P_{DMTHF} = 0.08 kPa; $P_{4\text{-pentenoic acid}}$ = 0 kPa, P_{water} = 0 kPa (●); $P_{4\text{-pentenoic acid}}$ = 0.16 kPa, P_{water} = 0 kPa (●); $P_{4\text{-pentenoic acid}}$ = 0.16 kPa, P_{water} = 3.5 kPa (●)

Based on these observations, it is important to decouple the role of GVL and water on the dehydration of 2,5-hexanediol over MFI-140. The dehydration pathway of 2,5-hexanediol was found to proceed via intermediate cyclic ether as aforementioned. The kinetic effect of water on alcohol dehydration, the first step in the reaction pathway over solid acid catalysts, has been studied extensively in literature. Marin et al. found that water does not influence 1-butanol dehydration over ZSM-5 zeolites [137]. On the other hand, a negative effect of water on dehydration rate was observed by Iglesia et al. and Lercher et al., which was explained by the stabilization of adsorption state of alcohol in the presence of water [109, 110]. In our studies, this first step is facile and fast, and so the effects of water on the first step cannot be ascertained. However, the water clearly has an effect on the secondary reactions. Therefore, our subsequent studies focused on the effects of water and GVL on the conversion of 2,5-dimethyltetrahydrofuran, the primary product of the di-alcohol dehydration. Unless otherwise noted, these studies are all carried out over the MFI-140 catalysts, which shows the most pronounced effect of co-feeding water.

Results are shown in Fig. 36a and Fig. 36b for hexadiene formation TOF versus time on stream with DMTHF as the reactant. As was the case when hexanediol was the fed reactant, several observations can be made: the addition of GVL significantly inhibits the rate, co-feeding water in the absence of GVL has a minor effect, but co-feeding water in the presence of GVL enhances the rate over that occurring with only GVL co-fed. Deactivation does occur, so as before, the data is fit to a simple deactivation model to obtain initial TOF values to aid in subsequent analysis of reaction mechanism and kinetics. The dependence of hexadiene formation rate on DMTHF partial pressure was obtained by varying DMTHF partial pressure for several cases: no co-fed components

(Fig. 37); with co-fed water (Fig. 38); with co-fed GVL (Fig. 39); and with co-fed water and GVL (Fig. 40).

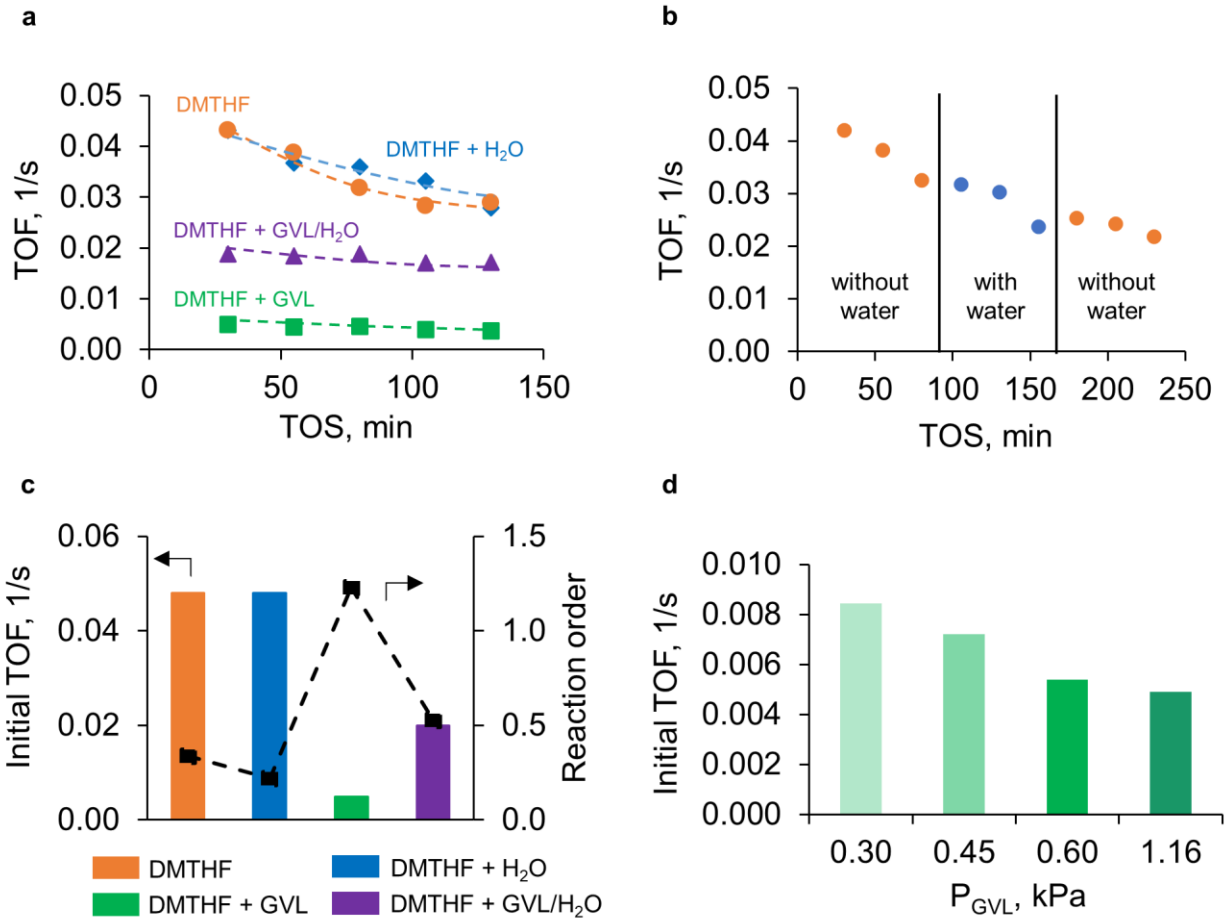

Fig. 36. Dehydration of intermediate ether 2,5-dimethyltetrahydrofuran. **a,** Turnover frequency of hexadienes formation over MFI-140 in the absence and presence of water. Reaction conditions: T = 250°C, P_{DMTHF} = 0.08 kPa; P_{GVL} = 0 kPa, P_{water} = 0 kPa (●); P_{GVL} = 0 kPa, P_{water} = 3.5 kPa (♦); P_{GVL} = 0.6 kPa, P_{water} = 3.5 kPa (▲); P_{GVL} = 0.6 kPa, P_{water} = 0 kPa (■). **b,** Turnover frequency of hexadienes formation over MFI-140 with intermittent co-feeding of water. T = 250°C, PDMTHF = 0.08 kPa, P_{water} = 0 kPa (●) or 3.5 kPa (●). **c,** Correlation between reaction rate and reaction order with respect to 2,5-dimethyltetrahydrofuran in different co-

feeding experiments over MFI-140. Reaction conditions: T = 250°C, P_{DMTHF} = 0.08 kPa; P_{GVL} = 0 kPa, P_{water} = 0 kPa (■); P_{GVL} = 0 kPa, P_{water} = 3.5 kPa (■); P_{GVL} = 0.6 kPa, P_{water} = 0 kPa (■); P_{GVL} = 0.6 kPa, P_{water} = 3.5 kPa (■). **d,** Inhibition effect of GVL on dehydration of 2,5-dimethyltetrahydrofuran over MFI-140. Reaction conditions: T = 250°C, P_{DMTHF} = 0.08 kPa; P_{GVL} = 0.30 – 1.16 kPa.

The resulting reaction orders are presented in Fig. 36c, along with the initial TOF for P_{DMTHF} = 0.08 kPa. The similar turnover frequency and reaction order of DMTHF with and without co-feeding water indicates that water may influence the adsorption state and transition state of the vapor-phase dehydration of DMTHF in the absence of GVL to the same extent which does not change the intrinsic energy barrier. On the other hand, adding GVL significantly reduces the dehydration of DMTHF. Furthermore, the presence of water mitigates the inhibition effect of GVL and improves the formation of hexadienes when the reaction is carried out in the presence of GVL. Therefore, this result on the intermediate ether could explain well the observation of water enhancement effect in 2,5-hexanediol dehydration over MFI-140 (Fig. 27c).

The inhibition effect of GVL on dehydration of DMTHF was further investigated by varying partial pressure of GVL. The results in Fig. 36d clearly show that the inhibition effect of GVL in DMTHF dehydration increases with the partial pressure of GVL. This observation suggests that GVL inhibits the dehydration of 2,5-dimethyltetrahydrofuran by competitive adsorption on acid sites. In fact, GVL was found to convert to pentenoic acid isomers under the reaction conditions in this study. As GVL competes for the acid sites, the surface coverage of DMTHF under different co-feeding conditions would be influenced consequently.

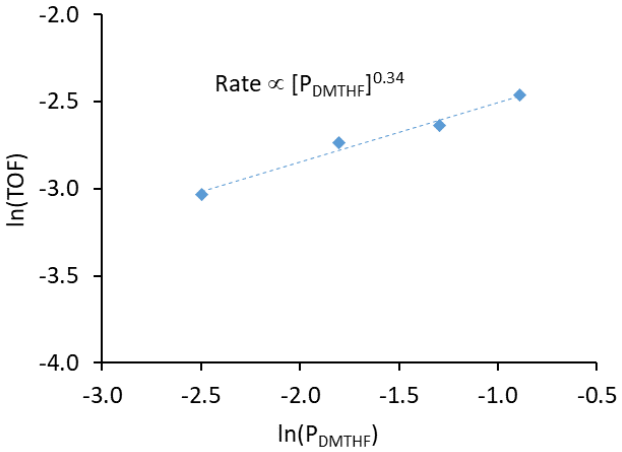

Fig. 37. Reaction order of 2,5-dimethyltetrahydrofuran dehydration with respect to 2,5-dimethyltetrahydrofuran over MFI-140. T = 250°C, P_{DMTHF} = 0.08 – 0.4 kPa

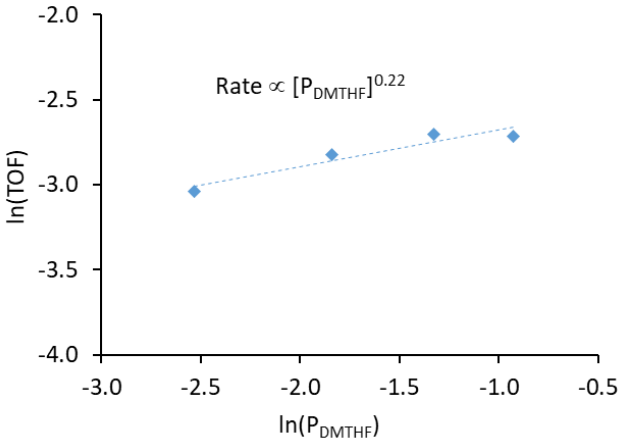

Fig. 38. Reaction order of 2,5-dimethyltetrahydrofuran dehydration with respect to 2,5-dimethyltetrahydrofuran over MFI-140. T = 250°C, P_{DMTHF} = 0.08 – 0.4 kPa, P_{water} = 3.5 kPa

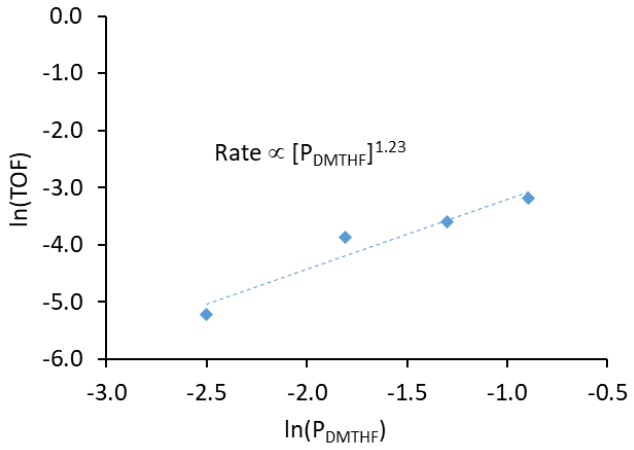

Fig. 39. Reaction order of 2,5-dimethyltetrahydrofuran dehydration with respect to 2,5-dimethyltetrahydrofuran over MFI-140. T = 250°C, P_{DMTHF} = 0.08 – 0.4 kPa, P_{GVL} = 0.6 kPa

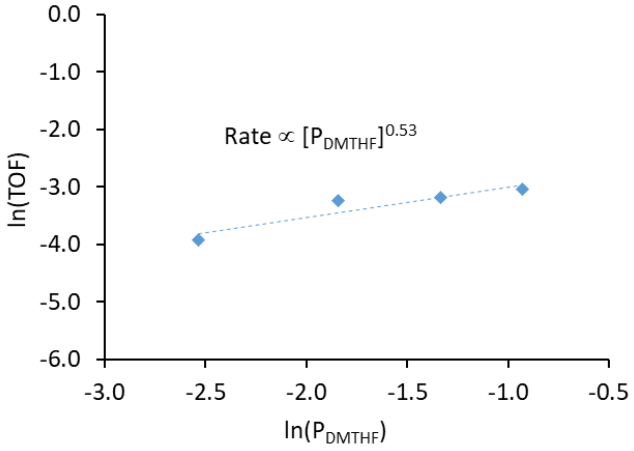

Fig. 40. Reaction order of 2,5-dimethyltetrahydrofuran dehydration with respect to 2,5-dimethyltetrahydrofuran over MFI-140. T = 250°C, P_{DMTHF} = 0.08 – 0.4 kPa, P_{water} = 3.5 kPa, P_{GVL} = 0.6 kPa

The change in reaction order of DMTHF dehydration with respect to DMTHF in different co-feeding experiments over MFI-140 suggests that the adsorption state is altered under these reaction conditions. The reaction orders of DMTHF dehydration with respect to DMTHF with and without co-feeding water are 0.22 and 0.34 respectively. In this case, the catalyst surface is nearly

saturated by DMTHF, which suggests the strong interaction of cyclic ether with Brønsted acid sites. Then, co-feeding GVL increases the reaction order of DMTHF to 1.23, which means that the surface coverage of DMTHF in MFI-140 catalyst is reduced. This observation is likely due to the competitive adsorption of GVL on Brønsted acid sites as aforementioned. Interestingly, adding water with GVL changes the apparent reaction order with respect to P_{DMTHF} to 0.53, suggesting greater surface coverage by DMTHF. Clearly, the initial turnover frequency of hexadiene formation correlates well with apparent reaction order and therefore surface coverage of DMTHF in zeolite catalysts. It is noted that in the presence of water, protons on the zeolite framework are delocalized to form hydronium ion clusters acting as mobile Brønsted acid sites under these reaction conditions. As a result, the heat of adsorption of DMTHF and GVL on conventional Brønsted acid site and hydronium ion cluster could be altered, leading to the different surface coverage of DMTHF in the absence and presence of water molecules inside zeolite pores.

The apparent activation energy of hexadienes formation in 2,5-hexanediol dehydration in the presence of GVL over MFI-140 with and without water co-feeding was estimated by an Arrhenius plot over the temperature range of 220°C to 250°C.

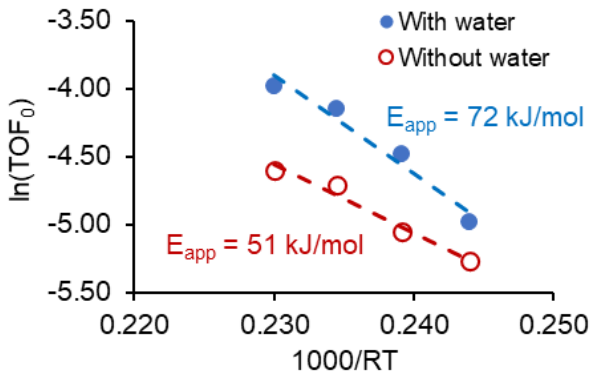

Fig. 41. Apparent activation energy of hexadienes formation in 2,5-hexanediol dehydration over MFI-140. Reaction conditions: $P_{2,5\text{-hexanediol}}$ = 0.09 kPa, P_{GVL} = 0.6 kPa, P_{water} = 0 kPa (without water) or 3.5 kPa (with water)

As shown in Fig. 41, the apparent activation energy of hexadienes formation over MFI-140 in the presence of water is higher than that in the absence of water. The presence of water enables higher surface coverage by the intermediate 2,5-dimethyltetrahydrofuran as shown by reaction order results in Fig. 36c. As a result, the heat of adsorption of cyclic ether may be incorporated in the measured activation energy for the reaction in the presence of water, while the activation energy in the absence of water is referenced to gas phase due to the first-order reaction. Consequently, the measured energy barrier of 2,5-hexanediol dehydration in the presence of GVL is higher when water is co-fed. The difference of activation energy in the presence and absence of water is about 21 kJ/mol, which is consistent with the calculated heat of adsorption of DMTHF in the presence of GVL and water molecules.

DFT analysis in the effect of GVL and co-fed water on the dehydration of DMTHF

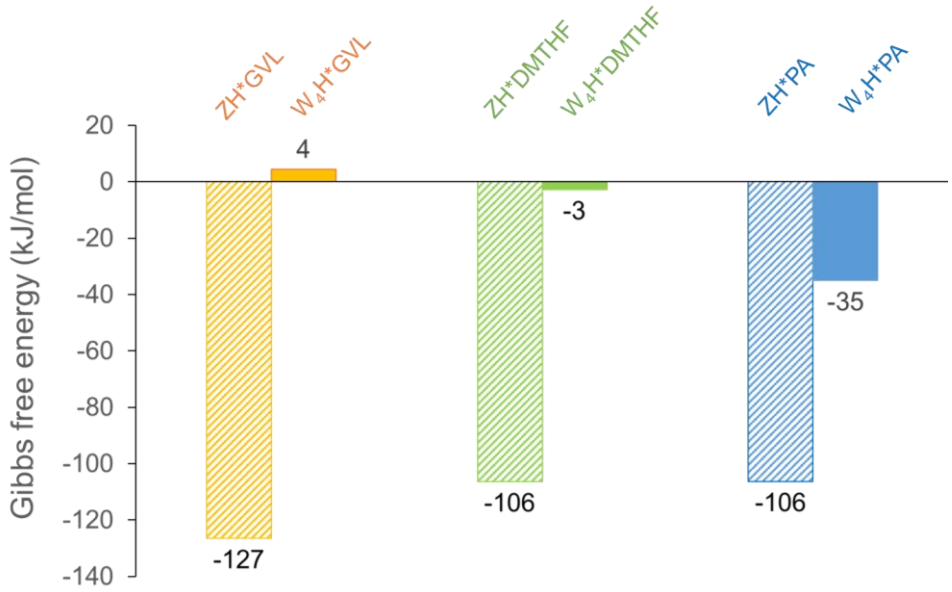

Fig. 42. Gibbs free energy of adsorption of GVL, DMTHF, and pentenoic acid. Z: zeolite framework; H: the proton; ZH: the framework Brønsted acid site ("conventional" BAS); GVL: γ-valerolactone; DMTHF: 2,5-dimethyl tetrahydrofuran; PA: pentenoic acid isomers; W: water; W4: cluster of four water molecules; W4H: the hydronium cluster ("mobile" BAS).

To further investigate the inhibitory effect of GVL in the absence of co-fed water on the conversion of DMTHF, we performed DFT calculations on the energetics of molecular adsorption over the Brønsted acid sites (Fig. 42 and Fig. 43). As shown in Fig. 42, the Gibbs free energy of GVL adsorption (-127 kJ/mol) is substantially greater than that of DMTHF (-106 kJ/mol). Accordingly, the equilibrium constant of GVL adsorption is a hundred times higher than that of DMTHF (Table 6). The result suggests that GVL should predominate the catalyst surface coverage; the hexadienes formation from DMTHF in the presence of GVL, compared to that in the solvent-free condition, will exhibit a decreased TOF and an increase in the reaction order with respect to DMTHF. In addition, Fig. 42 shows that PA isomers, which are the ring-opening products of GVL, could also suppress the surface coverage of DMTHF due to their comparable Gibbs free energies of adsorption (Table 6). These findings are consistent with the experimental observations depicted in Fig. 27c and Fig. 35.

Table 6. Adsorption energetics of species on the Brønsted acid sites

No.	Process	ΔE_{ZPVE}	$\Delta E_{DFT\text{-}D3}$	ΔU	ΔH	ΔS	ΔG	K_{ads}
1	ZH + GVL → ZH*GVL	0.2	-164.9	-167.4	-171.8	-86.5	-126.5	$4.3x10^{12}$
2	ZH + DMTHF → ZH*DMTHF	6.0	-166.7	-164.3	-168.6	-119.1	-106.4	$4.2x10^{10}$
3	ZH + PA → ZH*PA	2.8	-154.6	-155.5	-159.9	-102.4	-106.3	$4.1x10^{10}$
4	ZH + 4W → Z+W_4H	30.5	-293.1	-274.1	-291.5	-268.9	-150.8	$1.1x10^{15}$
5	W_4H + GVL →W_4H*GVL	8.8	-41.8	-38.7	-43.1	-90.9	4.5	$3.6x10^{-1}$
6	W_4H + E → W_4H*E	12.6	-59.8	-56.6	-61.0	-111.3	-2.7	$1.9x10^{0}$
7	W_4H + PA → W_4H*PA	8.9	-76.8	-76.6	-81.0	-87.8	-35.0	$3.1x10^{3}$

Z: zeolite framework; H: the proton; ZH: the framework Brønsted acid site (“conventional” BAS); GVL: γ-valerolactone; DMTHF: 2,5-dimethyl tetrahydrofuran; PA: pentenoic acid isomers; W: water; W_4: cluster of four water molecules; W_4H: the hydronium cluster (“mobile” BAS).

The energy differences (ΔU, ΔH, and ΔG) are displayed in the unit of kJ/mol. The entropy difference (ΔS) is displayed in the unit of J/mol.K. The first three processes describe the adsorptions of γ-valerolactone (GVL), the intermediate cyclic ether (DMTHF) and pentenoic acid isomers (PA) over the framework Brønsted acid site, respectively. The No. 4 reaction presents the formation of the hydronium cluster (W_4H) induced by four molecules of co-fed water. The last three reactions are written for the adsorptions of GVL, DMTHF and PA on the hydronium cluster.

To understand the mechanism by which co-fed water remediates the surface coverage of DMTHF and thus improves the TOF of hexadienes formation, and why it only works in the presence of GVL but not in the DMTHF-alone system, we performed DFT calculations on the adsorption of relevant species in the presence of four water molecules per acid site (based on experimental measurement of four moles of water per acid site). It is demonstrated that the proton on the zeolite framework (or "conventional” BAS) could be transferred into the cluster of four co-fed water molecules, which results in the formation of a “mobile” proton (Fig. 43d). This phenomenon has been observed when more than two water molecules are introduced per site [4].

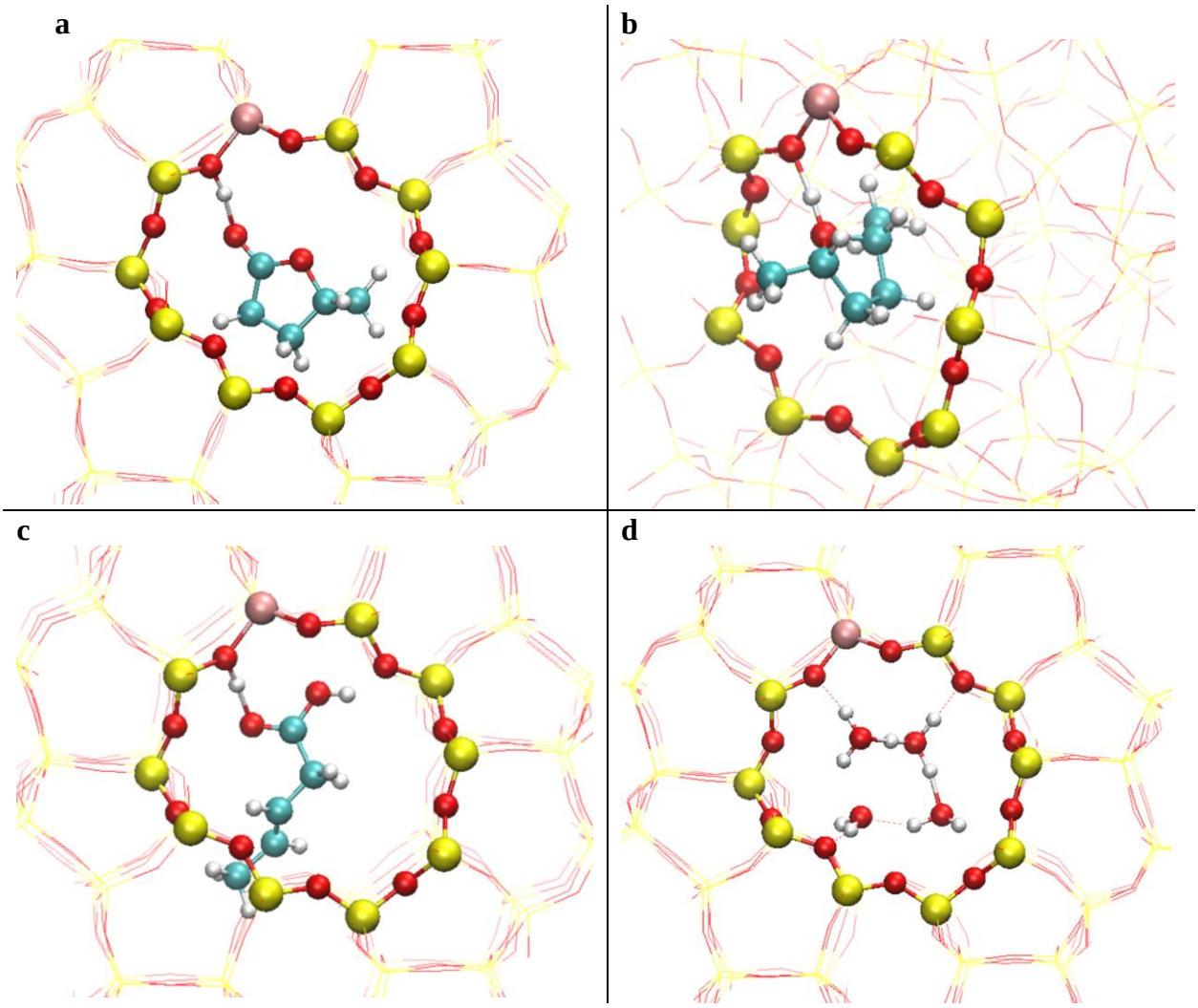

Fig. 43. The DFT optimized structures over the framework Brønsted acid site. The aluminum, silicone, oxygen, carbon, and hydrogen atoms are, respectively, colored by pink, yellow, red, yellow, and white. **a,** γ-valerolactone (GVL). **b,** 2,5-dimethyl tetrahydrofuran (DMTHF). **c,** pentenoic acid isomers (PA). **d,** hydronium cluster

On the mobile proton, the competitive adsorption of GVL could be further suppressed as compared to conventional BAS. As depicted in Fig. 42 and Fig. 44, GVL adsorption on the hydronium cluster exhibits an almost thermoneutral Gibbs free energy similar to DMTHF. As a result, the equilibrium constant of GVL adsorption on the mobile proton is decreased (Table 6); which leads to a higher coverage of DMTHF, a reduced reaction order of DMTHF, and an

improved TOF of hexadienes formation. These findings are consistent with experimental observations shown in Fig. 27c. The experimental observations (Fig. 27c) that, in the absence of GVL, water co-feeding shows no significant changes on the TOF of hexadienes formation can be attributed to the high coverage of DMTHF with and without co-fed water and similar intrinsic activation barriers in both cases.

Detailed analysis in energetics of adsorption (Table 6) reveals that, despite exhibiting a higher adsorption heat than DMTHF, the dominantly competitive adsorption of GVL should be attributed to the entropic contribution. The result might appear counterintuitive as the greater enthalpy acquired has been commonly reported in exchange with the greater entropy lost [138-140]. In this study, however, we found that GVL molecule with a less bulky structure (Fig. 43) is much more facile to access the BAS with a reduced entropy cost, which consequently leads to the highly competitive adsorption of GVL over the adsorption of DMTHF. Whilst the confinement effect on the adsorption entropy loss has not been adequately investigated, Gounder and Iglesia found that this factor can, indeed, notably alter the energy state of precursors and hence influence the activation barriers [19]. Therefore, the aforementioned result implies that the utilization of confined environment in tuning the catalyst activity and product selectivity should be further considered for our polymeric reactions later.

Another evidence to support water-induced coverage change is experiments with co-fed PA, which is a ring-opening product of GVL. Different from GVL and DMTHF, the hydronium cluster substantially favors the adsorption of PA isomers (Table 6). This distinct effect suggests that a small amount of PA resulted from the ring-opening of GVL could inhibit the hexadienes formation due to its competitive adsorption on the surface. This finding thus explains the

experimental observation that the water co-feeding is not able to promote hexadienes formation in the presence of PA (Fig. 35).

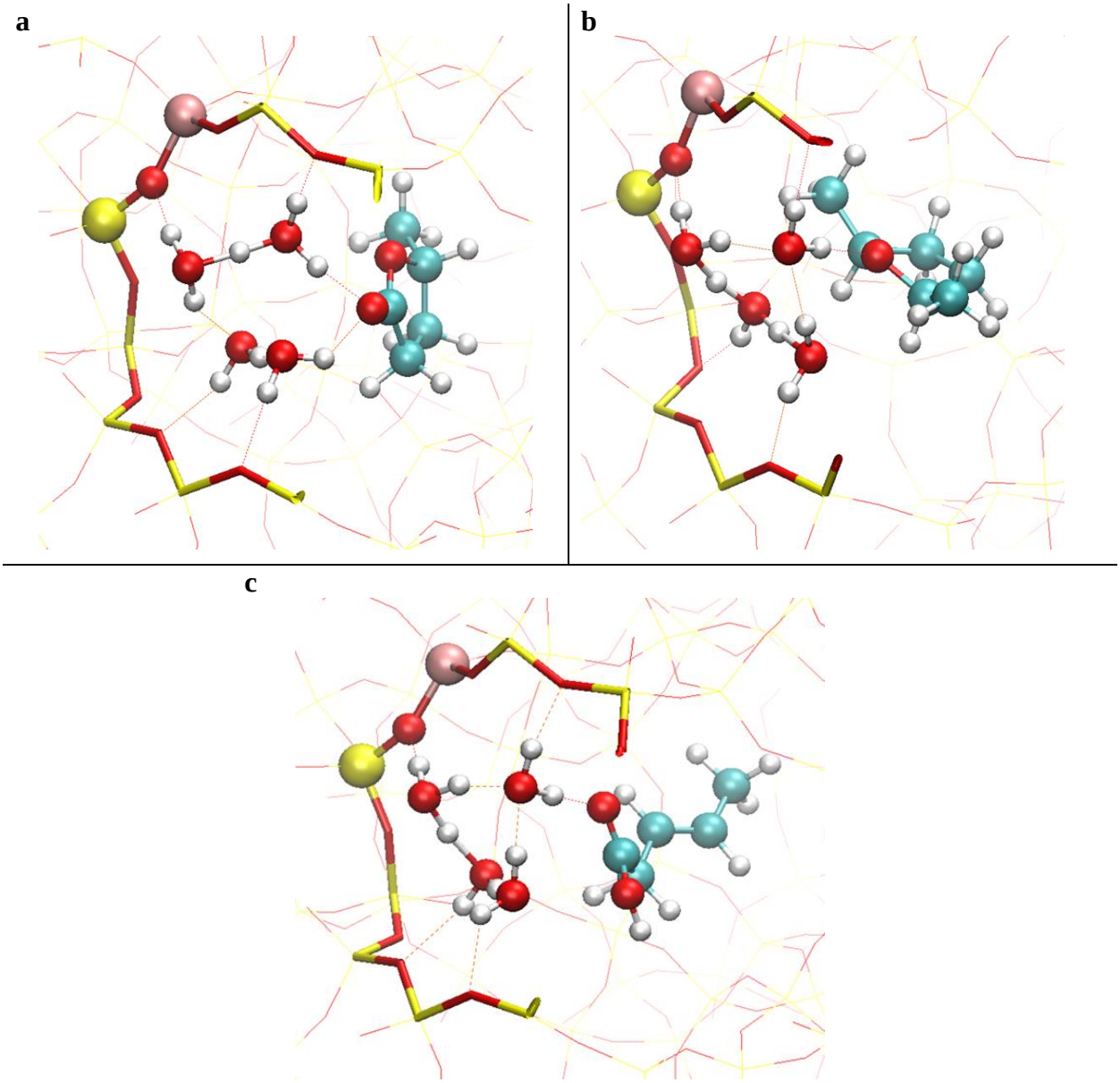

Fig. 44. The DFT optimized structures on the hydronium cluster. The aluminum, silicone, oxygen, carbon, and hydrogen atoms are, respectively, colored by pink, yellow, red, yellow, and white. **a,** γ-valerolactone (GVL). **b,** 2,5-dimethyl tetrahydrofuran (DMTHF). **c,** pentenoic acid isomers (PA).

Effect of water on dehydration of real EVOH polymer

The dehydration of real EVOH polymer over solid acid catalyst at 120°C in the presence of polar aprotic solvent was investigated in a batch reactor. Nitrogen atmospheric environment was applied to minimize the side reactions in ambient air.

The dried solid product of EVOH dehydration over MFI-140 zeolite in GVL solvent was analyzed by FT-IR instrument (Fig. 45a and Fig. 45b). The FT-IR spectra of EVOH powder and dehydrated solid products after 2-hour liquid phase reaction are shown in Fig. 45a with the appearance of the typical peaks such as O-H stretching at 3700-3000 cm^{-1}, C-H stretching at 3000-2700 cm^{-1}, O-H bending at 1590-1270 cm^{-1}, and C-O stretching at 1270-970 cm^{-1}. The FT-IR spectra of EVOH powder and solid product after mixing with GVL in the absence of catalyst are identical. After adding MFI-140 catalyst with the catalyst-to-polymer mass ratio of 1:3, we see a shift of C-O stretching peak from 1170-970 cm^{-1} to a higher wavenumber range of 1270-1100 cm^{-1}. This observation indicates the transformation of secondary alcohol bonding in EVOH to a more ether-like bonding with the presence of solid acid catalyst. Another new feature showing up in FT-IR spectra with adding MFI-140 zeolite in Fig. 45a is the highlighted region of C=O stretching at 1810-1680 cm^{-1}. This C=O stretching peak is the indication of the dehydration of EVOH as explained in Fig. 45c. As EVOH undergoes dehydration with the presence of MFI-140 zeolite, C=C double bonds are formed with the elimination of water molecules. The IR absorption band for C=C stretching at 1680-1600 cm^{-1} is not visible in FT-IR spectra as shown in Fig. 45a, which suggests that there are subsequent reactions related to these C=C double bonds. In fact, the appearance of C=O stretching band has been observed during thermal or ion induced degradation of polyvinyl alcohol, which is attributed to double bond migration via hydride shift mechanism followed by keto-enol tautomerization [141-143].

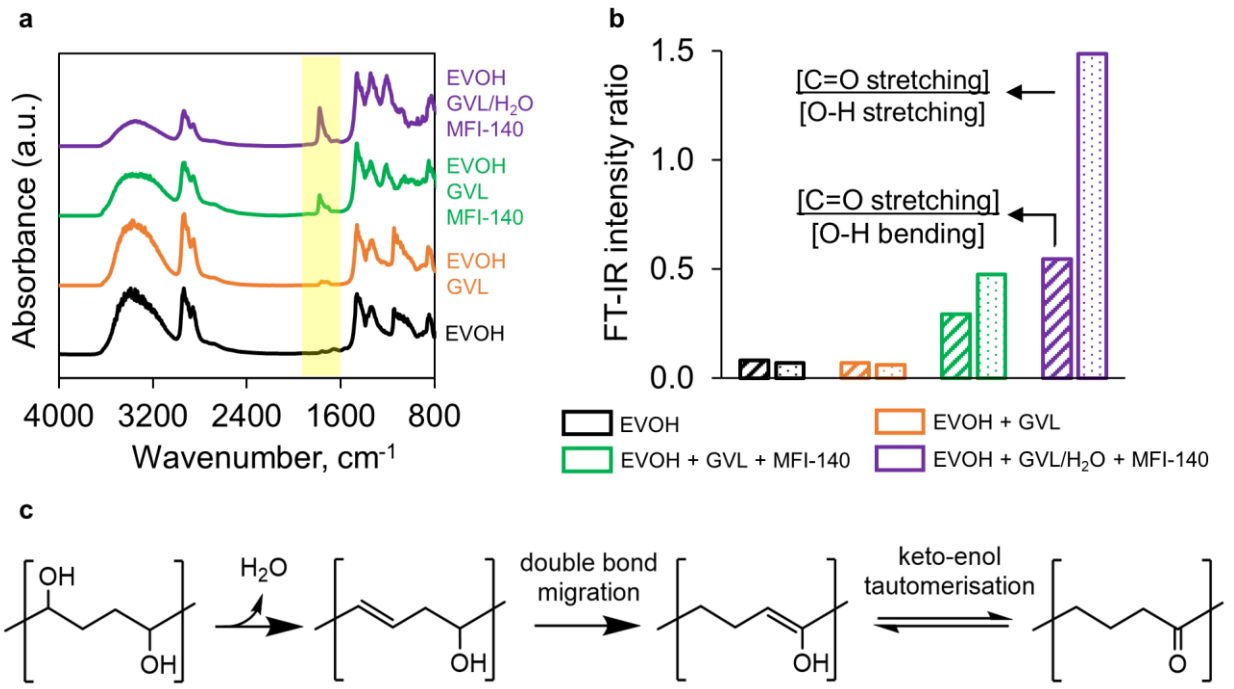

Fig. 45. Dehydration of EVOH polymer. **a,** FT-IR spectra of original EVOH powder and dried solid products after reactions in liquid phase. Reaction conditions: 300 mg EVOH powder, 20 ml solvent, 100 mg MFI-140, T = 120°C, reaction time = 2 h, stirring = 600 rpm. **b,** FT-IR peak intensity ratios of C=O stretching to O-H bending or O-H stretching of original EVOH powder and dried solid products after reactions in liquid phase. **c,** Illustrated scheme for the formation of C=O double bonds in EVOH dehydration over solid acid catalyst in GVL solvent.

The conversion of EVOH by dehydration is indicated indirectly via FT-IR intensity ratio of C=O stretching to O-H stretching or O-H bending as shown in Fig. 45b. Interestingly, adding water to the reaction mixture with the volumetric ratio of GVL:H_2O = 9:1 has shown a significant enhancement in these IR band intensity ratios. This observation implies that the positive effect of water on 2,5-hexanediol model compound is also applicable to the real EVOH dehydration over MFI-140 zeolite in the presence of GVL solvent.

Conclusion

Water shows an enhancement effect on EVOH polymer dehydration over MFI-140 in the presence of GVL solvent, which was investigated via the study of the model compound. The reaction pathway of 2,5-hexanediol dehydration over H-ZSM-5 zeolites was found to proceed via 2,5-dimethyltetrahydrofuran intermediate to form hexadiene isomers. It was found that surface coverage of the intermediate ether (2,5-dimethyltetrahydrofuran) decreases in the presence of GVL due to the competitive adsorption of GVL, which eventually undergoes ring-opening to form pentenoic acids. In the absence of GVL solvent, water does not influence the dehydration of the intermediate ether. Interestingly, the co-presence of water would mitigate the inhibition effect of GVL and improve the formation of hexadienes. The presence of water inside zeolite pores is known to facilitate delocalization of Brønsted acid sites to form hydronium ion clusters which act as mobile acid sites. Therefore, the accessibility of the intermediate ether (2,5-dimethyltetrahydrofuran) to acid sites in the presence of GVL is improved when water is co-fed as indicated by the concomitant increase in the apparent reaction order with respect to the ether. As a result, the inhibition effect of GVL is mitigated by the formation of hydronium ion clusters in the presence of water, leading to a higher rate of hexadienes formation. These findings provide mechanistic insights to guide the design of robust catalytic systems for the real EVOH polymer dehydration as well as mixed plastics recycling.

Methods

Reagents

Poly(vinyl alcohol-co-ethylene) (EVOH, ethylene 32 mol %) in pellet form was purchased from Sigma-Aldrich and was cryogenically ground to obtain fine powder form. 2,5-hexanediol

(99%, mixture of isomers, Sigma-Aldrich), γ-valerolactone (GVL, ≥ 99%, Sigma-Aldrich), 2,5-dimethyltetrahydrofuran (DMTHF, mixture of cis and trans, 96%, Sigma-Aldrich), 2,4-hexadiene (mixture of isomers, 90%, Sigma-Aldrich), 1,5-hexadiene (97%, Sigma-Aldrich), n-hexane (99%, Sigma-Aldrich), 1-hexene (97%, Sigma-Aldrich), 4-pentenoic acid (97%, Sigma-Aldrich) were obtained from the commercial supplier and used as received.

Catalyst preparation

ZSM-5 zeolites with two different Si/Al ratios were purchased in the ammonium form NH_4-ZSM-5 from Zeolyst International (CBV-5524G with Si/Al = 25, CBV-8014 with Si/Al = 40, CBV-28014 with Si/Al = 140). Beta zeolite (Si/Al = 133) was obtained in proton-form H-Beta from Alfa Aesar. Sodium exchange of NH_4-ZSM-5 (CBV-8014) was carried out to titrate a fraction of the Brønsted acid sites. NH_4-ZSM-5 (CBV-8014) samples were mixed with 0.5 M $NaNO_3$ solution with the ratio of 20 ml solution per gram catalyst. Deionized water and commercial $NaNO_3$ (Sigma Aldrich, ACS Reagent, ≥ 99.0%) were used to prepare $NaNO_3$ solution. The mixture of NH_4-ZSM-5 powder and $NaNO_3$ solution was stirred for 12 hours at room temperature. Then, the solution was centrifuged, and the solid part was washed five times with deionized water followed by a drying step at 80°C in a vacuum oven for 24 hours.

All catalyst samples (except Beta zeolite in proton form) were calcined in flowing dry air with the ramping rate of 2°C /min up to 600°C and kept at that temperature for 5 hours to obtain proton-form H-ZSM-5. Protonated zeolites were then pelletized, crushed, and sieved to particles with sizes ranging from 90 to 250 μm. H-ZSM-5 zeolites with Si/Al = 25, Si/Al = 40, Si/Al = 140, and sodium-titrated samples are denoted as MFI-25, MFI-40, MFI-140, and Na-MFI-40, respectively. H-Beta zeolite (Si/Al = 133) is denoted as BEA-133.

Characterization

Temperature-programmed reaction (TPRx) of isopropylamine (IPA) coupled with a MKS Cirrus 200 quadrupole mass spectrometer (MS) was carried out on catalyst samples to determine Brønsted acid site (BAS) densities of these catalysts. The details of this method are described elsewhere [89].

Thermogravimetric analysis (TGA) was performed on a Netzsch STA 449F1 equipped with a pin thermocouple and a Netzsch nano-balance to quantify the number of water molecules per acid site in MFI-140. Catalyst was dried by heating up to 300°C with the ramping rate of 10°C/min and kept for 1 hour in flowing helium (125 ml/min) before introducing water at 3.5 kPa in a flow reactor. Then catalyst was transferred to the crucible and heated from 40°C to 600°C at the ramp rate of 5°C/min in flowing argon (20 ml/min). The number of water molecules per Brønsted acid site in MFI-140 was quantified based on the desorption of water from the catalyst indicated by the weight loss of the sample and the Brønsted acid site density from IPA-TPRx experiment.

Fourier-transform infrared (FT-IR) spectroscopy was carried out in a PerkinElmer Spectrum 100 Fourier Transform Infrared (FT-IR) spectrometer equipped with a high-temperature diffuse reflectance Infrared Fourier Transformation (DRIFT) CaF_2 cell (HVC, Harrick). A blank run of KBr pellet was obtained for the background. The solid samples were pretreated as described below before obtaining FT-IR spectra in He inert atmosphere.

Catalytic testing

Dehydration of EVOH was carried out in a PTFE bottle in nitrogen atmosphere, which was heated by a silicon oil bath. EVOH fine powder and the solvent were stirred and heated to the

reaction temperature before adding the catalyst and starting the reaction. The reaction mixture was stirred with PTFE magnetic stir bar at 600 rpm in all experiments. After the reaction, the product was filtered to separate the liquid and solid parts. The liquid part was analyzed by GC-MS and showed no conversion of solvent under the reaction conditions. The solid part was washed with deionized water and dried in a vacuum oven at 80°C overnight to remove residual solvent before FT-IR analysis.

Vapor phase flow reactions over zeolite catalysts were conducted in a quartz tube reactor (1/4" OD) at atmospheric pressure. The catalyst was mixed with acid-washed glass beads and packed between quartz wool layers in the quartz reactor. The quartz reactor was installed inside an oven whose temperature was controlled by a thermocouple inside the quartz reactor and beneath the catalyst bed. Before injecting reactants, physisorbed water in catalyst samples were removed by heating samples to 300°C with the ramping rate of 10°C/min and kept for 1 hour in flowing helium (125 ml/min). The oven temperature was then set to reach the desired reaction temperature. Reactants were injected to the reactor through septa on a heated vaporization zone using KD Scientific syringe pumps. To prevent the condensation of reaction products on the downstream tubing, the outlet of the reactor was heated to 250°C. Samples were collected at different reaction time on stream (TOS) using a gas sample loop connected with a six-port valve and products were analyzed by a Hewlett Packard 6890 gas chromatograph equipped with a flame ionization detector and an INNOWAX column (30 m × 0.25 mm).

To decouple kinetic effects from catalyst deactivation over reaction time on stream in flow reactions, all of reaction rates were extrapolated to zero-time on stream to obtain initial rates which are used in reaction order and activation energy plots.

$$\text{Reaction space time} = \frac{\text{Mass of catalyst (g)}}{\text{Reactant flow rate (g/h)}} \quad (9)$$

$$\text{Product yield (mol\%)} = \frac{\text{Product flow rate (mol/s)}}{\text{Reactant flow rate (mol/s)}} \times 100\% \quad (10)$$

$$\text{Turnover frequency } (1/\text{s}) = \frac{\text{Mole of product formed per gram catalyst (mol/g}_{\text{cat}}\text{.s)}}{\text{Brønsted acid site density (mol H}^{+}\text{/g}_{\text{cat}}\text{)}} \quad (11)$$

DFT calculations

The Vienna Ab Initio Simulation Package (VASP) [144] was used to calculate all electronic energies using density functional theory (DFT). Description of the electron-ion interactions was carried out by the projector-augmented wave (PAW) [145, 146] approach with a plane-wave energy cutoff of 400 eV. The exchange correlation energies were computed by the generalized gradient approximation (GGA) with Perdew-Burke-Ernzerhof (PBE) functional [147]. The van de Waal interactions was accounted by using the DFT-D3 semiempirical method [148]. Iteration of self-consistency loops with convergence level of 10^{-5} - 10^{-7} eV and maximum atomic force criterion of less than 0.01 eV $Å^{-1}$ were employed to optimize the structures. A literature model for the adsorbate entropy in zeolite [149] was applied to estimate the entropy lost when a gaseous molecule adsorbs into the zeolite pore. For calculations of zero-point energy (ZPE), the vibrational frequencies at 0K were obtained by the Partial Hessian Vibrational Analysis (PHVA) [150]. The internal energy (U), enthalpy (H), entropy (S), Gibbs free energy (G) and equilibrium constants (K_a) corrected at the reaction conditions were calculated based on the statistical thermodynamics [151].

A periodic unit cell of H-ZSM5 employed in this paper consists of 96 tetrahedral sites [152] with the lattice constants set to a = 20.078 Å, b = 19.894 Å, and c =13.372 Å, as in our previous work [15, 81, 153]. The Bronsted acid site (BAS) was constructed by replacement of a Si atom at a T7-site with one Al atom. The proton was placed in the oxygen bisecting T7 and T8 sites as in

our previous work [15]. The molecules in the gas phase were positioned into a cube with the lattice constant of 30 Å.

Acknowledgements

The authors are grateful for the support from the National Science Foundation under Grant No. EFRI E3P-2029394 to carry out this research. The computations were performed at the OU Supercomputing Center for Education & Research and the National Energy Research Scientific Computing Center (NERSC), a U.S. Department of Energy Office of Science User Facility. B.W. thanks support from the U.S. Department of Energy, Basic Energy Sciences (Grant DE-SC0018284).

Chapter 5: Concluding remarks

In this work, the diverse roles of water on different vapor phase reactions in a fixed-bed reactor has been investigated. Previous literature has shown that the presence of water exerts detrimental effects on different reactions of oxygenates and hydrocarbons such as acylation, ketonization, dehydration, and alkane cracking which are attributed to the interaction with surface active acyl species, affecting reaction equilibrium, competitive adsorption, stabilizing adsorption state, and poisoning the Lewis/Brønsted acid synergistic sites. However, co-feeding water with a bulky ester as an acylating agent over a high-silica MFI zeolite within internal diffusion limited regime enhances the acylation of m-cresol with acetic acid. In fact, water can hydrolyze the bulky ester to form small molecules which diffuse faster inside the zeolite pores to generate kinetic relevant active intermediate ester near Brønsted acid sites at pore intersections, leading to a higher reaction rate. This positive effect of water on mass transfer of reaction intermediates can be extended to the conversion of other oxygenates which involve hydrolyzable active species.

As the partial pressure of water is sufficient to delocalize the framework protons and form stable hydrated hydronium ions inside zeolite pores, water can influence the reactant adsorption states and reaction transition states which consequently has significant impacts on catalytic reaction rates and catalyst stability against coking.

The enhancement effect of water on dealkylation of cumene, which is a non-polar hydrocarbon, is very intriguing. The higher turnover frequency of cumene dealkylation in the presence of water was attributed to the entropic gain of the reaction transition state associated with hydronium ion clusters. As site proximity also shows a similar entropic effect as water, the improvement of cumene dealkylation rate with water co-feeding can happen at lower temperatures in reactions over zeolites with the presence of paired acid sites.

On the other hand, in the dehydration of a di-alcohol with the presence of polar aprotic solvent such as gamma-valerolactone over Brønsted zeolites, the change in the adsorption favorability of the reaction intermediate versus the competitive adsorbate on hydrated hydronium ions compared to conventional framework proton enables a higher surface coverage of the reactant in the presence of water. As a result, co-feeding water can reduce the competitive adsorption of the polar aprotic solvents and improves the dehydration of polyols in the presence of these solvents.

In conclusion, as water is a cheap and readily available material, mechanistic understanding of the diverse role on water on diffusion, adsorption, and catalytic rate of various chemical transformations over zeolites would enable us to design more novel and stable catalytic systems. As a result, the conversion, product selectivity, and catalyst stability of complex reactions can be manipulated to achieve optimal performance.

Chapter 6: Future works

Although various roles of water have been studied and revealed in this work, there are open questions about the kinetic effect of water on catalytic reactions that require further investigation. For example, co-feeding a small amount of water has shown an enhancement in the acylation of m-cresol with either bulky ester or acetic acid over a high-silica H-Beta zeolite. It is expected that this reaction is not limited by internal diffusion, and the concentration of water is not sufficient to form hydrated hydronium ions.

It is known that the reaction kinetically relevant step and the energy barrier of alcohol dehydration are influenced by the presence of water and paired acid sites. Therefore, the effect of water on alcohol dehydration in contrast to cumene dealkylation over zeolites with or without the presence of paired acid sites is also worth investigating to reveal the role of the reactant polarity.

The other area that needs further exploration is the effect of water on the dehydration of pentanediol, which has a closer distance between two hydroxyl groups compared to hexanediol and is less likely to form cyclic ether intermediate as a model compound for EVOH transformation. This reaction, in combination with the dehydration of hexanediol, would provide insightfully mechanistic views of the dehydration of polar polymers like EVOH, as there is a diverse distribution of hydroxyl groups on the C-C backbone in this polymer. In addition, it is of great practical interest to study the effect of water on the dehydration of polyols in the presence of dimethyl sulfoxide solvent, which can solubilize the polar polymer at low temperature over catalysts with more accessible active sites such as sulfonic acid-functionalized silica with varying acid site density.

Regarding the effect of water solvent on the hydrogenation of phenolic compounds over supported metal catalysts, more robust catalytic systems can be developed by depositing the metal

particles inside the carbon nanotubes to carry out the selective hydrogenation of different molecules, including dehydrated polymer molecules. Various methods to open the caps of the carbon nanotubes can be utilized, such as sonication and pretreatment with nitric acid. However, the treatment conditions of these approaches have to be optimized to minimize undesired side effects like buckling of carbon nanotubes, lattice dislocations on the tube surface, and creating more carboxylic acid defects on the nanotube surface. The role of the hydrophilicity of catalyst support on the adsorption/desorption properties of the reaction intermediate is critical, which can be revealed by comparing the reactions over Pd/SiO_2 versus hydrophobic Pd/SiO_2 catalyst functionalized by silane agents.

By designing catalysts and studying the kinetics of probe reactions properly in combination with molecular modeling, the future works would enable us to acquire the fundamental understanding of interactions of water with active sites and reaction molecules at the molecular level. The outcome of this research would not only be a significant contribution to the catalysis community but also be of great importance to industrial processes to maximize the yield of desired products and prolong the catalyst lifetime by utilizing inexpensive and readily material such as water.

References

[1] B. M. Weckhuysen and J. Yu, Recent advances in zeolite chemistry and catalysis, Chemical Society Reviews 44 (2015) 7022-7024.

[2] A. Corma, State of the art and future challenges of zeolites as catalysts, Journal of Catalysis 216 (2003) 298-312.

[3] J. Dědeček, E. Tabor, and S. Sklenak, Tuning the aluminum distribution in zeolites to increase their performance in acid-catalyzed reactions, ChemSusChem 12 (2019) 556-576.

[4] G. Li, B. Wang, and D. E. Resasco, Water-mediated heterogeneously catalyzed reactions, ACS Catalysis 10 (2019) 1294-1309.

[5] C. J. Heard, L. Grajciar, F. Uhlík, M. Shamzhy, M. Opanasenko, J. Čejka, and P. Nachtigall, Zeolite (In) Stability under Aqueous or Steaming Conditions, Advanced Materials 32 (2020) 2003264.

[6] L. Zhang, K. Chen, B. Chen, J. L. White, and D. E. Resasco, Factors that determine zeolite stability in hot liquid water, Journal of the American Chemical Society 137 (2015) 11810-11819.

[7] Z. Zhao, R. Bababrik, W. Xue, Y. Li, N. M. Briggs, D.-T. Nguyen, U. Nguyen, S. P. Crossley, S. Wang, B. Wang, and D. E. Resasco, Solvent-mediated charge separation drives alternative hydrogenation path of furanics in liquid water, Nature Catalysis 2 (2019) 431-436.

[8] N. Xue, A. Vjunov, S. Schallmoser, J. L. Fulton, M. Sanchez-Sanchez, J. Z. Hu, D. Mei, and J. A. Lercher, Hydrolysis of zeolite framework aluminum and its impact on acid catalyzed alkane reactions, Journal of Catalysis 365 (2018) 359-366.

[9] D. E. Resasco, S. P. Crossley, B. Wang, and J. L. White, Interaction of water with zeolites: a review, Catalysis Reviews 63 (2021) 302-362.

[10] K. Stanciakova and B. Weckhuysen, Water–active site interactions in zeolites and their relevance in catalysis, Trends in Chemistry 3 (2021) 456-468.

[11] H. Wang, Y. Hou, W. Sun, Q. Hu, H. Xiong, T. Wang, B. Yan, and W. Qian, Insight into the Effects of Water on the Ethene to Aromatics Reaction with HZSM-5, ACS Catalysis 10 (2020) 5288-5298.

[12] K. De Wispelaere, C. S. Wondergem, B. Ensing, K. Hemelsoet, E. J. Meijer, B. M. Weckhuysen, V. Van Speybroeck, and J. Ruiz-Martínez, Insight into the Effect of Water on the Methanol-to-Olefins Conversion in H-SAPO-34 from Molecular Simulations and in Situ Microspectroscopy, ACS Catalysis 6 (2016) 1991-2002.

[13] P. Bollini, T. T. Chen, M. Neurock, and A. Bhan, Mechanistic role of water in HSSZ-13 catalyzed methanol-to-olefins conversion, Catalysis Science & Technology 9 (2019) 4374-4383.

[14] A. Vjunov, M. Wang, N. Govind, T. Huthwelker, H. Shi, D. Mei, J. L. Fulton, and J. A. Lercher, Tracking the Chemical Transformations at the Brønsted Acid Site upon Water-Induced Deprotonation in a Zeolite Pore, Chemistry of Materials 29 (2017) 9030-9042.

[15] M. Zeets, D. E. Resasco, and B. Wang, Enhanced chemical activity and wettability at adjacent Brønsted acid sites in HZSM-5, Catalysis Today 312 (2018) 44-50.

[16] M. Wang, N. R. Jaegers, M.-S. Lee, C. Wan, J. Z. Hu, H. Shi, D. Mei, S. D. Burton, D. M. Camaioni, O. Y. Gutiérrez, V.-A. Glezakou, R. Rousseau, Y. Wang, and J. A. Lercher, Genesis and stability of hydronium ions in zeolite channels, Journal of the American Chemical Society 141 (2019) 3444-3455.

[17] K. Chen, A. Gumidyala, M. Abdolrhamani, C. Villines, S. Crossley, and J. L. White, Trace water amounts can increase benzene H/D exchange rates in an acidic zeolite, Journal of Catalysis 351 (2017) 130-135.

[18] N. Pfriem, P. H. Hintermeier, S. Eckstein, S. Kim, Q. Liu, H. Shi, L. Milakovic, Y. Liu, G. L. Haller, E. Baráth, Y. Liu, and J. A. Lercher, Role of the ionic environment in enhancing the activity of reacting molecules in zeolite pores, Science 372 (2021) 952-957.

[19] R. Gounder and E. Iglesia, The catalytic diversity of zeolites: confinement and solvation effects within voids of molecular dimensions, Chemical Communications 49 (2013) 3491-3509.

[20] A. J. Jones, S. I. Zones, and E. Iglesia, Implications of transition state confinement within small voids for acid catalysis, The Journal of Physical Chemistry C 118 (2014) 17787-17800.

[21] A. J. Jones, R. T. Carr, S. I. Zones, and E. Iglesia, Acid strength and solvation in catalysis by MFI zeolites and effects of the identity, concentration and location of framework heteroatoms, Journal of Catalysis 312 (2014) 58-68.

[22] V. Frillette, W. Haag, and R. Lago, Catalysis by crystalline aluminosilicates: Characterization of intermediate pore-size zeolites by the “Constraint Index”, Journal of Catalysis 67 (1981) 218-222.

[23] T. Yokoi, H. Mochizuki, S. Namba, J. N. Kondo, and T. Tatsumi, Control of the Al distribution in the framework of ZSM-5 zeolite and its evaluation by solid-state NMR technique and catalytic properties, The Journal of Physical Chemistry C 119 (2015) 15303-15315.

[24] J. Dědeček, D. Kaucký, and B. Wichterlová, Al distribution in ZSM-5 zeolites: An experimental study, Chemical Communications(2001) 970-971.

[25] J. Dědeček, Z. Sobalík, and B. Wichterlová, Siting and distribution of framework aluminium atoms in silicon-rich zeolites and impact on catalysis, Catalysis Reviews 54 (2012) 135-223.

[26] C. Song, Y. Chu, M. Wang, H. Shi, L. Zhao, X. Guo, W. Yang, J. Shen, N. Xue, L. Peng, and W. Ding, Cooperativity of adjacent Brønsted acid sites in MFI zeolite channel leads to enhanced polarization and cracking of alkanes, Journal of Catalysis 349 (2017) 163-174.

[27] A. N. Mlinar, P. M. Zimmerman, F. E. Celik, M. Head-Gordon, and A. T. Bell, Effects of Brønsted-acid site proximity on the oligomerization of propene in H-MFI, Journal of Catalysis 288 (2012) 65-73.

[28] J. R. Di Iorio, C. T. Nimlos, and R. Gounder, Introducing catalytic diversity into single-site chabazite zeolites of fixed composition via synthetic control of active site proximity, ACS Catalysis 7 (2017) 6663-6674.

[29] E. Tabor, M. Bernauer, B. Wichterlová, and J. Dedecek, Enhancement of propene oligomerization and aromatization by proximate protons in zeolites; FTIR study of the reaction pathway in ZSM-5, Catalysis Science & Technology 9 (2019) 4262-4275.

[30] P. M. Kester, J. T. Crum, S. Li, W. F. Schneider, and R. Gounder, Effects of Brønsted acid site proximity in chabazite zeolites on OH infrared spectra and protolytic propane cracking kinetics, Journal of Catalysis 395 (2021) 210-226.

[31] G. W. Huber, S. Iborra, and A. Corma, Synthesis of transportation fuels from biomass: chemistry, catalysts, and engineering, Chemical Reviews 106 (2006) 4044-4098.

[32] D. E. Resasco, B. Wang, and S. Crossley, Zeolite-catalysed C–C bond forming reactions for biomass conversion to fuels and chemicals, Catalysis Science & Technology 6 (2016) 2543-2559.

[33] A. W. Beck, A. J. O'Brien, G. G. Zaimes, D. E. Resasco, S. P. Crossley, and V. Khanna, Systems-level analysis of energy and greenhouse gas emissions for coproducing biobased fuels and chemicals: implications for sustainability, ACS Sustainable Chemistry & Engineering 6 (2018) 5826-5834.

[34] G. G. Zaimes, A. W. Beck, R. R. Janupala, D. E. Resasco, S. P. Crossley, L. L. Lobban, and V. Khanna, Multistage torrefaction and in situ catalytic upgrading to hydrocarbon biofuels: analysis of life cycle energy use and greenhouse gas emissions, Energy & Environmental Science 10 (2017) 1034-1050.

[35] J. A. Herron, T. Vann, N. Duong, D. E. Resasco, S. Crossley, L. L. Lobban, and C. T. Maravelias, A systems-level roadmap for biomass thermal fractionation and catalytic upgrading strategies, Energy Technology 5 (2017) 130-150.

[36] A. Corma, M. JoséCliment, H. García, and J. Primo, Design of synthetic zeolites as catalysts in organic reactions: acylation of anisole by acyl chlorides or carboxylic acids over acid zeolites, Applied Catalysis 49 (1989) 109-123.

[37] M. Rueping and B. J. Nachtsheim, A review of new developments in the Friedel–Crafts alkylation – From green chemistry to asymmetric catalysis, Beilstein Journal of Organic Chemistry 6 (2010) 6.

[38] G. Sartori and R. Maggi, Use of Solid Catalysts in Friedel−Crafts Acylation Reactions, Chemical Reviews 106 (2006) 1077-1104.

[39] M. Bejblová, D. Procházková, and J. Čejka, Acylation Reactions over Zeolites and Mesoporous Catalysts, ChemSusChem 2 (2009) 486-499.

[40] P. Botella, A. Corma, J. M. López-Nieto, S. Valencia, and R. Jacquot, Acylation of Toluene with Acetic Anhydride over Beta Zeolites: Influence of Reaction Conditions and Physicochemical Properties of the Catalyst, Journal of Catalysis 195 (2000) 161-168.

[41] K. Shanmugapriya, M. Palanichamy, B. Arabindoo, and V. Murugesan, A novel route to produce thymol by vapor phase reaction of m-cresol with isopropyl acetate over Al-MCM-41 molecular sieves, Journal of Catalysis 224 (2004) 347-357.

[42] K. Shanmugapriya, M. Palanichamy, V. Balasubramanian, and V. Murugesan, Vapour phase reaction of m-cresol and ethyl acetate over MCM-41 molecular sieves: One-pot synthesis of coumarin derivatives, Microporous and Mesoporous Materials 95 (2006) 272-278.

[43] A. Gumidyala, B. Wang, and S. Crossley, Direct carbon-carbon coupling of furanics with acetic acid over Brønsted zeolites, Science Advances 2 (2016) e1601072.

[44] V. Sheemol, B. Tyagi, and R. V. Jasra, Acylation of toluene using rare earth cation exchanged zeolite β as solid acid catalyst, Journal of Molecular Catalysis A: Chemical 215 (2004) 201-208.

[45] Y. Ji, J. Pan, P. Dauenhauer, and R. J. Gorte, Probing direct carbon-carbon acylation of furans and long-chain acids over H-ZSM-5, Applied Catalysis A: General 577 (2019) 107-112.

[46] A. Gumidyala, T. Sooknoi, and S. Crossley, Selective ketonization of acetic acid over HZSM-5: The importance of acyl species and the influence of water, Journal of Catalysis 340 (2016) 76-84.

[47] T. N. Pham, T. Sooknoi, S. P. Crossley, and D. E. Resasco, Ketonization of carboxylic acids: mechanisms, catalysts, and implications for biomass conversion, ACS Catalysis 3 (2013) 2456-2473.

[48] C. Gauthier, B. Chiche, A. Finiels, and P. Geneste, Influence of acidity in Friedel-Crafts acylation catalyzed by zeolites, Journal of Molecular Catalysis 50 (1989) 219-229.

[49] O. Kresnawahjuesa, R. J. Gorte, and D. White, The acylation of propene by acetic acid over H-[Fe] ZSM-5 and H-[Al] ZSM-5, Journal of Molecular Catalysis A: Chemical 212 (2004) 309-314.

[50] A. Corma, H. Garcia, S. Iborra, and J. Primo, Modified faujasite zeolites as catalysts in organic reactions: Esterification of carboxylic acids in the presence of HY zeolites, Journal of Catalysis 120 (1989) 78-87.

[51] N. N. Duong, B. Wang, T. Sooknoi, S. P. Crossley, and D. E. Resasco, Enhancing the Acylation Activity of Acetic Acid by Formation of an Intermediate Aromatic Ester, ChemSusChem 10 (2017) 2823-2832.

[52] M. L. M. Bonati, R. W. Joyner, and M. Stockenhuber, On the mechanism of aromatic acylation over zeolites, Microporous and Mesoporous Materials 104 (2007) 217-224.

[53] C. L. Padró and C. R. Apesteguía, Acylation of phenol on solid acids: Study of the deactivation mechanism, Catalysis Today 107-108 (2005) 258-265.

[54] D. Rohan, C. Canaff, E. Fromentin, and M. Guisnet, Acetylation of anisole by acetic anhydride over a HBEA zeolite—Origin of deactivation of the catalyst, Journal of Catalysis 177 (1998) 296-305.

[55] A. Vogt, H. W. Kouwenhoven, and R. Prins, Fries rearrangement over zeolitic catalysts, Applied Catalysis A: General 123 (1995) 37-49.

[56] S. Schallmoser, T. Ikuno, M. Wagenhofer, R. Kolvenbach, G. Haller, M. Sanchez-Sanchez, and J. Lercher, Impact of the local environment of Brønsted acid sites in ZSM-5 on the catalytic activity in n-pentane cracking, Journal of Catalysis 316 (2014) 93-102.

[57] Y. Zhang, R. Zhao, M. Sanchez-Sanchez, G. L. Haller, J. Hu, R. Bermejo-Deval, Y. Liu, and J. A. Lercher, Promotion of protolytic pentane conversion on H-MFI zeolite by proximity of extra-framework aluminum oxide and Brønsted acid sites, Journal of Catalysis 370 (2019) 424-433.

[58] J. A. van Bokhoven, M. Tromp, D. Koningsberger, J. Miller, J. Pieterse, J. Lercher, B. Williams, and H. H. Kung, An explanation for the enhanced activity for light alkane conversion in mildly steam dealuminated mordenite: The dominant role of adsorption, Journal of Catalysis 202 (2001) 129-140.

[59] O. A. Abdelrahman, K. P. Vinter, L. Ren, D. Xu, R. J. Gorte, M. Tsapatsis, and P. J. Dauenhauer, Simple quantification of zeolite acid site density by reactive gas chromatography, Catalysis Science & Technology 7 (2017) 3831-3841.

[60] H. S. Fogler, *Elements of chemical reaction engineering*. Prentice Hall, 2016.

[61] J. Jae, G. A. Tompsett, A. J. Foster, K. D. Hammond, S. M. Auerbach, R. F. Lobo, and G. W. Huber, Investigation into the shape selectivity of zeolite catalysts for biomass conversion, Journal of Catalysis 279 (2011) 257-268.

[62] D. Olson, G. Kokotailo, S. Lawton, and W. Meier, Crystal structure and structure-related properties of ZSM-5, The Journal of Physical Chemistry 85 (1981) 2238-2243.

[63] J. Caro, M. Bülow, J. Kärger, and H. Pfeifer, The influence of chemisorbed molecules on mass transfer in H-ZSM-5-type zeolites and the location of Brønsted acid sites, Journal of Catalysis 114 (1988)

[64] M. Foster, I. Rivin, M. Treacy, and O. D. Friedrichs, A geometric solution to the largest-free-sphere problem in zeolite frameworks, Microporous and Mesoporous Materials 90 (2006) 32-38.

[65] M. L. Sarazen, E. Doskocil, and E. Iglesia, Catalysis on solid acids: Mechanism and catalyst descriptors in oligomerization reactions of light alkenes, Journal of Catalysis 344 (2016) 553-569.

[66] A. Hwang, D. Prieto-Centurion, and A. Bhan, Isotopic tracer studies of methanol-to-olefins conversion over HSAPO-34: The role of the olefins-based catalytic cycle, Journal of Catalysis 337 (2016) 52-56.

[67] A. Hwang, M. Kumar, J. D. Rimer, and A. Bhan, Implications of methanol disproportionation on catalyst lifetime for methanol-to-olefins conversion by HSSZ-13, Journal of Catalysis 346 (2017) 154-160.

[68] S. S. Arora, D. L. Nieskens, A. Malek, and A. Bhan, Lifetime improvement in methanol-to-olefins catalysis over chabazite materials by high-pressure H 2 co-feeds, Nature Catalysis 1 (2018) 666-672.

[69] U. Freese, F. Heinrich, and F. Roessner, Acylation of aromatic compounds on H-Beta zeolites, Catalysis Today 49 (1999) 237-244.

[70] S. Wang and E. Iglesia, Experimental and theoretical assessment of the mechanism and site requirements for ketonization of carboxylic acids on oxides, Journal of Catalysis 345 (2017) 183-206.

[71] Y. Zhao and B. Wojciechowski, The consequences of steam dilution in catalytic cracking: I. Effect of steam dilution on reaction rates and activation energy in 2-methylpentane cracking over USHY, Journal of Catalysis 163 (1996) 365-373.

[72] V. J. Margarit, M. Osman, S. Al-Khattaf, C. Martinez, M. Boronat, and A. Corma, Control of the reaction mechanism of alkylaromatics transalkylation by means of molecular confinement effects associated to zeolite channel architecture, ACS Catalysis 9 (2019) 5935-5946.

[73] S. Al-Khattaf, S. A. Ali, A. M. Aitani, N. Žilková, D. Kubička, and J. Čejka, Recent advances in reactions of alkylbenzenes over novel zeolites: the effects of zeolite structure and morphology, Catalysis Reviews 56 (2014) 333-402.

[74] J. M. Serra, E. Guillon, and A. Corma, A rational design of alkyl-aromatics dealkylation–transalkylation catalysts using C8 and C9 alkyl-aromatics as reactants, Journal of Catalysis 227 (2004) 459-469.

[75] S. Al-Khattaf and H. De Lasa, The role of diffusion in alkyl-benzenes catalytic cracking, Applied Catalysis A: General 226 (2002) 139-153.

[76] A. Corma and B. Wojciechowski, The catalytic cracking of cumene, Catalysis Reviews Science and Engineering 24 (1982) 1-65.

[77] A. Corma, J. Fierro, R. Montan, and F. Tomas, On the mechanism of cumene dealkylation: the interaction of cumene molecules on silica-alumina surfaces, Journal of Molecular Catalysis 30 (1985) 361-372.

[78] G. Li, B. Wang, B. Chen, and D. E. Resasco, Role of water in cyclopentanone self-condensation reaction catalyzed by MCM-41 functionalized with sulfonic acid groups, Journal of Catalysis 377 (2019) 245-254.

[79] A. J. Jones and E. Iglesia, The strength of Brønsted acid sites in microporous aluminosilicates, ACS Catalysis 5 (2015) 5741-5755.

[80] R. Gounder and E. Iglesia, Effects of partial confinement on the specificity of monomolecular alkane reactions for acid sites in side pockets of mordenite, Angewandte Chemie International Edition 49 (2010) 808-811.

[81] K. Chen, M. Abdolrahmani, S. Horstmeier, T. N. Pham, V. T. Nguyen, M. Zeets, B. Wang, S. Crossley, and J. L. White, Brønsted–Brønsted Synergies between Framework and Noncrystalline Protons in Zeolite H-ZSM-5, ACS Catalysis 9 (2019) 6124-6136.

[82] T. N. Pham, V. Nguyen, B. Wang, J. L. White, and S. Crossley, Quantifying the Influence of Water on the Mobility of Aluminum Species and Their Effects on Alkane Cracking in Zeolites, ACS Catalysis 11 (2021) 6982-6994.

[83] P. O. Fritz and J. H. Lunsford, The effect of sodium poisoning on dealuminated Y-type zeolites, Journal of Catalysis 118 (1989) 85-98.

[84] G. Li, B. Wang, T. Kobayashi, M. Pruski, and D. E. Resasco, Optimizing the surface distribution of acid sites for cooperative catalysis in condensation reactions promoted by water, Chem Catalysis 1 (2021) 1065-1087.

[85] Y. Liu, A. Vjunov, H. Shi, S. Eckstein, D. M. Camaioni, D. Mei, E. Baráth, and J. A. Lercher, Enhancing the catalytic activity of hydronium ions through constrained environments, Nature Communications 8 (2017) 14113.

[86] H. Shi, S. Eckstein, A. Vjunov, D. M. Camaioni, and J. A. Lercher, Tailoring nanoscopic confines to maximize catalytic activity of hydronium ions, Nature Communications 8 (2017) 15442.

[87] S. Eckstein, P. H. Hintermeier, M. V. Olarte, Y. Liu, E. Baráth, and J. A. Lercher, Elementary steps and reaction pathways in the aqueous phase alkylation of phenol with ethanol, Journal of Catalysis 352 (2017) 329-336.

[88] Y. Liu, E. Baráth, H. Shi, J. Hu, D. M. Camaioni, and J. A. Lercher, Solvent-determined mechanistic pathways in zeolite-H-BEA-catalysed phenol alkylation, Nature Catalysis 1 (2018) 141-147.

[89] H. K. Chau, D. E. Resasco, P. Do, and S. P. Crossley, Acylation of m-cresol with acetic acid supported by in-situ ester formation on H-ZSM-5 zeolites, Journal of Catalysis 406 (2022) 48-55.

[90] J. Dědeček, D. Kaucký, B. Wichterlová, and O. Gonsiorová, Co^{2+} ions as probes of Al distribution in the framework of zeolites. ZSM-5 study, Physical Chemistry Chemical Physics 4 (2002) 5406-5413.

[91] A. Janda and A. T. Bell, Effects of Si/Al ratio on the distribution of framework Al and on the rates of alkane monomolecular cracking and dehydrogenation in H-MFI, Journal of the American Chemical Society 135 (2013) 19193-19207.

[92] C. T. Nimlos, A. J. Hoffman, Y. G. Hur, B. J. Lee, J. R. Di Iorio, D. D. Hibbitts, and R. Gounder, Experimental and Theoretical Assessments of Aluminum Proximity in MFI Zeolites and Its Alteration by Organic and Inorganic Structure-Directing Agents, Chemistry of Materials 32 (2020) 9277-9298.

[93] L. H. Ong, M. Dömök, R. Olindo, A. C. van Veen, and J. A. Lercher, Dealumination of HZSM-5 via steam-treatment, Microporous and Mesoporous Materials 164 (2012) 9-20.

[94] X. Rozanska, L. Barbosa, and R. van Santen, A periodic density functional theory study of cumene formation catalyzed by H-Mordenite, The Journal of Physical Chemistry B 109 (2005) 2203-2211.

[95] B. Jansang, T. Nanok, and J. Limtrakul, Structures and reaction mechanisms of cumene formation via benzene alkylation with propylene in a newly synthesized ITQ-24 zeolite: an embedded ONIOM study, The Journal of Physical Chemistry B 110 (2006) 12626-12631.

[96] Z. Lei, L. Liu, and C. Dai, Insight into the reaction mechanism and charge transfer analysis for the alkylation of benzene with propylene over H-Beta zeolite, Molecular Catalysis 454 (2018) 1-11.

[97] A. D. Chowdhury, K. Houben, G. T. Whiting, S.-H. Chung, M. Baldus, and B. M. Weckhuysen, Electrophilic aromatic substitution over zeolites generates Wheland-type reaction intermediates, Nature Catalysis 1 (2018) 23-31.

[98] A. Ison and R. J. Gorte, The adsorption of methanol and water on H-ZSM-5, Journal of Catalysis 89 (1984) 150-158.

[99] N. Hansen, T. Kerber, J. Sauer, A. T. Bell, and F. J. Keil, Quantum chemical modeling of benzene ethylation over H-ZSM-5 approaching chemical accuracy: a hybrid MP2: DFT study, Journal of the American Chemical Society 132 (2010) 11525-11538.

[100] D. Mei and J. A. Lercher, Effects of Local Water Concentrations on Cyclohexanol Dehydration in H-BEA Zeolites, The Journal of Physical Chemistry C 123 (2019) 25255-25266.

[101] R. Gounder, A. J. Jones, R. T. Carr, and E. Iglesia, Solvation and acid strength effects on catalysis by faujasite zeolites, Journal of Catalysis 286 (2012) 214-223.

[102] T. G. Kofke and R. Gorte, A temperature-programmed desorption study of olefin oligomerization in H-ZSM-5, Journal of Catalysis 115 (1989) 233-243.

[103] M. Bernauer, E. Tabor, V. Pashkova, D. Kaucký, Z. Sobalík, B. Wichterlová, and J. Dedecek, Proton proximity–New key parameter controlling adsorption, desorption and activity in propene oligomerization over H-ZSM-5 zeolites, Journal of Catalysis 344 (2016) 157-172.

[104] Q. Wang, G. Giannetto, and M. Guisnet, Dealumination of zeolites III. Effect of extra-framework aluminum species on the activity, selectivity, and stability of Y zeolites in n-heptane cracking, Journal of Catalysis 130 (1991) 471-482.

[105] J. Čejka, A. Vondrová, B. Wichterlová, H. G. Jerschkewitz, G. Lischke, and E. Schreier, The effect of extra-framework aluminum in dealuminated ZSM-5 zeolites on the transformation of aromatic hydrocarbons, Collection of Czechoslovak Chemical Communications 60 (1995) 412-420.

[106] B. Wichterlová, N. Žilkova, E. Uvarova, J. Čejka, P. Sarv, C. Paganini, and J. A. Lercher, Effect of Brønsted and Lewis sites in ferrierites on skeletal isomerization of n-butenes, Applied Catalysis A: General 182 (1999) 297-308.

[107] V. Mavrodinova, M. Popova, R. Mihályi, G. Pál-Borbély, and C. Minchev, Transalkylation of toluene with cumene over zeolites Y dealuminated in solid-state: Part II. Effect of the introduced Lewis acid sites, Applied Catalysis A: General 248 (2003) 197-209.

[108] M. Grady and R. J. Gorte, Adsorption of 2-propanol and propene on H-ZSM-5: Evidence for stable carbenium ion formation, The Journal of Physical Chemistry 89 (1985) 1305-1308.

[109] Y. Zhi, H. Shi, L. Mu, Y. Liu, D. Mei, D. M. Camaioni, and J. A. Lercher, Dehydration Pathways of 1-Propanol on HZSM-5 in the Presence and Absence of Water, Journal of the American Chemical Society 137 (2015) 15781-15794.

[110] J. Macht, M. J. Janik, M. Neurock, and E. Iglesia, Mechanistic consequences of composition in acid catalysis by polyoxometalate keggin clusters, Journal of the American Chemical Society 130 (2008) 10369-10379.

[111] M. Niaounakis, *Recycling of flexible plastic packaging*. William Andrew, 2019.

[112] Plastic upcycling, Nature Catalysis 2 (2019) 945-946.

[113] L. T. Korley, T. H. Epps, B. A. Helms, and A. J. Ryan, Toward polymer upcycling—adding value and tackling circularity, Science 373 (2021) 66-69.

[114] A. J. Martín, C. Mondelli, S. D. Jaydev, and J. Pérez-Ramírez, Catalytic processing of plastic waste on the rise, Chem 7 (2021) 1487-1533.

[115] L. D. Ellis, N. A. Rorrer, K. P. Sullivan, M. Otto, J. E. McGeehan, Y. Román-Leshkov, N. Wierckx, and G. T. Beckham, Chemical and biological catalysis for plastics recycling and upcycling, Nature Catalysis 4 (2021) 539-556.

[116] I. Vollmer, M. J. Jenks, M. C. Roelands, R. J. White, T. van Harmelen, P. de Wild, G. P. van Der Laan, F. Meirer, J. T. Keurentjes, and B. M. Weckhuysen, Beyond mechanical recycling: Giving new life to plastic waste, Angewandte Chemie International Edition 59 (2020) 15402-15423.

[117] P. S. Roy, G. Garnier, F. Allais, and K. Saito, Strategic approach towards plastic waste valorization: challenges and promising chemical upcycling possibilities, ChemSusChem 14 (2021) 4007-4027.

[118] H. Chen, K. Wan, Y. Zhang, and Y. Wang, Waste to Wealth: Chemical Recycling and Chemical Upcycling of Waste Plastics for a Great Future, ChemSusChem 14 (2021) 1-15.

[119] Q. Hou, M. Zhen, H. Qian, Y. Nie, X. Bai, T. Xia, M. L. U. Rehman, Q. Li, and M. Ju, Upcycling and catalytic degradation of plastic wastes, Cell Reports Physical Science 2 (2021) 100514.

[120] X. Chen, Y. Wang, and L. Zhang, Recent progress in the chemical upcycling of plastic wastes, ChemSusChem 14 (2021) 4137-4151.

[121] O. Horodytska, F. J. Valdés, and A. Fullana, Plastic flexible films waste management–A state of art review, Waste Management 77 (2018) 413-425.

[122] J. M. Garcia and M. L. Robertson, The future of plastics recycling, Science 358 (2017) 870-872.

[123] K. L. Sánchez-Rivera, P. Zhou, M. S. Kim, L. D. González Chávez, S. Grey, K. Nelson, S. C. Wang, I. Hermans, V. M. Zavala, R. C. Van Lehn, and G. W. Huber, Reducing Antisolvent Use in the STRAP Process by Enabling a Temperature-Controlled Polymer Dissolution and Precipitation for the Recycling of Multilayer Plastic Films, ChemSusChem 14 (2021) 4317-4329.

[124] T. W. Walker, N. Frelka, Z. Shen, A. K. Chew, J. Banick, S. Grey, M. S. Kim, J. A. Dumesic, R. C. Van Lehn, and G. W. Huber, Recycling of multilayer plastic packaging materials by solvent-targeted recovery and precipitation, Science Advances 6 (2020) eaba7599.

[125] D. M. Alonso, S. G. Wettstein, and J. A. Dumesic, Gamma-valerolactone, a sustainable platform molecule derived from lignocellulosic biomass, Green Chemistry 15 (2013) 584-595.

[126] A. Corma, Inorganic solid acids and their use in acid-catalyzed hydrocarbon reactions, Chemical Reviews 95 (1995) 559-614.

[127] F. Chen, M. Shetty, M. Wang, H. Shi, Y. Liu, D. M. Camaioni, O. Y. Gutiérrez, and J. A. Lercher, Differences in Mechanism and Rate of Zeolite-Catalyzed Cyclohexanol Dehydration in Apolar and Aqueous Phase, ACS Catalysis 11 (2021) 2879-2888.

[128] J. F. DeWilde, H. Chiang, D. A. Hickman, C. R. Ho, and A. Bhan, Kinetics and mechanism of ethanol dehydration on γ-Al2O3: the critical role of dimer inhibition, ACS Catalysis 3 (2013) 798-807.

[129] O. A. Abdelrahman, D. S. Park, K. P. Vinter, C. S. Spanjers, L. Ren, H. J. Cho, K. Zhang, W. Fan, M. Tsapatsis, and P. J. Dauenhauer, Renewable isoprene by sequential hydrogenation of itaconic acid and dehydra-decyclization of 3-methyl-tetrahydrofuran, ACS Catalysis 7 (2017) 1428-1431.

[130] O. A. Abdelrahman, D. S. Park, K. P. Vinter, C. S. Spanjers, L. Ren, H. J. Cho, D. G. Vlachos, W. Fan, M. Tsapatsis, and P. J. Dauenhauer, Biomass-derived butadiene by dehydra-decyclization of tetrahydrofuran, ACS Sustainable Chemistry & Engineering 5 (2017) 3732-3736.

[131] S. Li, O. A. Abdelrahman, G. Kumar, M. Tsapatsis, D. G. Vlachos, S. Caratzoulas, and P. J. Dauenhauer, Dehydra-decyclization of tetrahydrofuran on H-ZSM5: mechanisms, pathways, and transition state entropy, ACS Catalysis 9 (2019) 10279-10293.

[132] G. Kumar, D. Liu, D. Xu, L. Ren, M. Tsapatsis, and P. J. Dauenhauer, Dehydra-decyclization of 2-methyltetrahydrofuran to pentadienes on boron-containing zeolites, Green Chemistry 22 (2020) 4147-4160.

[133] M. D. Kumbhalkar, J. S. Buchanan, G. W. Huber, and J. A. Dumesic, Ring opening of biomass-derived cyclic ethers to dienes over silica/alumina, ACS Catalysis 7 (2017) 5248-5256.

[134] J. Q. Bond, D. Martin Alonso, R. M. West, and J. A. Dumesic, γ-Valerolactone ring-opening and decarboxylation over SiO2/Al2O3 in the presence of water, Langmuir 26 (2010) 16291-16298.

[135] J. Q. Bond, C. S. Jungong, and A. Chatzidimitriou, Microkinetic analysis of ring opening and decarboxylation of γ-valerolactone over silica alumina, Journal of Catalysis 344 (2016) 640-656.

[136] S. Gupta, R. Arora, N. Sinha, M. I. Alam, and M. A. Haider, Mechanistic insights into the ring-opening of biomass derived lactones, RSC Advances 6 (2016) 12932-12942.

[137] M. John, K. Alexopoulos, M.-F. Reyniers, and G. B. Marin, Reaction path analysis for 1-butanol dehydration in H-ZSM-5 zeolite: Ab initio and microkinetic modeling, Journal of Catalysis 330 (2015) 28-45.

[138] F. Eder, Y. He, G. Nivarthy, and J. A. Lercher, Sorption of alkanes on novel pillared zeolites; comparison between MCM-22 and MCM-36, Recueil des Travaux Chimiques des Pays-Bas 115 (1996) 531-535.

[139] F. Eder and J. A. Lercher, Alkane sorption in molecular sieves: The contribution of ordering, intermolecular interactions, and sorption on Brønsted acid sites, Zeolites 18 (1997) 75-81.

[140] B. A. De Moor, M.-F. o. Reyniers, O. C. Gobin, J. A. Lercher, and G. B. Marin, Adsorption of C2− C8 n-Alkanes in Zeolites, The Journal of Physical Chemistry C 115 (2011) 1204-1219.

[141] U. H. Hossain, T. Seidl, and W. Ensinger, Combined in situ infrared and mass spectrometric analysis of high-energy heavy ion induced degradation of polyvinyl polymers, Polymer Chemistry 5 (2014) 1001-1012.

[142] B. Holland and J. Hay, The thermal degradation of poly (vinyl alcohol), Polymer 42 (2001) 6775-6783.

[143] P. Thomas, J.-P. Guerbois, G. Russell, and B. Briscoe, FTIR study of the thermal degradation of poly (vinyl alcohol), Journal of Thermal Analysis and Calorimetry 64 (2001) 501-508.

[144] G. Kresse and J. Furthmüller, Efficient iterative schemes for ab initio total-energy calculations using a plane-wave basis set, Physical Review B 54 (1996) 11169.

[145] P. E. Blöchl, Projector augmented-wave method, Physical Review B 50 (1994) 17953.

[146] G. Kresse and D. Joubert, From ultrasoft pseudopotentials to the projector augmented-wave method, Physical Review B 59 (1999) 1758.

[147] J. P. Perdew, K. Burke, and M. Ernzerhof, Generalized gradient approximation made simple, Physical Review Letters 77 (1996) 3865.

[148] S. Grimme, J. Antony, S. Ehrlich, and H. Krieg, A consistent and accurate ab initio parametrization of density functional dispersion correction (DFT-D) for the 94 elements H-Pu, The Journal of Chemical Physics 132 (2010) 154104.

[149] P. J. Dauenhauer and O. A. Abdelrahman, A universal descriptor for the entropy of adsorbed molecules in confined spaces, ACS Central Science 4 (2018) 1235-1243.

[150] B. A. De Moor, A. Ghysels, M.-F. Reyniers, V. Van Speybroeck, M. Waroquier, and G. B. Marin, Normal mode analysis in zeolites: toward an efficient calculation of adsorption entropies, Journal of Chemical Theory and Computation 7 (2011) 1090-1101.

[151] C. J. Cramer, "Computational Chemistry: Theories and Models," ed: John Wiley & Sons, Chichester, England, 2004.

[152] H. v. van Koningsveld, High-temperature (350 K) orthorhombic framework structure of zeolite H-ZSM-5, Acta Crystallographica Section B: Structural Science 46 (1990) 731-735.

[153] K. Chen, S. Horstmeier, V. T. Nguyen, B. Wang, S. P. Crossley, T. Pham, Z. Gan, I. Hung, and J. L. White, Structure and catalytic characterization of a second framework Al (IV) site in zeolite catalysts revealed by NMR at 35.2 T, Journal of the American Chemical Society 142 (2020) 7514-7523.

Appendix A1: Supporting information for Chapter 2

S1. Catalyst characterization

Table 7. BET surface area of zeolite catalysts

Catalysts	BET surface area (m^2/g)
MFI-40	449 [(a)]
Na-MFI-40	413 ± 7
MFI-140	428 ± 6
Na-MFI-140	415 ± 7

[(a)] value obtained from literature [154]

The BET surface areas drop about 3% and 8% by comparing parent MFI-40 with Na-MFI-40 and MFI-140 with Na-MFI-140 respectively, indicating that the chance of pore blockage after the sodium exchange is minimized.

Table 8. Coke content on the spent MFI-140 catalysts after 130 minutes reaction time on stream with varying $P_{acetic\ acid}$ and keeping $P_{m\text{-}cresol}$ at 0.3 kPa, $T_{reaction}$ = 250°C

	Coke, wt.%
$P_{acetic\ acid}$ = 1.4 kPa	1.7
$P_{acetic\ acid}$ = 2.8 kPa	2.4
$P_{acetic\ acid}$ = 4.1 kPa	1.9

Table 8 shows that the coke content on the spent catalyst measured by TGA-TPO analysis increases when the partial pressure of acetic acid increases from 1.4 kPa to 2.8 kPa, which is attributed to subsequent esterification of acylated product with acetic acid to form coke precursors. Then, the decrease of coke content on the spent catalyst at the partial pressure of acetic acid of 4.1 kPa could be due to pore blockage under these reaction conditions, which reduces the possibility of coke formation inside zeolite pores. It is acknowledged that the turnover number of the reaction at 130 minutes time on stream decreases with the partial pressure of acetic acid. Therefore, the partial pressure of the acylated product at 130 minutes reaction time on stream is lower at a higher partial pressure of acetic acid, leading to reduced coke content on the spent catalyst at the partial pressure of acetic acid of 4.1 kPa.

S2. Diffusion test by titration method

The role of diffusion in the vapor phase acylation of guaiacol with acetic acid over microporous zeolites has been emphasized as a rate-limiting factor in a recent study [155]. Xu et al. studied anisole acylation with acetic anhydride over Beta zeolites with different Brønsted acid site densities [156], where they also observed the dependence of reaction rate on acid site density. In general, when operating at high site densities and bulky reactants, this reaction is highly

susceptible to diffusion corruptions to measured reaction rates, which can cloud investigations into the reaction mechanism.

It should be noted that the potential influence of diffusion on reaction rate is dependent not only on acid site density, but also the crystallite size. The crystallite sizes of MFI-40 and MFI-140 have been reported to be 0.2-0.5 μm and 0.4-2 μm respectively, which indicate a shorter diffusion path length of MFI-40 compared to MFI-140 [157, 158]. Regarding the local confining environment surrounding the acid sites, it should be noted that changes to acid strength indicated by deprotonation energy (DPE) do not strongly depend on framework structure and proton location, but rather changes in intrinsic activity are commonly ascribed to the local environment around acid sites [159, 160]. It has been reported that Brønsted acid sites in MFI-40 and MFI-140 are mainly located at channel intersections and can be considered to have similar deprotonation energy and intrinsic reactivity consequently [21, 56, 79].

S3. Derivation of initial rates of the acylation of m-cresol with acetic acid over MFI-140 zeolite

Denotations:

K_1	equilibrium constant of m-Tolyl acetate formation
K_2	adsorption equilibrium constant of m-Tolyl acetate
K_3	adsorption equilibrium constant of m-cresol
K_4	adsorption equilibrium constant of acetic acid
K_5	adsorption equilibrium constant of water
K_6	equilibrium constant of acylium ion formation step on the catalyst surface
K_7	equilibrium constant of C-C coupling step on the catalyst surface
K_8^{-1}	desorption equilibrium constant of 2-hydroxy-4-methylacetophenone
k_6	rate constant of the acylium ion formation step
k_7	rate constant of the C-C coupling step
mC	m-cresol
AC	acetic acid
E	m-Tolyl acetate
AC^+	acylium ion
ACP	2-hydroxy-4-methylacetophenone
$[H^+]_0$	total number of Brønsted acid sites
*	vacant Brønsted acid sites

S3.1. Acylium ion formation from m-Tolyl acetate is the rate-limiting step. C-C coupling step follows Eley-Rideal reaction model.

Proposed elementary steps:

1) $mC + AC \rightleftarrows E + H_2O$ Formation of m-Tolyl acetate
2) $E + * \rightleftarrows E*$ Adsorption of m-Tolyl acetate
3) $mC + * \rightleftarrows mC*$ Adsorption of m-cresol
4) $AC + * \rightleftarrows AC*$ Adsorption of acetic acid
5) $H_2O + * \rightleftarrows H_2O*$ Adsorption of water
6) $E* \rightarrow AC^+ * + mC$ Formation of acylium ion from m-Tolyl acetate
7) $mC + AC^+ * \rightleftarrows ACP*$ Formation of acylated product via C-C coupling
8) $ACP* \rightleftarrows ACP + *$ Desorption of 2-hydroxy-4-methylacetophenone

The acylation rate expression can be derived as:

$$\frac{r}{[H^+]_0} = k_6[E^*] = \frac{k_6 K_1 K_2 P_{mC} P_{AC}/P_{H_2O}}{1 + \frac{K_1 K_2 P_{mC} P_{AC}}{P_{H_2O}} + K_3 P_{mC} + K_4 P_{AC} + K_5 P_{H_2O} + \frac{K_8 P_{ACP}}{K_7 P_{mC}} + K_8 P_{ACP}}$$

In this reaction mechanism, adsorbed m-Tolyl acetate is assumed to be the most abundant surface intermediate (MASI). All elementary steps, except the rate limiting step, are at quasi-equilibrium. Therefore, the initial acylation rate equation can be simplified as:

$$\frac{r_{initial}}{[H^+]_0} = \frac{k_6 K_1 K_2 P_{mC} P_{AC}/P_{H_2O}}{1 + \frac{K_1 K_2 P_{mC} P_{AC}}{P_{H_2O}}}$$

At low surface coverage of active intermediate m-Tolyl acetate:

$$\frac{r_{initial}}{[H^+]_0} = k_6 K_1 K_2 P_{mC} P_{AC}/P_{H_2O}$$

At high surface coverage of active intermediate m-Tolyl acetate: $r_{initial} = C_t k_6$

S3.2. C-C coupling is the rate-limiting step. C-C coupling step follows Eley-Rideal reaction model.

Proposed elementary steps:

1) $mC + AC \rightleftarrows E + H_2O$ Formation of m-Tolyl acetate
2) $E + * \rightleftarrows E*$ Adsorption of m-Tolyl acetate
3) $mC + * \rightleftarrows mC*$ Adsorption of m-cresol
4) $AC + * \rightleftarrows AC*$ Adsorption of acetic acid
5) $H_2O + * \rightleftarrows H_2O*$ Adsorption of water
6) $E* \rightleftarrows AC^+ * + mC$ Formation of acylium ion from m-Tolyl acetate
7) $mC + AC^+ * \rightarrow ACP*$ Formation of acylated product via C-C coupling
8) $ACP* \rightleftarrows ACP + *$ Desorption of 2-hydroxy-4-methylacetophenone

The acylation rate expression can be derived as:

$$\frac{r_{initial}}{[H^+]_0} = k_7 P_{mC}[AC^{+*}]$$

$$= \frac{k_7 K_1 K_2 K_6 P_{mC} P_{AC}/P_{H_2O}}{1 + \frac{K_1 K_2 P_{mC} P_{AC}}{P_{H_2O}} + K_3 P_{mC} + K_4 P_{AC} + K_5 P_{H_2O} + \frac{K_1 K_2 K_6 P_{AC}}{P_{H_2O}} + K_8 P_{ACP}}$$

In this reaction mechanism, surface acyl species is assumed to be the most abundant surface intermediate (MASI). All elementary steps, except the rate limiting step, are at quasi-equilibrium. Therefore, the initial acylation rate equation can be simplified as:

$$\frac{r_{initial}}{[H^+]_0} = \frac{k_7 K_1 K_2 K_6 P_{mC} P_{AC}/P_{H_2O}}{1 + \frac{K_1 K_2 K_6 P_{AC}}{P_{H_2O}}}$$

At low surface coverage of surface acyl species: $\frac{r_{initial}}{[H^+]_0} = k_7 K_1 K_2 K_6 P_{mC} P_{AC}/P_{H_2O}$

At high surface coverage of surface acyl species: $\frac{r_{initial}}{[H^+]_0} = k_7 P_{mC}$

References

[21] A. J. Jones, R. T. Carr, S. I. Zones, and E. Iglesia, Acid strength and solvation in catalysis by MFI zeolites and effects of the identity, concentration and location of framework heteroatoms, Journal of Catalysis 312 (2014) 58-68.

[56] S. Schallmoser, T. Ikuno, M. Wagenhofer, R. Kolvenbach, G. Haller, M. Sanchez-Sanchez, and J. Lercher, Impact of the local environment of Brønsted acid sites in ZSM-5 on the catalytic activity in n-pentane cracking, Journal of Catalysis 316 (2014) 93-102.

[79] A. J. Jones and E. Iglesia, The strength of Brønsted acid sites in microporous aluminosilicates, ACS Catalysis 5 (2015) 5741-5755.

[154] F. Thibault-Starzyk, I. Stan, S. Abelló, A. Bonilla, K. Thomas, C. Fernandez, J.-P. Gilson, and J. Pérez-Ramírez, Quantification of enhanced acid site accessibility in hierarchical zeolites–the accessibility index, Journal of Catalysis 264 (2009) 11-14.

[155] S. Gutiérrez-Rubio, M. Shamzhy, J. Čejka, D. Serrano, I. Moreno, and J. Coronado, Vapor phase acylation of guaiacol with acetic acid over micro, nano and hierarchical MFI and BEA zeolites, Applied Catalysis B: Environmental 285 (2021) 119826.

[156] H. Wei, K. Liu, S. Xie, W. Xin, X. Li, S. Liu, and L. Xu, Determination of different acid sites in Beta zeolite for anisole acylation with acetic anhydride, Journal of Catalysis 307 (2013) 103-110.

[157] J. Van Aelst, A. Philippaerts, E. Bartholomeeusen, E. Fayad, F. Thibault-Starzyk, J. Lu, D. Schryvers, R. Ooms, D. Verboekend, and P. Jacobs, Towards biolubricant compatible vegetable oils by pore mouth hydrogenation with shape-selective Pt/ZSM-5 catalysts, Catalysis Science & Technology 6 (2016) 2820-2828.

[158] D. Rojo-Gama, M. Nielsen, D. S. Wragg, M. Dyballa, J. Holzinger, H. Falsig, L. F. Lundegaard, P. Beato, R. Y. Brogaard, and K. P. Lillerud, A straightforward descriptor for the deactivation of zeolite catalyst H-ZSM-5, ACS Catalysis 7 (2017) 8235-8246.

[159] R. J. Gorte and S. P. Crossley, A perspective on catalysis in solid acids, Journal of Catalysis 375 (2019)

[160] S. P. Crossley, D. E. Resasco, and G. L. Haller, Clarifying the Multiple Roles of Confinement in Zeolites: From stabilization of transition states to modification of internal diffusion rates, Journal of Catalysis 372 (2019) 382-387.

Appendix A2: Acylation of m-cresol with acetic acid: effect of zeolite framework and water

1. Materials and methods

ZSM-5 zeolites with different Si/Al ratios (CBV-8014 with Si/Al = 40, CBV-28014 with Si/Al = 140) and BEA zeolite (CP814C with Si/Al = 19) were purchased in the ammonium form from Zeolyst International. Beta zeolite (Si/Al = 133) was obtained in proton-form H-Beta from Alfa Aesar. ZSM-22 (TON, Si/Al = 32.5 – 40) was purchased in proton-form from ACS Material.

Catalyst samples in ammonium form were calcined in flowing dry air at 600°C for 5 h with a heating rate of 2°C/min to obtain the proton-form zeolites. Protonated zeolites were then pelletized, crushed, and sieved to particles with sizes ranging from 90 to 250 μm. H-ZSM-5 zeolites with Si/Al = 40 and Si/Al = 140 are denoted as MFI-40 and MFI-140, respectively. H-Beta zeolite (Si/Al = 133) is denoted as BEA-133.

Temperature-programmed desorption (TPD) of isopropylamine (IPA) was carried out to determine the Brønsted acid site densities of the catalysts. Vapor phase flow reactions between m-cresol and acetic acid over different zeolites were conducted in a quartz tube reactor (1/4″ OD) at atmospheric pressure. The details of these methods are described in Chapter 2.

2. Effect of zeolite frameworks

The effect of zeolite framework and Si/Al ratio on acylation rate was investigated. By comparing turnover frequencies of acylation reactions over MFI-140 and BEA-133 as shown in Fig. 46, it shows that MFI-140 exhibits a higher turnover frequency compared to BEA-133. This result implies that confinement effect plays an important role in this acylation reaction. It is also worth mentioning that reactions over MFI-40 and BEA-19 (BAS density = 0.562 mmol/g) with high acid site density are likely limited by internal mass transfer. In addition, ZSM-22 (BAS

density = 0.384 mmol/g) shows a very low reactivity in Fig. 46, which is attributed to the pore mouth blocking in 1-D pore channels by carbonaceous deposits.

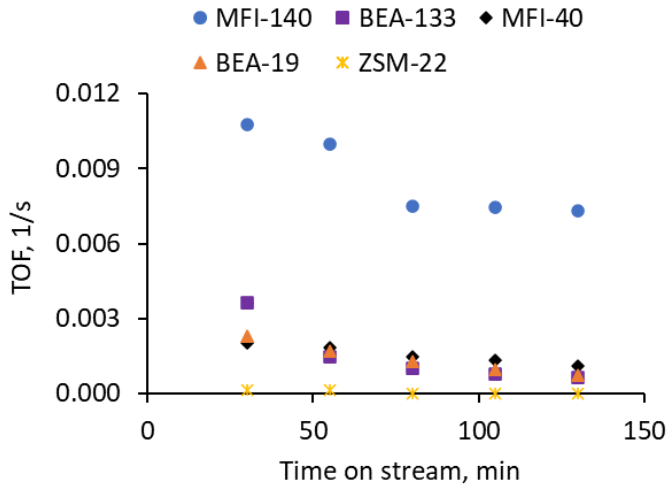

Fig. 46. Rate of 2-hydroxyl-4-methylacetophenone formation over different zeolites at 250°C, $P_{m\text{-}cresol}$ = 0.3 kPa, $P_{acetic\ acid}$ = 1.4 kPa

3. Effect of water

The effect of water on acylation reaction is a very intriguing part using BEA-133 to avoid the influence of internal mass transfer limitation. As shown in Fig. 47, reaction of m-cresol with m-tolyl acetate shows a higher rate than reaction with acetic acid, which is consistent with our previous results as m-tolyl acetate is a more effective acylating agent compared to acetic acid.

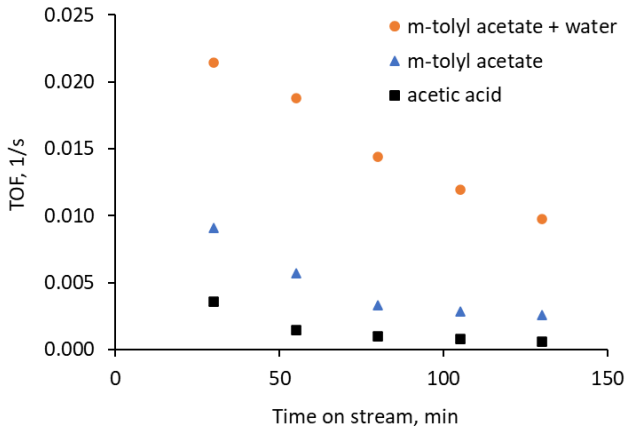

Fig. 47. Rate of 2-hydroxyl-4-methylacetophenone formation in reactions of m-cresol with acetic acid (■), m-tolyl acetate (▲), m-tolyl acetate + water (●) over BEA-133 at 250°C, $P_{m\text{-}cresol}$ = 0.3 kPa, $P_{acylating\ agent}$ = 1.4 kPa, P_{water} = 0 – 0.9 kPa

Interestingly, co-feeding water still helps enhance the acylation rate. This result suggests that water plays an important kinetic role in this reaction. The kinetic effect of water on acylation of m-cresol with acetic acid was revealed by separated runs and intermittent water co-feeding as shown in Fig. 48a and Fig. 48b.

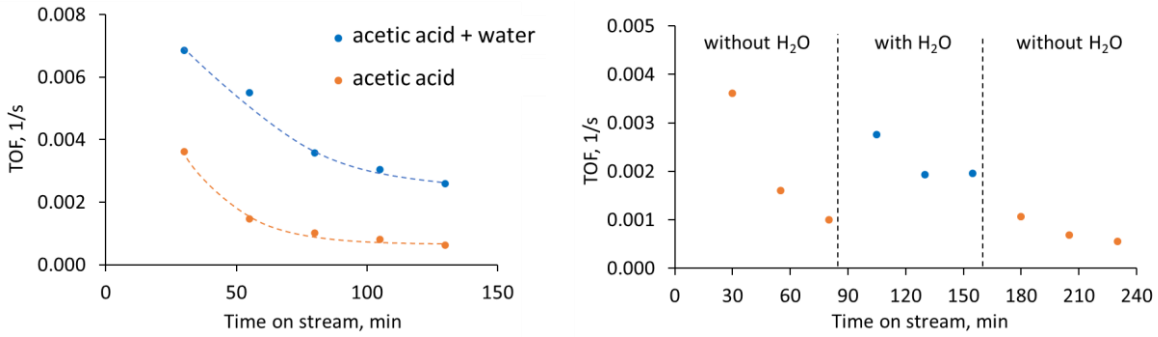

a) **b)**

Fig. 48. Effect of water co-feeding on m-cresol acylation with acetic acid over BEA-133 at 250°C, $P_{m\text{-}cresol}$ = 0.3 kPa, $P_{acetic\ acid}$ = 1.4 kPa, P_{water} = 0 – 0.9 kPa

It clearly shows that water reversibly enhances acylation of m-cresol with acetic acid over BEA-133 which is likely not limited by internal diffusion. One possibility is that water helps clean

active sites by hydrolyzing esterification products or inhibiting the subsequent reactions of acylated product. However, by extrapolating to 0-minute TOS to decouple the influence of deactivation, the turnover frequency of reaction in the presence of water is still higher than the reaction in the absence of water. It is speculated that water may enthalpically stabilize the transition state of this reaction, leading to higher rates in the presence of water.

Appendix A3: Supporting information for Chapter 3

S1. Derivation of cumene dealkylation rate by transition state theory

The reaction rate of cumene dealkylation can be derived based on Langmuir-Hinshelwood mechanism as follows:

$$TOF = \frac{Rate}{[H^+]} = k_{TST}\theta_{cumene} = \frac{k_{TST}K_{cumene}P_{cumene}}{1 + K_{cumene}P_{cumene}}$$

Because the reaction is not zero-order with respect to partial pressure of cumene, the major fraction of Brønsted acid sites is vacant sites. Therefore, reaction rate can be simplified as follows:

$$TOF = k_{TST}K_{cumene}P_{cumene}^{n}$$

Rate constant is obtained from transition state theory:

$$k_{TST} = \frac{k_B T}{h} e^{-\Delta G_0^{\ddagger}/RT} = \frac{k_B T}{h} e^{\frac{\Delta S^{\ddagger}}{R}} e^{\frac{-\Delta H^{\ddagger}}{RT}}$$

Adsorption constant is calculated by Van't Hoff equation:

$$lnK_{Cumene} = -\frac{\Delta H_{cumene}}{RT} + \frac{\Delta S_{cumene}}{R}$$

As a result, the Eyring–Polanyi equation for the reaction rate of cumene dealkylation can be described as follows:

$$TOF = \frac{k_B T}{h} e^{\frac{\Delta S_{app}^{\ddagger}}{R}} e^{\frac{-\Delta H_{app}^{\ddagger}}{RT}} P_{cumene}^{n}$$

where $\Delta S_{app}^{\ddagger}$ is apparent activation entropy and $\Delta H_{app}^{\ddagger}$ is apparent activation enthalpy

S2. Catalyst deactivation during cumene dealkylation

Silanol defects are present at significant amount in low Si/Al zeolites such as MFI-11.5 and AHFS-MFI-11.5 catalysts. Beato et al. reported that catalyst deactivation during conversion of methanol to hydrocarbons is attributed to the presence of silanol defects [161]. However, the concentrations of silanol defects in MFI-11.5 and AHFS-MFI-11.5 catalysts are comparable as shown in FT-IR spectra in Fig. 9, yet the deactivation behaviors of these two catalysts are markedly different as shown in Fig. 22. Therefore, these results show that the deactivation of H-ZSM-5 zeolites in cumene dealkylation is strongly influenced by the presence of extra-framework aluminum species.

The influence of reaction temperature on catalyst deactivation in cumene dealkylation over different H-ZSM-5 zeolites is shown in Fig. 24-26. Interestingly, catalysts become more stable at higher temperature up to 300°C, even though the reaction rate and amount of propylene increase with temperature. This trend of catalyst stability versus reaction temperature is also generally consistent in the presence and absence of water co-feeding. It was found that at temperature lower than 500 K, oligomerization of olefins is dominant, oligomerization products adsorb strongly on active sites, and reaction is likely to be limited by slow diffusion of product molecules [162]. However, as reaction temperature increases above 500 K, cracking reactions of oligomers become significant and internal mass transport of product molecules is much faster, leading to shorter residence time of heavy molecules inside zeolite pores [162]. Lobo et al. also reported that oligomerization of butene on H-Beta zeolite is limited by diffusion of oligomers out of zeolite crystals, while Peratello et al. claimed that internal diffusion is the rate determining step in propylene oligomerization over amorphous mesoporous silica-alumina with a low activation energy of 18 kJ/mol [163, 164]. The important role of intracrystalline mass transfer along with

Brønsted acid site density in light olefin oligomerization over H-ZSM-5 zeolites with different meso-porosity and crystallite size was also emphasized by Corma et al. in the previous study [165]. In fact, the longer the residence time of oligomers and the bulkier the oligomerization products, the faster coke formation and catalyst deactivation.

The temperature dependence of oligomerization, cracking reactions, and mass transfer in zeolites could all play the role in the higher stability of zeolites in cumene dealkylation at high reaction temperature. In addition, these interesting effects of water, extra-framework aluminum species, and reaction temperature on catalyst stability during cumene dealkylation can be applied in reactions in which catalysts deactivation caused by olefin oligomerization.

References

[161] K. Barbera, F. Bonino, S. Bordiga, T. V. Janssens, and P. Beato, Structure–deactivation relationship for ZSM-5 catalysts governed by framework defects, Journal of Catalysis 280 (2011) 196-205.

[162] J. Van den Berg, J. Wolthuizen, and J. Van Hooff, Reaction of small olefins on zeolite H-ZSM-5. A thermogravimetric study at low and intermediate temperatures, Journal of Catalysis 80 (1983) 139-144.

[163] M. J. Wulfers and R. F. Lobo, Assessment of mass transfer limitations in oligomerization of butene at high pressure on H-Beta, Applied Catalysis A: General 505 (2015) 394-401.

[164] S. Peratello, M. Molinari, G. Bellussi, and C. Perego, Olefins oligomerization: thermodynamics and kinetics over a mesoporous silica–alumina, Catalysis Today 52 (1999) 271-277.

[165] A. Corma, C. Martínez, and E. Doskocil, Designing MFI-based catalysts with improved catalyst life for $C_3^=$ and $C_5^=$ oligomerization to high-quality liquid fuels, Journal of Catalysis 300 (2013) 183-196.

Appendix A4: Supporting information for Chapter 4

S1. Statistical Thermodynamics Calculation

The entropy loss of a gaseous molecule adsorbing over the BAS is calculated as follows [149]:

$$\Delta S_{ads} = S_{1D,trans} + \left\{ F_{rot,slab} + \frac{1}{7}\left[\left(1 - \frac{V_{cri}}{2V_{occ}} \right)^{-3} - 1 \right] \right\} S_{rot}$$

where:

$F_{rot,slab} = 0.03$ is the loss factor of rotational degrees of freedom corrected from the slab

$V_{\mathrm{occ}} = 177.4$ (A^3) is the averaged occupiable volume of the MFI zeolite pores

V_{cri} is the critical volume which eliminates all rotation degrees of freedom of the adsorbate.

In this work, we approximated this parameter to the volume of the smallest cylinder outfitting with the adsorbate.

$S_{1D,trans}$ and S_{rot} are, respectively, the one-dimensional translational and the rotational entropies of the gas-phase species. In this work, these values were computed according to the statistical thermodynamics [151]:

$$S_{1D,trans} = \frac{1}{3} S_{3D,trans} = \frac{1}{3} \left\{ k_B . \ln Q_{trans} + k_B T . \left[\frac{\partial ln(Q_{trans})}{\partial T} \right]_{N,V} \right\}$$

$$Q_{trans} = \frac{q_{trans}^N}{N!}$$

$$q_{trans} = \left(\frac{2\pi m k_B T}{h^2} \right)^{\frac{3}{2}} . V$$

$$S_{rot} = k_B . \ln Q_{rot} + k_B T . \left[\frac{\partial ln(Q_{rot})}{\partial T} \right]_{N,V}$$

$$Q_{rot} = \frac{q_{rot}^{N}}{N!}$$

$$q_{rot} = \left(\frac{8\pi^2 k_B T}{h^2}\right)^{\frac{3}{2}} . \frac{\sqrt{\pi I_x I_y I_z}}{\sigma}$$

$$I_{x,y,z} = \sum_{i}^{number\ of\ atoms} m.d_{i-(x,y,z)\ axis}^{2}$$

The zero-point energy (ZPE), internal energy (U), enthalpy (H), Gibbs free energy (G) are calculated following the statistical thermodynamics [151]. The difference in energies upon the adsorption is referenced from the gas-phase species.

$$E_{ZPE} = \sum_{i}^{modes} \frac{1}{2} h\nu_i$$

$$U = E_{electronic\ (DFT-D3)} + E_{ZPVE} + k_B T^2 . \left[\frac{\partial ln(Q_{total\ ensemble})}{\partial T}\right]_{N,V}$$

$$Q_{total\ ensemble} = \frac{(q_{trans} . q_{rot} . q_{vib})^N}{N!}$$

$$q_{vib-gas} = \prod_{i}^{3n-6} \frac{1}{1 - exp\left(\frac{-h\nu_i}{k_B T}\right)}$$

$$q_{vib-adsorbate} = \prod_{i}^{3n} \frac{1}{1 - exp\left(\frac{-h\nu_i}{k_B T}\right)}$$

$$H = U + PV = U + RT$$

$$G = H - TS$$

$$S = S_{trans} + S_{rot} + S_{vib}$$

$$S_{vib} = k_B . \ln Q_{vib} + k_B T . \left[\frac{\partial ln(Q_{vib})}{\partial T}\right]_{N,V}$$

$$Q_{vib} = \frac{q_{vib}^{N}}{N!}$$

$$\Delta G = -RTlnK_{ads}$$

References

[149] P. J. Dauenhauer and O. A. Abdelrahman, A universal descriptor for the entropy of adsorbed molecules in confined spaces, ACS Central Science 4 (2018) 1235-1243.

[151] C. J. Cramer, "Computational Chemistry: Theories and Models," ed: John Wiley & Sons, Chichester, England, 2004.

Appendix A5: Dehydration of 2,4-pentanediol and ethylene-vinyl alcohol co-polymer (EVOH) over sulfonic acid-functionalized silica catalyst

1. Materials and methods

Poly(vinyl alcohol-co-ethylene) (EVOH, pellets, ethylene 32 mol %), 2,4-pentanediol (98%), dimethyl sulfoxide (DMSO, ≥99.9%, Sigma-Aldrich), silica gel (high-purity grade, Davisil Grade 646, 35-60 mesh, pore size 150 Å), 3-mercaptopropyl trimethoxysilane (MPTMS, 95%), anhydrous methanol (99.8%), anhydrous ethanol (≥99.5%), hydrogen peroxide aqueous solution (30 wt%) were purchased from Sigma-Aldrich and used as received. ZSM-5 zeolite (CBV-28014, Si/Al = 140) was purchased in the ammonium form NH_4-ZSM-5 from Zeolyst International and calcined in flowing dry air at 600°C for 5 h with a heating rate of 2°C/min to obtain the proton-form zeolite. The protonated zeolite was pelletized, crushed, and sieved to particles with sizes ranging from 90 – 250 μm. H-ZSM-5 zeolite is denoted as MFI-140.

Sulfonic acid-functionalized silica was prepared by high-temperature grafting silylation method to minimize leaching of acid functional group from the silica support in liquid phase reaction [78, 166]. Before functionalization, the silica gel was dried overnight at 80°C in a vacuum oven to remove any physisorbed water. Incipient wetness impregnation was carried out by adding dropwise 3.45 ml of methanol solution of 2.5 M 3-mercaptopropyl trimethoxysilane onto 2.89 g of the silica gel. The solid was transferred to a Teflon-lined autoclave and heated to 180°C for 14 h. After functionalization, the solid was washed three times with ethanol and dried at 80°C in a vacuum oven for 12 h. The sample was oxidized in 25 mL of a 30 wt% H_2O_2 stirred solution at room temperature for 12 h to obtain the sulfonic acid groups. The solid was separated from the

solution, washed three times with ethanol, and dried at 80°C in a vacuum oven for 12 h. The acid-functionalized silica catalyst is denoted as SiO_2-SO_3H.

Thermogravimetric analysis with the temperature program oxidation (TGA-TPO) was performed on a Netzsch STA 449F1 equipped with a pin thermocouple and a Netzsch nano-balance to quantify the number of functional groups per gram catalyst. The catalyst sample was placed in a crucible with a constant flow of argon (20 ml/min) and air (40 ml/min). The cell was preheated to 40°C for 10 min before being increased to 700°C with a ramping rate of 3°C/min. The outlet gases (H_2O, CO_2, SO_2) were analyzed on an on-line mass chromatography Aeolos QMS 403C.

Fourier-transform infrared (FT-IR) spectroscopy was carried out in a PerkinElmer Spectrum 100 Fourier Transform Infrared (FT-IR) spectrometer equipped with a high-temperature diffuse reflectance Infrared Fourier Transformation (DRIFT) CaF_2 cell (HVC, Harrick). A blank run of KBr pellet was obtained for the background. The polymer samples were pretreated at 50°C for 1 h before obtaining FT-IR spectra in He inert atmosphere.

Nuclear magnetic resonance (NMR) experiments were performed at OU NMR Facility on Varian VNMRS 400 MHz spectrometer with a dual broadband probe at 25°C. NMR samples were prepared in DMSO-d6 solvent.

Vapor phase dehydration of 2,4-pentanediol was carried out in a quartz tube reactor (1/4" OD) at atmospheric pressure. SiO_2-SO_3H catalyst was pretreated by heating to 250°C at the ramp rate of 10°C/min and held at 250°C for 1 h to remove physisorbed water in the catalyst. The detail of the catalytic testing is described in Chapter 4.

Liquid phase dehydration of EVOH polar polymer was conducted in a three-neck round bottom flask in nitrogen atmosphere and heated by a silicon oil bath. EVOH pellets were fully dissolved in 10 ml of DMSO solvent before catalyst was added to the stirred solution at the reaction temperature. After reaction, the solution was decanted and cooled down, followed by adding water as an anti-solvent to collect the polymer product.

2. Thermal Gravimetric Analysis (TGA) results

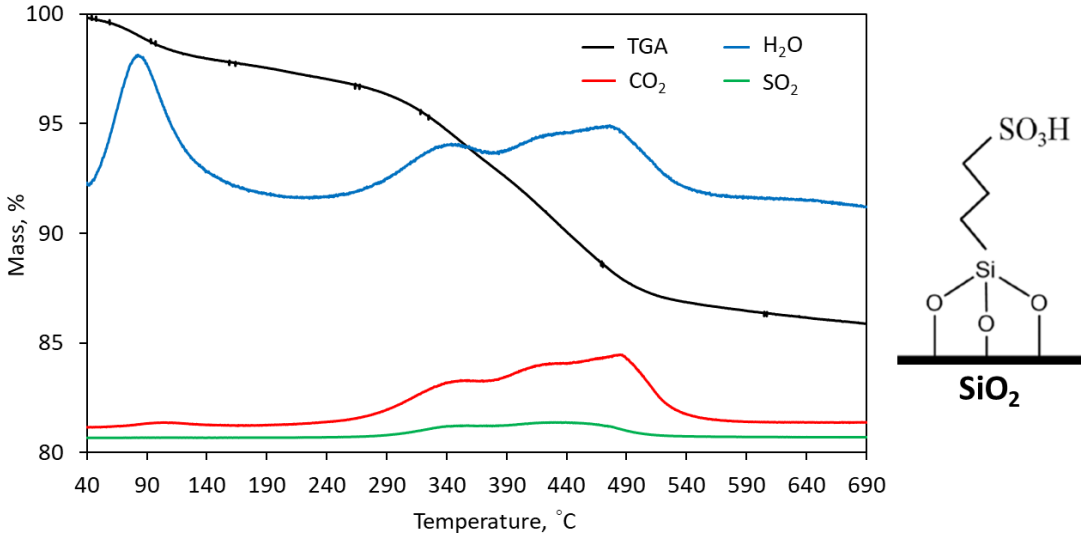

Fig. 49. TGA-TPO plot of SiO_2-SO_3H catalyst

Fig. 49 shows the TGA-TPO result of SiO_2-SO_3H catalyst with four temperature regions consistent with the previous report [166]. The mass loss in the temperature range of 40-120°C is attributed to the removal of physisorbed water, as indicated by the peak of water in the mass spectrometry. There is no significant mass loss and detectable MS peaks in the second temperature region (120-300°C). The third temperature range of 300-500°C shows a considerable mass loss due to the thermal degradation of the functional groups, as MS peaks of CO_2, SO_2, and H_2O were detected. Based on the mass loss in this region, the acid site density of the sulfonic acid-functionalized silica was obtained with 0.902 mmol/g sulfonic groups per gram catalyst. The small

mass loss in the temperature above 500°C is attributed to the thermal dehydroxylation of free silanol groups on the catalyst surface [167].

3. Vapor phase dehydration of 2,4-pentanediol

In this section, in contrast to the 2,5-hexanediol which quickly forms the dimethyl tetrahydrofuran intermediate (Chapter 4), 2,4-pentanediol was studied as another model compound to represent the functionality of EVOH polar polymer with shorter distance between OH groups and unlikely to form the cyclic ether.

Different products in the vapor phase dehydration of 2,4-pentanediol are detected, including 4-penten-2-ol, 2-pentanone, pentadienes, and pentene. Based on these observable products, the reaction pathway of 2,4-pentanediol dehydration over SiO_2-SO_3H catalyst is proposed in Scheme 3.

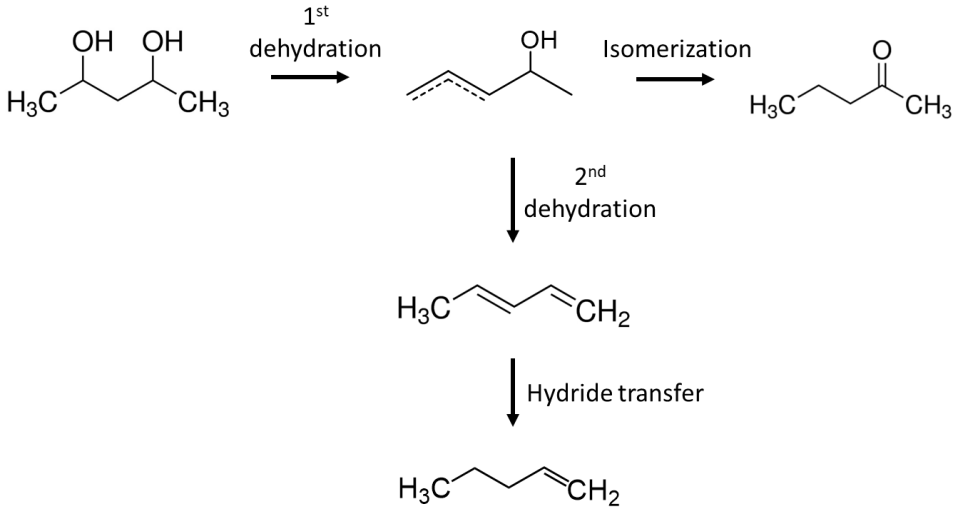

Scheme 3. Reaction pathway of 2,4-pentanediol dehydration over SiO_2-SO_3H catalyst

The conversion of 2,4-penanediol and product yields with varying reaction space time W/F (mass of catalyst/reactant flowrate ratio) is shown in Fig. 50.

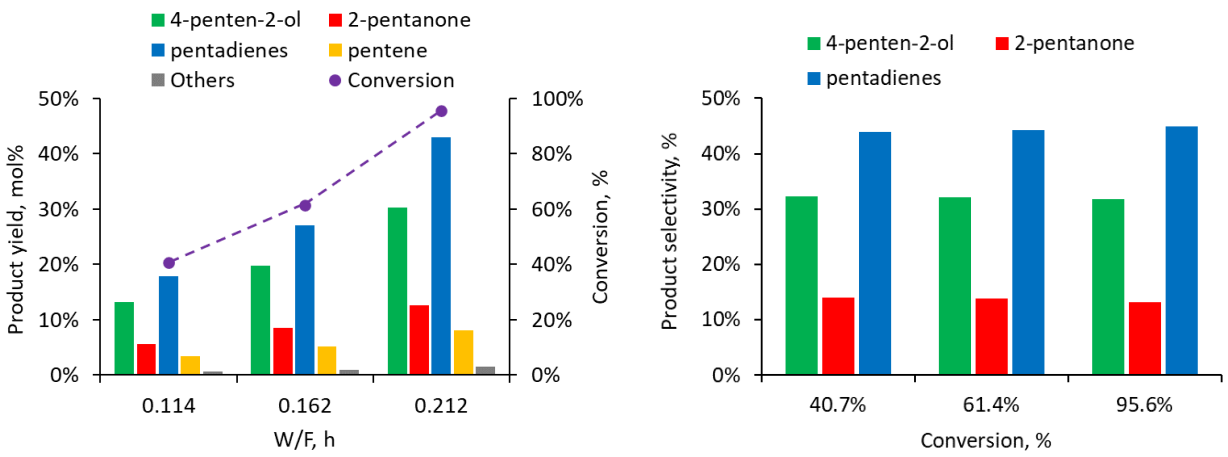

a) **b)**

Fig. 50. Initial conversion, product yields, and product selectivity of 2,4-pentanediol dehydration over SiO_2-SO_3H at 0-min TOS. Reaction conditions: T = 200°C, $P_{2,4\text{-pentanediol}}$ = 0.3 kPa

The conversion of 2,4-pentanediol increases linearly with W/F, indicating that it is not limited by external mass transfer or influenced by thermodynamic equilibrium under the reaction conditions. Interestingly, all the product yields keep increasing with the increase of 2,4-pentanediol conversion. In addition, the selectivity of 4-penten-2-ol, 2-pentanone, and pentenes remains unchanged with increasing the conversion. These results suggest that the three major observed products are formed in parallel, and 4-penten-2-ol is not likely to be the primary product of the first dehydration step.

4. Liquid phase dehydration of EVOH in DMSO

As polymer molecules are very bulky and entangled in the solid state, there are two approaches to increase the mobility of polymer molecules in catalytic polymer-to-polymer conversion without breaking C-C backbone. The first approach is heating polymer to the temperature above its melting point and carrying out reactions in molten phase. This method does not use any solvents and minimizes the cost of solvent separation after the reaction; however, it

requires a high energy consumption and may encounter side reactions at the high temperature, leading to a small operation window. The second approach is utilizing a proper solvent to solubilize the polymer, enabling the catalytic reactions in liquid phase. This process can happen at a much lower temperature than the melting point of the polymer, which reduces the energy usage and mitigates undesired by-products. However, it has the disadvantage of additional cost of solvent consumption and separation.

In this section, DMSO was selected as the solvent as EVOH is fully soluble in this solvent. The peak assignments in FT-IR spectra are described in Chapter 4. It is worth mentioning that the acid sites in SiO_2-SO_3H are exposed on the external catalyst surface and more accessible by the bulky polymer molecules compared to the microporous zeolites.

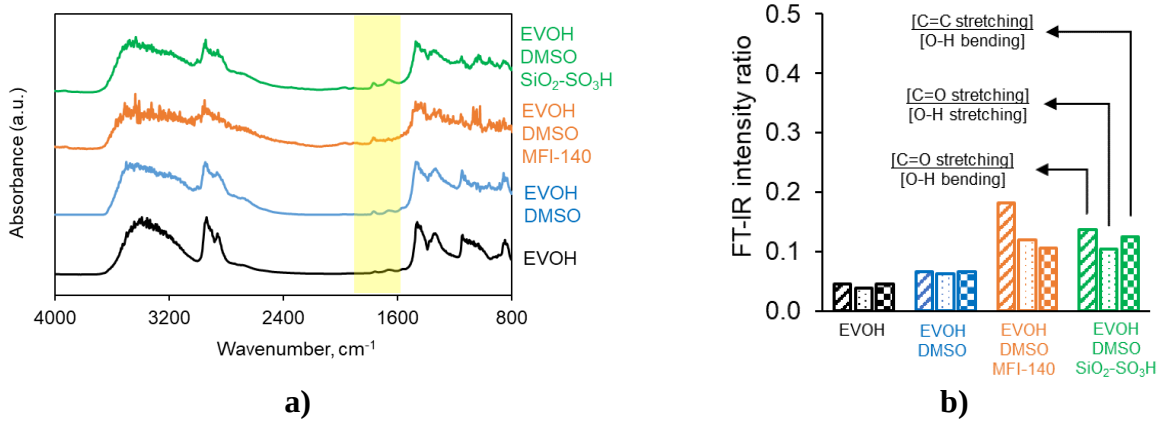

a) **b)**

Fig. 51. a) FT-IR spectra of fresh EVOH powder and dried solid products after reactions in liquid phase. **b)** FT-IR peak intensity ratios of different bonds of fresh EVOH powder and dried solid products after reactions in liquid phase. Reaction conditions: Nitrogen atmosphere, 1 g EVOH, 10 ml DMSO, T = 120°C, 100 mg catalyst, reaction time = 2 h, stirring = 600 rpm

Fig. 51a shows the appearance of C=O bond stretching with the presence of catalysts such as MFI-140 and SiO_2-SO_3H. In addition, the IR adsorption band for C=C stretching becomes more visible in the FT-IR spectrum of the solid product after the reaction over SiO_2-SO_3H. The catalytic

effect of MFI-140 and SiO_2-SO_3H is further revealed by FT-IR intensity ratios as shown in Fig. 51b with the increase of C=O stretching and C=C stretching relative peak intensity.

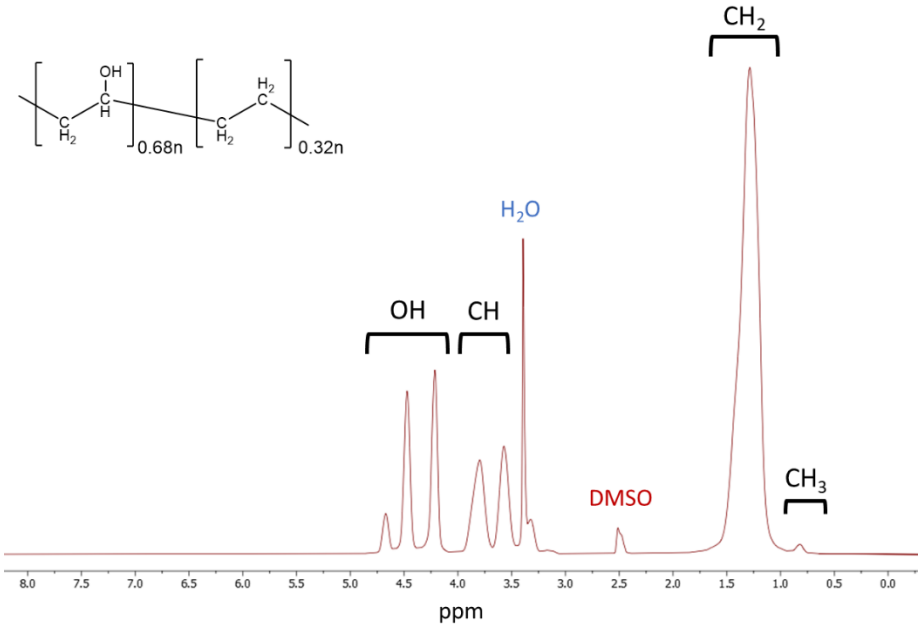

Fig. 52. ^{1}H NMR spectrum of fresh EVOH polymer in DMSO-d6

Different bonds associated with hydrogen and carbon in the polar polymer samples can also be analyzed by ^{1}H NMR and ^{13}C NMR in DMSO-d6 solvent [168, 169]. Fig. 52 and Fig. 53 shows the ^{1}H NMR and ^{13}C NMR spectra of the fresh EVOH polymer with the peak assignments are clearly indicated on the spectra. Based on peak integration and normalization of the ^{1}H NMR spectrum, the calculated fractions of distinct bonds associated with hydrogen atom are consistent with the theoretical values of the EVOH polar polymer sample, as shown in Table 9.

Table 9. Fractions of bonds associated with hydrogen atoms in EVOH

Fraction, %	**R-CH_3**	**R-CH_2-R**	**R-CH-R**	**R-OH**
Theoretical value	-	49.25	25.37	25.37
^{1}H NMR calculation	0.34	47.53	24.07	28.06

Although there is a small discrepancy between the theory and the ^{1}H NMR, the fraction of R-OH would be useful to calculate the conversion level of the EVOH dehydration.

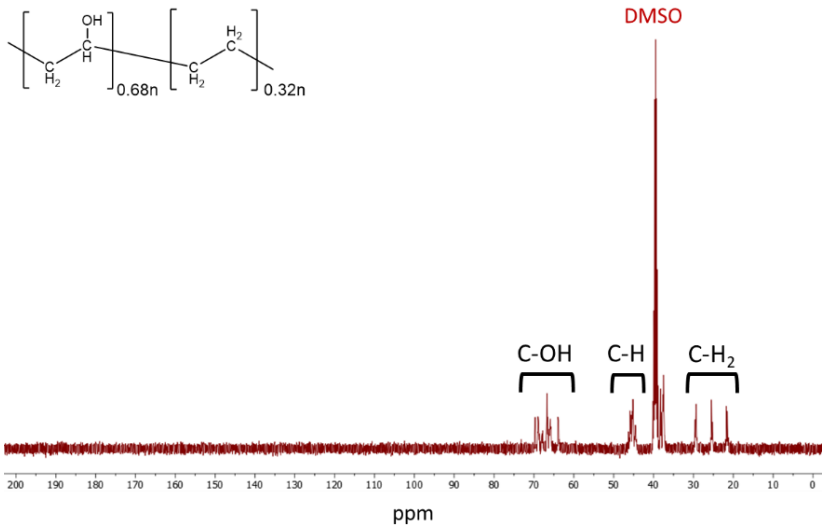

Fig. 53. ^{13}C NMR spectrum of fresh EVOH polymer in DMSO-d6

References

[78] G. Li, B. Wang, B. Chen, and D. E. Resasco, Role of water in cyclopentanone self-condensation reaction catalyzed by MCM-41 functionalized with sulfonic acid groups, Journal of Catalysis 377 (2019) 245-254.

[166] T. V. Bui, S. J. Umbarila, B. Wang, T. Sooknoi, G. Li, B. Chen, and D. E. Resasco, High-temperature grafting silylation for minimizing leaching of acid functionality from hydrophobic mesoporous silicas used as catalysts in the liquid phase, Langmuir 35 (2019) 6838-6852.

[167] X. S. Zhao, G. Lu, A. Whittaker, G. Millar, and H. Zhu, Comprehensive study of surface chemistry of MCM-41 using 29Si CP/MAS NMR, FTIR, pyridine-TPD, and TGA, The Journal of Physical Chemistry B 101 (1997) 6525-6531.

[168] I. Korbag and S. Mohamed Saleh, Studies on the formation of intermolecular interactions and structural characterization of polyvinyl alcohol/lignin film, International Journal of Environmental Studies 73 (2016) 226-235.

[169] S. Ito, M. Noguchi, and K. Nozaki, Ping-pong polymerization by allylation and hydroformylation for alternating vinyl alcohol–vinyl monomer copolymers, Chemical Communications 48 (2012) 10481-10483.

Appendix A6: Effect of water solvent on hydrogenation of a phenolic compound over supported metal catalysts in aqueous phase

1. Materials and methods

o-cresol (99%), 2-methylcyclohexanone (≥99.5%), 2-methylcyclohexanol (mixture of cis and trans, 99%), n-dodecane (≥99%), tetraamminepalladium(II) nitrate solution (10 wt. % in H_2O), and 3,5-lutidine (≥99%) were purchased from Sigma Aldrich and used as received. LUDOX® TM-50 colloidal silica (50 wt. % suspension in H_2O) was purchased from Sigma Aldrich and washed and dried to obtain the silica nanoparticles as described in the previous report [170]. Multiwalled carbon nanotubes (MWCNT) were obtained from Southwest Nanotechnologies.

Silica-supported palladium (hereafter denoted as Pd/SiO_2, metal loading 1.47 wt%) was prepared by the incipient wetness impregnation method by adding dropwise 0.8 ml $Pd(NH_3)_4(NO_3)$ (10 wt. % in H_2O) solution to 2 g silica nanoparticles. The sample was slowly heated to 80°C at 1°C/min, dried at 80°C for 12 h, followed by heating to 350°C with the ramping rate of 2°C/min in flowing air. The dried sample was calcined at 350°C for 2 h to obtain the Pd/SiO_2 catalyst. Similarly, carbon nanotubes-supported palladium (hereafter denoted as Pd/CNT, metal loading 3.74 wt%) was prepared by the incipient wetness impregnation method by adding dropwise 0.5 ml $Pd(NH_3)_4(NO_3)$ (10 wt. % in H_2O) solution to 0.5 g silica nanoparticles. The sample was slowly heated to 80°C at 2°C/min, dried at 80°C for 12 h, followed by heating to 350°C with the ramping rate of 10°C/min in flowing air. The dried sample was calcined at 350°C for 2 h to obtain the Pd/CNT catalyst.

The hydrogenation reactions of o-cresol over supported palladium catalysts were carried out at 150°C in a Parr batch reactor (300 mL) equipped with an in-situ ATR-IR spectroscopic

probe to online monitor the IR spectra of the reaction mixture during the reaction time on stream (TOS). The agitator speed was 750 rpm. Supported palladium catalysts were reduced in hydrogen at 150°C for 2 h to obtain the metal form with the minimal of palladium nanoparticles [171]. The details of the catalytic testing were described elsewhere [172, 173].

After the reactions, the reactor was cooled down to room temperature, and the liquid products were analyzed by a GC-MS and a GC-FID for product identification and quantification. The final concentration of the reactant and products was calculated from the calibration curves, which were built by manual injection of the standards in the GC-FID. The concentration profile versus reaction time on stream, unless otherwise noted, was obtained based on the final concentration values and the in-situ ATR-IR peak heights.

The BET surface areas and pore volumes of MWCNT and SiO_2 were obtained by the nitrogen adsorption-desorption analysis. The experiment was conducted on a Micromeritics ASAP 2020 at liquid nitrogen temperature (-196°C) after degassing the samples at 200°C in the vacuum for 12 h.

2. Effect of water solvent on the hydrogenation of o-cresol

Hydrogenation of lignin-derived phenolic compounds is an essential treatment of the biofuel upgrading process to improve biofuels' heating value and thermal stability. The hydrogenation reaction of phenolic compounds has been studied in the gas phase [174]. However, the presence of water during biomass processing requires more in-depth studies on the hydrogenation of phenolic compounds in the aqueous phase to facilitate the practical aspects of the biofuel hydrotreating processes.

Table 10. BET surface areas and pore volumes of catalyst supports

	BET specific surface area, m^2/g	Pore volume, cm^3/g	Micropore volume, cm^3/g
MWCNT	299.0	1.039	0.018
SiO_2	101.7	0.230	0.004

The typical IR spectra with peak assignments of reaction mixture during the reaction time on stream are shown in Fig. 54.

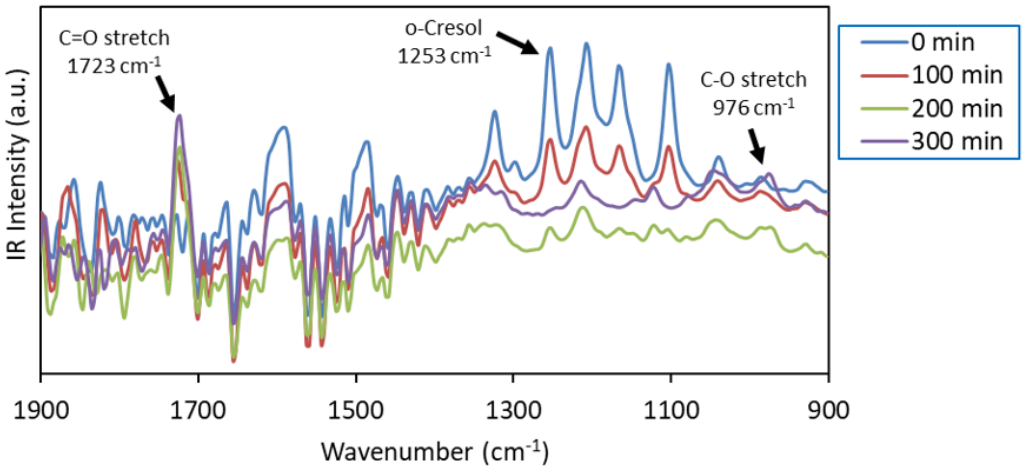

Fig. 54. The change of in-situ ATR-IR signal versus reaction time on stream

The concentration of o-cresols and two observed products (2-methylcyclohexanone and 2-methylcyclohexanol) as a function of the reaction time on stream during the hydrogenation in the apolar solvent (n-dodecane) is shown in Fig. 55. While the concentration of 2-methylcyclohexanone increases to a maximum value and then decreases, the concentration of 2-methylcyclohexanol keeps increasing over time. These results suggest that the hydrogenation of o-cresol proceeds via the ketone intermediate and eventually form the final alcohol product (Scheme 4).

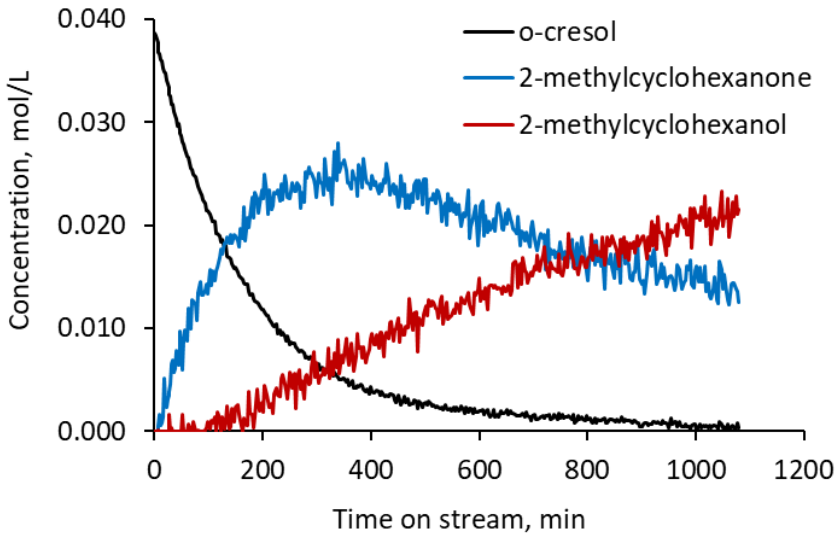

Fig. 55. Concentration vs. time profiles from in-situ IR spectra during the hydrogenation of o-cresol in n-dodecane at 150°C on Pd/SiO_2. Reaction conditions: 120 ml n-dodecane, 60 mg Pd/SiO_2. Concentration values are calibrated by the in-situ ATR-IR peak heights.

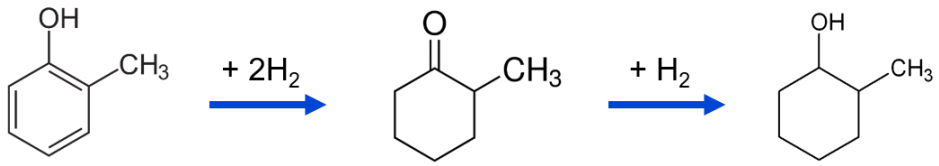

Scheme 4. Reaction pathway of the hydrogenation of o-cresol

TEM image of Pd/CNT (Fig. 56) shows the presence of palladium nanoparticles on the MWCNT support. Although it would be more obvious with 3D TEM analysis, it seems that most of the palladium nanoparticles are located on the external surface of the carbon nanotubes.

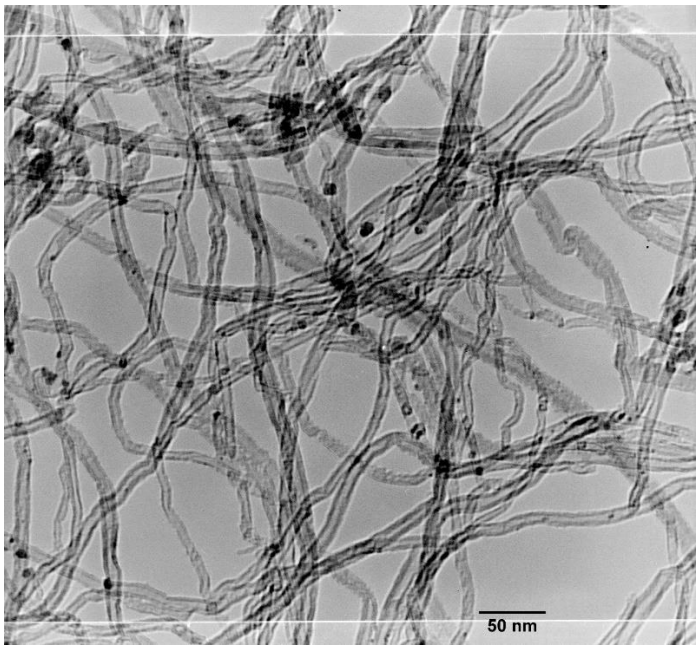

Fig. 56. TEM image of palladium particles on carbon nanotubes

The hydrogenation of o-cresol over Pd/CNT in aqueous phase and organic phase are shown in Fig. 57 and Fig. 58.

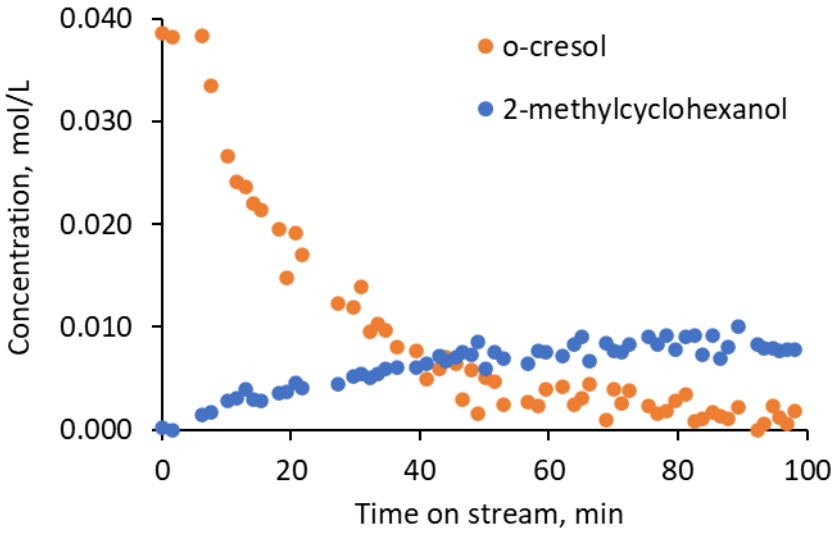

Fig. 57. Concentration vs. time profiles from in-situ IR spectra during the hydrogenation of o-cresol in water at 150°C on Pd/CNT. Reaction conditions: 120 ml water, 63 mg Pd/CNT.

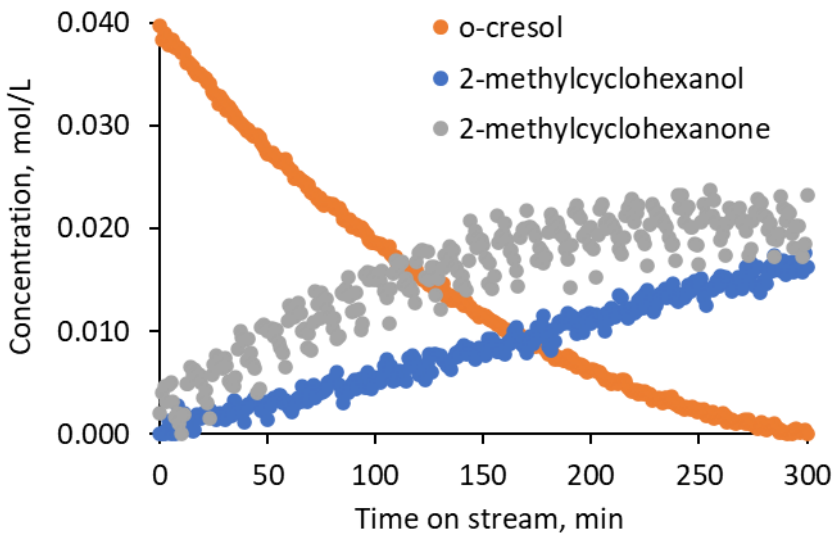

Fig. 58. Concentration vs. time profiles from in-situ IR spectra during the hydrogenation of o-cresol in water at 150°C on Pd/CNT. Reaction conditions: 120 ml n-dodecane, 61 mg Pd/CNT.

Based on the reaction time on stream to reach the 100% conversion, it clearly shows that the reaction rate of hydrogenation reaction of o-cresol in the aqueous medium is significantly higher than that in the organic phase. In addition, while both ketone (2-methylcyclohexanone) and alcohol (2-methylcyclohexanol) products are present in the organic phase reaction, only 2-methylcyclohexanol was detected in the aqueous phase reaction. These results are consistent with the previous report on the hydrogenation of o-cresol on supported platinum catalyst [173]. It is speculated that the hydrogenation of o-cresol in the aqueous phase is assisted by the water-assisted proton transfer, which was observed in the hydrogenation of the furanic compounds [7]. The absence of ketone product in the aqueous phase may be attributed to the reduced rate of desorption of the hydrophobic ketone intermediate from the catalyst support to the polar aqueous phase. As a result, the first hydrogenation step of o-cresol forms 2-methylcyclohexanone, which stays on the catalyst surface and continues to convert to 2-methylcyclohexanol.

Acknowledgements

This work was supported by the NSF. Microscopy was accomplished in conjunction with the Sam Nobel Microscopy Laboratory at OU, and the authors would like to thank Dr. Lawrence Barrett for his assistance with the TEM images.

References

[7] Z. Zhao, R. Bababrik, W. Xue, Y. Li, N. M. Briggs, D.-T. Nguyen, U. Nguyen, S. P. Crossley, S. Wang, B. Wang, and D. E. Resasco, Solvent-mediated charge separation drives alternative hydrogenation path of furanics in liquid water, Nature Catalysis 2 (2019) 431-436.

[170] J. Weston, R. Jentoft, B. Grady, D. Resasco, and J. Harwell, Silica nanoparticle wettability: Characterization and effects on the emulsion properties, Industrial & Engineering Chemistry Research 54 (2015) 4274-4284.

[171] M. Gurrath, T. Kuretzky, H. Boehm, L. Okhlopkova, A. Lisitsyn, and V. Likholobov, Palladium catalysts on activated carbon supports: Influence of reduction temperature, origin of the support and pretreatments of the carbon surface, Carbon 38 (2000) 1241-1255.

[172] Y. Li, Z. Liu, W. Xue, S. P. Crossley, F. C. Jentoft, and S. Wang, Hydrogenation of o-cresol on platinum catalyst: Catalytic experiments and first-principles calculations, Applied Surface Science 393 (2017) 212-220.

[173] Y. Li, Z. Liu, Y. Liu, S. P. Crossley, F. C. Jentoft, and S. Wang, Hydrogenation of o-cresol at the water/Pt (111) interface, The Journal of Physical Chemistry C 123 (2019) 5378-5384.

[174] C. Chen, G. Chen, F. Yang, H. Wang, J. Han, Q. Ge, and X. Zhu, Vapor phase hydrodeoxygenation and hydrogenation of m-cresol on silica supported Ni, Pd and Pt catalysts, Chemical Engineering Science 135 (2015) 145-154.